University of Cincinnati

Date: 2/28/2014

I, Peter A Sandwall II, hereby submit this original work as part of the requirements for the degree of Doctor of Philosophy in Nuclear & Radiological Engineering.

It is entitled:

Spatial Dosimetry with Violet Diode Laser-Induced Fluorescence of Water-Equivalent Radio-Fluorogenic Gels

Student's name: **Peter A Sandwall II**

This work and its defense approved by:

Committee chair: Henry Spitz, Ph.D.

Committee member: Henry Fenichel, Ph.D.

Committee member: William Connick, Ph.D.

Committee member: Howard Elson, Ph.D.

Committee member: Michael Lamba, Ph.D.

9048

Spatial Dosimetry with Violet Diode Laser-Induced Fluorescence of Water-Equivalent Radio-Fluorogenic Gels

A dissertation submitted to the

Division of Research and Advanced Studies
of the University of Cincinnati

in partial fulfillment of the
requirements for the degree of

Doctorate of Philosophy

in the School of Dynamic Systems
of the College of Engineering & Applied Science

April 2014

by

Peter A. Sandwall II

B.S., West Virginia Wesleyan College 2004
M.S., University of Cincinnati 2006

Committee: **Henry B. Spitz, Ph.D. (Chair)**

Howard R. Elson, Ph.D.

Michael A.S. Lamba, Ph.D.

William B. Connick, Ph.D.

Henry Fenichel, Ph.D.

ProQuest LLC.
789 East Eisenhower Parkway
P.O. Box 1346
Ann Arbor, MI 48106 - 1346

Abstract

The following work describes investigations of spatial dosimetry using laser-induced fluorescence of a radio-fluorogenic detector embedded within water-equivalent media. The chemical composition of a gelatin-based coumarin-3-carboxylic acid detector was investigated and dose response characterized. Violet diode (405nm) excitation sources were explored and laser-induced fluorescence (LIF) employed to obtain the pattern of fluorescent emission yielding images of the integrated spatial dose distribution. The design of a three-dimensional reader is proposed to provide a foundation for future work.

Radio-fluorogenic processes create fluorescent products in response to ionizing radiation. Water radiolysis produced by ionizing radiation yields hydroxyl free radicals that readily hydroxylate coumarin-3-carboxylic acid to 7-hydroxy-coumarin-3-carboxylic acid, a derivative of umbelliferone. Umbelliferone is a known fluorophore, exhibiting peak excitation in the UV to near UV range of 365-405nm with a visible 445nm blue emission. Coumarin-3-carboxlyic acid has been studied in an aqueous gelatin matrix.

The radio-fluorogenic coumarin-gelatin detector has been shown to respond to an absorbed dose of ionizing radiation in a measureable manner. The detector was studied with respect to concentration of gelatin and coumarin in the presence of pH buffers. Dose response of the detector was investigated with regard to ionizing radiation type, energy, and rate of irradiation. Results demonstrate a functional detector.

Patterns of energy deposition were formed in response to ionizing radiation produced by a sealed-source of radioactive Ir-192 embedded in the gelatin matrix of the detector. Spatial distributions of absorbed dose were recorded and analyzed as a function of fluorescent emission. The distribution of energy deposition was imaged with LIF excitation by a divergent beam of 405nm light and determined by analysis of digital image pixel intensity values displaying the 445nm fluorescent emission. Results demonstrate spatial dosimetry proof of principle.

A basic dedicated reader system was fabricated employing LIF. Images of fluorescent emission excitation profiles were obtained in multiple aqueous samples and processed to obtain a dose response. Design of an optical reader system for the radio-fluorogenic detector is explained and a three-dimensional dosimetry system proposed. Three-dimensional imaging principles with LIF have been illuminated.

Acknowledgements

All scientists stand on the shoulders of giants, many unsung and underappreciated. The present work would not have been possible without John Sweet, who paved the way with his pioneering work, investigating the use of agarose-based benzoate acid as a radio-fluorogenic gel. His unpublished studies provided the foundation upon which I stand.

Humble thanks to all of the many professors who helped me along my educational path. Of special note, my first physics professor, Dr. Wiest, who first exposed me to the light. Dr. Spitz, my advisor and committee chair, who accepted me into his program and patiently allowed my eyes to open. Committee members, Dr. Elson, whose perceived toughness only made me a stronger candidate. Dr. Lamba, who prodded me to go further and think clearer, Dr. Connick, whose initial instruction and continued encouragement have been invaluable, and, Dr. Fenichel who graciously allowed me full use of his laboratory.

Mi familia, Delmo Bianco, Robert Coit, and many supportive friends I have been blessed with along the way; too numerous to name individually, you know exactly who you are. The Brennan clan, who opened their hearts and home without question or conditions. The entire families of Chaves and Sandwall, whom have remained constant throughout the waxing and waning of my appetites and attention. Of particular note, without the support of my paternal grandmother, Kiesti Swanstrom and aunt Karin Sandwall, I may never

have had the opportunity of learning to love science. My maternal uncle, Carlos Chaves, without whose help my journey of discovery may have ended prematurely.

My mother, Gloria Tamara and sisters Erica Dagmar and Tara-Mickalina whom have been with me through thick and thin, believing in me before I believed in myself.

Last but certainly not least, Susan Marie, my beautiful wife who has gifted my life with stability and constancy, and two amazing daughters, Sophia Marie and Olivia Kelley, with more on the way!

There but for the grace of god, go I

Table of Contents

List of Figures and Tables

Chapter 1

Introduction

1.1 Introduction

Cancer is one of the leading causes of death worldwide.[1] The three primary methods of treatment are surgery, chemotherapy, and radiotherapy. Roughly 50% of cancer patients receive radiotherapy and international access to it continues to increase.[2-3] Accurate delivery of absorbed dose and the energy imparted to the treatment volume are essential to ensure efficacy of tumor control probability.[4-5]

Technological advancements have allowed for increasingly intricate multi-dimensional treatments delivered in fewer fractions, requiring patient-specific quality assurance prior to delivery.[6-8] The technology now exists to deliver a highly conformal plan with tight margins around the tumor and reduced irradiation of surrounding tissues. (Figure 1)

a.  b. 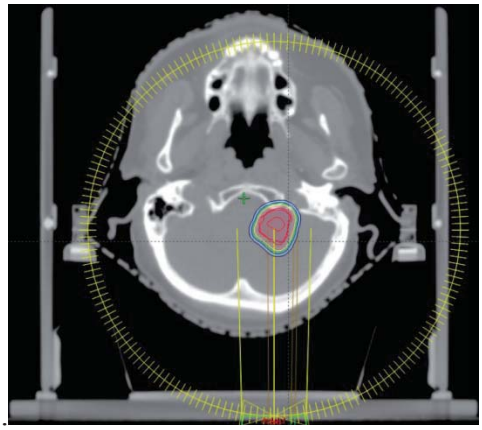

Figure 1. (a) Illustration of a medical linear accelerator with an immobilized patient, the beam shaping device can be seen above the patient.[9] (b) illustrates a computer-generated treatment plan on the axial slice of a computed-tomography image. The colored isodose lines represent absorbed dose with the red representing 100% of the intended dose and blue representing 50%. The yellow circle indicates treatment delivered in a continuous-arc.[10]

Complexities of modern treatment delivery have now advanced beyond the degree that commonly available quality assurance devices can accurately measure.[11] Proposed spatial solutions have included interpolating detector arrays and fully integrating gel-based systems.[12-14] While interpolating detector arrays are useful tools, they are not fully integrating dosimeters. With the potential to provide fully integrated multi-dimensional dose distributions and near tissue equivalence, gel dosimeters have repeatedly been championed as the appropriate sensors system. Investigations in search of the ideal dosimeter are ongoing.[15-18] The present work describes studies of a water-equivalent, radio-fluorogenic gel dosimetry system, relying on the production of fluorescent products for the measurement of absorbed dose.

1.1.1 Interactions of Light with Matter

Light is a form of energy, commonly defined as the visible portion of the electromagnetic spectrum. In physics, all of the electromagnetic spectrum is considered light. Understood to exist in duality as a wave and particle, light interactions with matter demonstrate characteristics described as wave, particle, or ray phenomena. These three approaches are used to describe various properties; in this manuscript, the particle and ray theories are most prevalent. Particle properties include momentum, absorption, and emission. Wave theory properties include diffraction, interference, and polarization. Ray theory properties include refraction and reflection.

Photons possess energy and momentum; interactions result in transfers. When a photon interacts with a material, energy and momentum are redistributed. This may result in excitation, ionization, or scattering depending on the magnitude of the interaction. Excitation may result in radiative emission, thermal dissipation, or other energy transfer. Scattering is simply the change in trajectory of the particle. Refraction is the change in speed and direction of a ray at the interface between materials. This property is characterized for materials by their refractive index. Reflection is redirection of light upon a surface, allowing for direct visualization of objects. Diffraction is bending and spreading of light when passing through an aperture or in response to an encounter with an obstacle. Diffraction is dependent on the wavelength or energy of light being studied. Interference is the superposition of multiple waves; such interference may be constructive or destructive. Polarization or angular arrangement of light is dependent on the phase of components.

1.1.1.1 Interactions of Visible Light with Matter

The Lambert-Beer Law is a mathematical expression for the transmission of light through matter. The decrease of light intensity can be expressed:

$$I_t = I_0 e^{-\alpha c l}$$

This shows transmission to be a function of the material concentration (c), optical path length (l), and a constant of proportionality (α). Quite similar to attenuation of x-ray beams, the exponential expression is a result of the decreasing population available to interact (undergo absorption). Akin to ionizing photons, the absorption coefficient is dependent on incident energy and absorbing material, i.e., wavelength and substance.

Absorption (A) or optical density (OD) of a material is a base 10 logarithmic function with the constant of proportionality replaced by the molar extinction coefficient (ε), a wavelength-dependent property inherent to the material. The Beer-Lambert Law predicts the OD to be proportional to the concentration of absorbing species. Biological samples are frequently turbid due to the presence of macromolecules that scatter light. Rayleigh scatter is proportional to $1/\lambda^4$; this is recognized to result in rapid reduction of transmitted intensity for shorter wavelengths. OD is expressed:

$$A = OD = \log\frac{I_0}{I_t} = \varepsilon c d$$

See Figure 2 for an illustration of the reduction of incident beam intensity per unit pathlength.

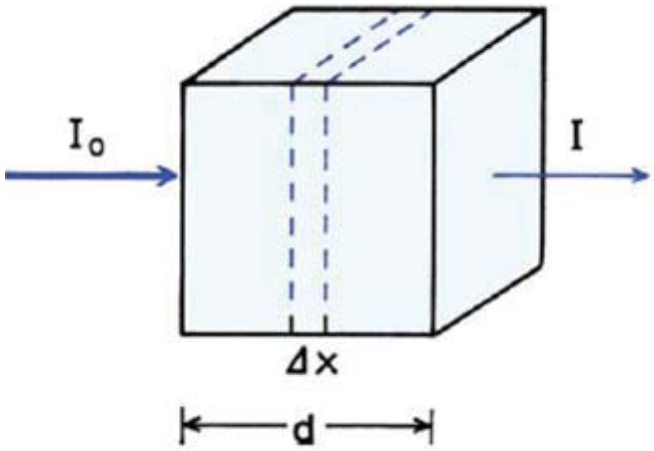

Figure 2. Illustration of an incident beam (I_0) traversing a pathlength of material and the subsequent reduction in intensity (I).[19]

Strongly dependent on wavelength, the molar extinction coefficient ($\varepsilon = \alpha / 2.303$) is expressed in units of $M^{-1}cm^{-1}$, when concentration (c) and path length (d) are stated in units of molarity M and cm, respectively. The relationship between absorbance (A) and transmission ($T = \frac{I_t}{I_0}$) is expressed:

$$A = -\log T$$

Under ideal conditions, measurement of absorption spectra allows derivation of the molar extinction coefficient when path length and concentration of a material are known. Unfortunately, ideal conditions are rarely met due to the optical properties of the sample container; reflection at the cuvette window results in a loss of light. This necessitates the use of a control to correct for inherent deviations within the system. Other deviations may be a result of solvent absorption, inhomogeneity within the sample, and aggregation of constituents.

Deviations from the Beer-Lambert Law are often the result of dye molecule aggregation, commonly found in the μ-mM concentration range. To account for this, it is favorable to determine an isosbestic point (wavelength), an equilibrium state where multiple components share the same extinction coefficient. Unfortunately, such points are rare in multicomponent systems.

Absorption of light and subsequent molecular excitation may yield fluorescence, a radiative return to the ground state from an excited singlet state. Non-radiative transfers of excitation energy are primarily a result of dipole-dipole interactions between the donor and acceptor neighboring molecules. Other excitation deactivation pathways include intersystem crossing, external conversion, and internal conversion; these are strongly influenced by environment and to a lesser degree, structure. Molecular predissociation and dissociation are almost entirely dependent on chemical structure; when analyzing a system the probability of each event is represented by a rate constant.[20]

1.1.1.1 Interactions of Ionizing Radiation with Matter

Ionizing radiation is radiant energy of sufficient energy to induce the loss of an atomic electron. There are two fundamental pathways of ionizing radiation interactions, direct and indirect. Uncharged radiations are indirectly ionizing, electromagnetic photons (quanta) and neutrons interact to release kinetically energetic charged particles which themselves are directly ionizing. Indirectly ionizing radiations interact less, but each interaction event results in a large energy loss. Charged particles are directly ionizing by Coulomb force interactions, freeing bound electrons. While the initial event is direct, energy deposition is predominately a result of secondary interactions. Directly ionizing radiations undergo many interactions, each resulting in a loss of less energy.[21]

Indirectly ionizing electromagnetic photons leads to the creation of delta-rays, directly ionizing energetic electrons, which are the predominant method of energy transfer. There are three primary processes of photon ionizing interactions, which will be briefly reviewed (Figure 3).

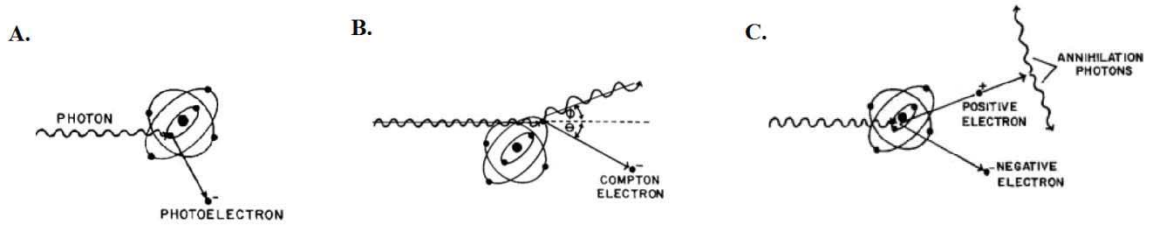

Figure 3. (a) Photoelectric effect, (b) Compton Effect, and (c) Pair Production. Each event results in the release of an energetic electron.[22]

The photoelectric effect (τ) describes the event when a photon is entirely absorbed by an atom that subsequently ejects an energetic electron. The photon's momentum is given to

the remaining positive ion while the kinetic energy of the photon is transferred to the ejected electron, minus the electrons atomic binding energy. The probability of photoelectric effect in a medium is approximated as proportional to $\frac{Z^n}{E^3}$. The positive ion combines with a loose electron and emits energy, which is assumed to deposit locally.[23]

In the Compton Effect (σ), a photon interacts with an atomic electron and both are scattered with a partial transfer of energy to the electron. The probability of scatter direction and subsequent energy transfer is a function of the incident photon energy with higher energies preferentially scattering forward, with the angle being proportional to energy loss. The probability of Compton scattering is directly dependent on Z; this process is the most probable for intermediate photon energies (range of radiotherapy). The fact that scattered photons may escape the volume of interaction complicates the calculation of energy imparted and resultant absorbed dose.[23]

Pair Production (κ) is when a photon interacts with the electrostatic field of an atomic nucleus, leading to the disappearance of the photon and simultaneous appearance of positive and negative electrons. Due to conservation of energy, this process requires the photon energy to exceed the rest mass of the two particles ($2m_0c^2$). The negative electron is considered a delta-ray, while the positive electron (positron) will travel a short distance before interacting with an electron and annihilating with the production of two 511keV photons. The probability of pair production is proportional to Z^2.[24]

As outlined in the preceding paragraphs, the three dominant photon interactions resulting in energy deposition are dependent on photon incident energy and atomic number of the absorbing material. Figure 4 shows the relative importance of each major type of photon interaction.

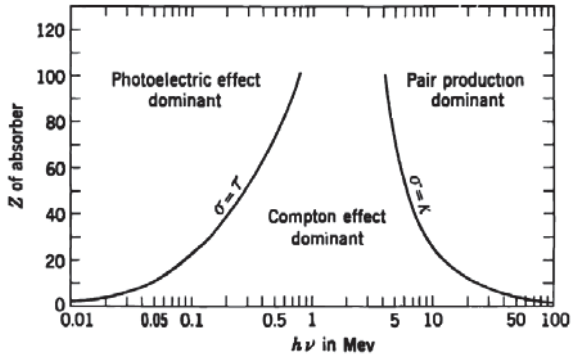

Figure 4. Relative importance of the three major types of photon interactions. Lines indicate where importance of energy and Z are equal.[24]

An agent of energy transfer, radiation deposits energy by stochastic processes represented by interaction coefficients.[21] The likelihood of a photon interaction in matter is an exponential function dependent on unit length of material a number of photons travels through. Solved from a first order differential equation, the probability of a number of photons traversing a distance (x) without an interaction is expressed:

$$\frac{I}{I_0} = e^{-\mu x}$$

Where I_0 is the initial intensity and I is the intensity that did not interact. The quantity μ is the total linear attenuation coefficient, which is the sum of interaction coefficients (probabilities of interaction) for the previously described processes ($\mu = \tau + \sigma + \kappa$).

The linear coefficients vary with density of absorber and it is often advantageous to normalize by material density; this quotient is known as the mass attenuation

coefficient $\left(\frac{\mu}{\rho}\right)$. This allows for the determination of attenuation through a composite of materials by summation of mass attenuation coefficients proportional to the mass of each element:

$$\left(\frac{\mu}{\rho}\right)_c = \sum_i w_i \left(\frac{\mu}{\rho}\right)_i$$

Where w_i is the weight fraction of elements.[25] This additive principle will return several times in the determination of interactions and imparted energy within a material.

The preceding equations allow for the determination of photon absorption in media. Photon attenuation is represented as an exponential function because particles that interact are assumed to be removed from the beam. Such behavior can only be observed when assuming narrow beam geometry; that is, neglecting contributions from scatter. The ingrowth of particles at depth due to scatter is referred to as build-up, which will be discussed further with regard to the measurement of energy imparted to a medium. Narrow beam geometry is rarely achieved and lends to the more complicated discussion of direct interactions which lead to the deposition of energy. As illustrated in Figure 3, the primary methods of photon interactions leading to energy transfer release energetic electrons, which are directly ionizing.

Energy exchange between energetic electrons and matter are the result of four mechanisms: inelastic collisions with atomic electrons (collisional energy loss, source of excitation, and ionization), inelastic collisions with an atomic nucleus (radiative energy loss, source of bremsstrahlung), elastic collisions with an atomic nucleus (non-radiative

energy loss), and elastic collisions with atomic electrons. All of the mechanisms of energy dissipation contribute to the energy exchange of charged particles; however, collisional energy losses are most relevant to discussions of radiation dosimetry.

Fundamental in determining biological effects from charged-particle interactions is the linear energy transfer (LET) or stopping power (*S*). Absorbed dose represents the volume density of energy transfer while LET is the rate. Stopping power is defined by:

$$S = -\frac{dE}{dx}$$

Where T is energy and x is distance. It should be noted both collision and radiative energy loss contribute to the stopping power; however, radiative energy loss is a fractional component most relevant for high-density materials. Radiation effects have been shown to be dependent on both the volume density and rate of energy deposition.[23]

From first principles, the electrostatic fields of charged particles are understood to interact with a force proportional to their charge and the inverse square of the distance between them. Defined by Coulomb's law, shown in scalar form for static particles:

$$F = k\frac{q_1 q_2}{r^2}$$

Where F is the force in Newtons (N), k is Coulomb's constant ($\frac{1}{4\pi\varepsilon_0} = 8.9875_E{}^9$ N m^2/C^2), q1 and q2 are the charges of particles involved in the interaction, and r is the distance between the two particles.[26] Examining the equation from which collisional stopping power is obtained:

$$-\left(\frac{dE}{dx}\right)_c = \frac{2\pi e^4 NZ}{m_0 v^2}\left(\ln\frac{m_0 v^2 E}{2I^2(1-\beta^2)} - (ln2)\left(2\sqrt{1-\beta^2} - 1 + \beta^2\right) + (1-\beta^2) + \frac{1}{8}\left(1-\sqrt{1-\beta^2}\right)^2\right)$$

Where v is the velocity of the particle, N and Z are the atomic density and number of the absorber, m_0 is the electron rest mass, e is the electronic charge, I is the average excitation and ionization potential of the element, and $\beta = v/c$. For a mixture of materials, similar to mass attenuation with photons, stopping powers for charged particles are assumed additive and derived from a weighted sum of stopping powers. This is expressed by the *Bragg-Kellman rule*:

$$\frac{1}{N_c}\left(\frac{dE}{dx}\right)_c = \sum_i W_i \frac{1}{N_i}\left(\frac{dE}{dx}\right)_i$$

Where, N is the atomic number density and w_i represents the atom fraction of the *i*th component.[25] The linear additive properties of both photon and electron interactions allow for determination of the absorbed dose within heterogeneous materials.

1.1.2 Radiation Dosimetry

The field of radiation dosimetry originated with the medical use of ionizing radiation and the desire to provide a physical correlate to biological effect. It was recognized early that biological effects are more directly related to the energy imparted, rather than the radiation fluence in a medium. Ionizing radiation traversing a material may interact with the medium, such interactions will result in a transfer of energy which could be deposited locally or transferred outside the volume. This can be understood with the following equation:

$$E_D = \sum E_{in} + \sum E_{out}$$

Where E_D is the energy imparted to the volume, comprised of the sum of energies that have entered volume (E_{in}) subtracted by the sum of energies that have left the volume (E_{out}).[21] The energy imparted to a volume of unit mass is a fundamental quantity of radiation dosimetry.

Radiation detectors are characterized by a response function resulting from energy imparted to a detection volume. Absorbed dose is defined as the energy imparted to a volume of unit mass:

$$D = \frac{dE_D}{dm}$$; unit, J/kg or Gy (gray)

Contingent on the concentration of interactions within a mass, the dependence on material density is apparent. Fundamental to radiation therapy, ionizing radiation prescriptions are given in units of Gy. The underlying concepts allowing for the determination of absorbed dose will now be reviewed.

As previously reviewed, when electrons pass sufficiently close to bound atomic electrons the resultant coulombic interactions may apply the force adequate to produce ionization. The energy threshold necessary to overcome the binding energy of an atomic electron is referred to as the ionization potential. Dependent on ionization potential, the mean energy ($\bar{W}$) necessary for creation of an ion pair in dry air is 33.97 eV. This value is nearly constant for all electron energies and allows determination of absorbed dose to a volume by collected charge within a calibrated ionization chamber coupled to an electrometer.

Ionization chambers are gas-filled detectors with a well-defined geometry that function by the collection of ion pairs produced by ionizing radiation interactions within a volume. Electronic equilibrium is the fundamental basis of cavity theory; detector volume and composition are selected to minimize perturbation of the field. The premise of equilibrium is $E_{in} = E_{out}$, such that contributions from scatter have reached a steady-state. With regard to photon beams, this is reached at the depth of maximum dose (D_{max}) followed with a state of transient equilibrium. The transient portion is stable, yet decreasing due to the reduced fluence. Preceding Dmax is the build-up region, in which some photons are escaping the volume without balance from photons entering.[27]

Placed within a water phantom, ion chambers are the accepted gold-standard for output verification and calibration of medical linear accelerators. Absorbed dose to water (or other media) can be obtained by use of interaction probabilities, stopping power ratios of the gas to medium. Since electronic equilibrium is a principal condition for accurate determination of radiation dose, the ideal detector has a material composition as near the object of study as possible.

1.1.3 Aqueous Dosimetry

With an atomic number and density similar to most biological tissue, water is the ideal medium for radiation dosimetry. Cells are composed of more than 70% water and are where the majority of energy deposition occurs. When determining interactions in a material, the weighted sum of atomic numbers may be used to justify material equivalence. Bragg's additive rule is defined as:

$$\langle Z_{eff} \rangle = \sum w_j Z_j$$

Where Z_{eff} is the effective atomic number and w_j is the weighted fraction of elemental constituents. Water is comprised of 11.1% hydrogen and 88.9% oxygen by weight. For water, the Z_{eff} is calculated to be: 1(2/18) +8(16/18) = 7.2. This is quite similar to reported values of soft tissue (7.1-7.4) and muscle (7.3-7.5).[28] (Figure 5)

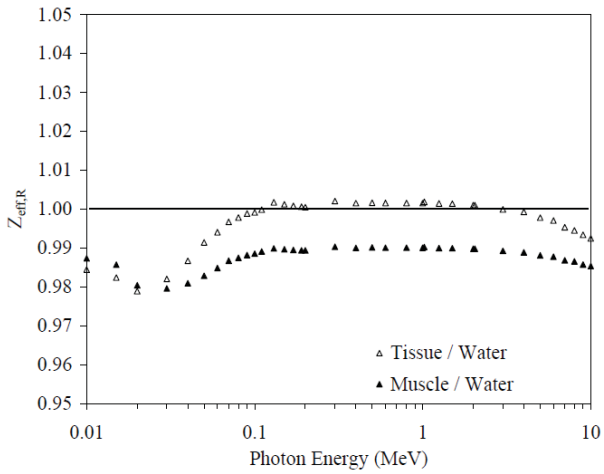

Figure 5. Illustrates the ratio of Tissue/Water and Muscle/Water for a range of photon energies. Values were calculated by linear addition of elemental compositions and cross referencing energy dependent interaction coefficients.[29]

Yields and reaction mechanisms in aqueous media have been studied extensively and are well known (Figure 6). Creation of reactive ions produces chemical reactions and subsequent biological damage. The chemical reactions resulting from interactions with ionizing radiation are generally attributed to "free radicals," such as hydroxyl radicals. Defined as a chemical unit possessing an unpaired or odd electron, free radicals are highly reactive and may result in addition and substitution reactions as well as hydrogen abstraction. This is known to induce DNA strand breaks resulting in the inability of

cellular division which leads to apoptosis, programmed cellular death. Figure 7 shows a block diagram of events leading to biological effects, adapted from reference.[21]

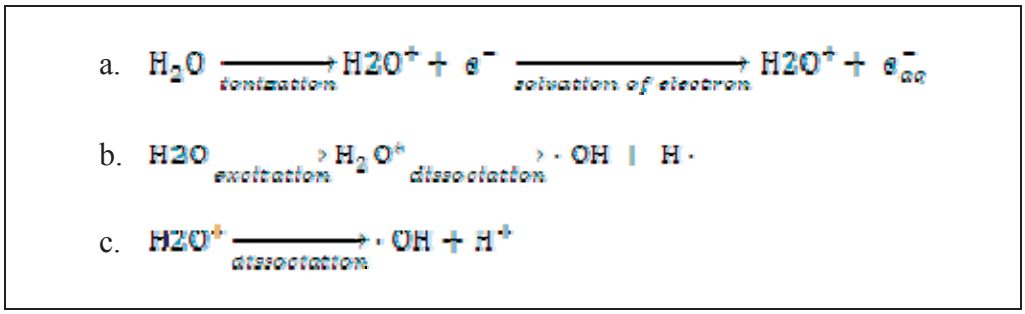

Figure 6. Creation of reactive oxidizing and reducing species from water molecules exposed to ionizing radiation. (a) Ionization of water and solvation aqueous electron. (b) Excitation and dissociation of water to create hydroxyl and hydrogen radicals. (c) Dissociation of ionized water to produce hydroxyl radicals and hydrogen ions.

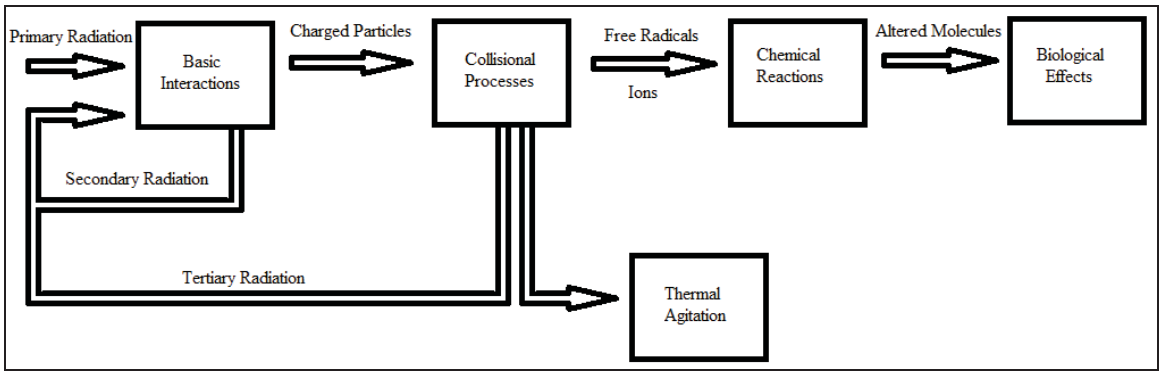

Figure 7. Illustration of the sequence of events from incident ionizing radiation to subsequent biological effects, adapted from reference.[21]

Homogeneous water phantoms with gas-filled ionization chambers measure the collected ionizations within a small volume, allowing for conversion to dose, and are routinely used for the calibration of medical linear accelerators.[28] Such methods are robust and well suited for point measurements; however, use of water-equivalent gel dosimeters for spatial dosimetry is well established.

1.1.4 Gel Dosimetry

When a material is used as a tissue simulant it is referred to as a substitute; a volume of tissue substitute is referred to as a phantom. When selecting a tissue substitute, the primary characteristics of interest are the radiation interactions and the dosimetric quantities one seeks to obtain.[29] With an effective atomic number nearly that of water, many gels are suitable tissue-substitutes and phantom materials for radiation dosimetry.

Gel dosimeters are tissue-like in composition and effective atomic number, with the ability to adjust to nearly any atomic number by use of additions.[30] As chemical detection methods, gel dosimeters contain an active chemical detector element in solution. Gels typically consist of two components: a liquid, most often water, and a dispersed colloidal solid.[31] Derived from the Greek word for glue, colloids are solutions of small particles. Gels are attractive for use in three-dimensional radiation detection and measurement.

Classified by their liquid, aqueous hydrogels are a suitable tissue substitute and possess a multi-dimensional lattice structure capable of retaining spatial information about distributions of chemical products. It has been demonstrated that for a number of gel dosimeters, the deviation from water was less than the difference from water to soft tissue and muscle.[29] The primary organic gelling agents with a history of use in radiation dosimetry are gelatin and agar.

Gelatin is a proteinaceous substance derived from degraded animal collagen, the primary constituent of skin, bone, and connective tissue. Agar is derived from seaweed; agarose is

an isolated polysaccharide possessing the highest gelling potential. Both gelatin and agarose have the ability to form hydrogels with low percentages of the gel agent. Agarose is translucent and scatters light, while gelatin is transparent. When investigated with optical systems, it has been reported that the opacity of agar makes it less than ideal as a gel dosimeter.[32]

The use of gels as rigid support for chemical dosimetry systems was originally investigated with colorimetric radiation sensitive dyes such as methylene blue, which changes color in response to reduction by ionizing radiation.[33-36] Additional investigations by Andrews et al. studied chloral hydrate in agar.[37] Gevantman and Pestaner studied trichloroethylene in agar and obtained the first patent of three-dimensional dosimetry.[38-40]

Ferricyanide in gelatin, Fricke-type dosimeters where iron atoms are reduced by ionizing radiation, were initially investigated with colorimetric methods and later analyzed with magnetic resonance imaging (MRI).[31,41-42] Polymer systems were studied later and presently leuco-dye systems are being actively explored.[16,18,43-44] The most recent development has been application of radio-fluorogenic polymers, where maleimido-pyrene is brought into the growing chain of tertiary-butyl acrylate resulting in the loss of an alkene, providing a shift in the electronic structure and yielding a fluorescent product.[45-48]

As reviewed, gel dosimetry has continued to develop since its inception and there are now many existing systems. Limitations of current three-dimensional gel dosimeters are rapid diffusion with Fricke-type, toxic constituents with polymers, complex fabrication methods with leuco-dyes, and the insolubility of radio-fluorogenic maleimido-pyrene in water.[11,48-50] The search for the ideal gel dosimeter continues.

1.1.5 Current Study

Radio-fluorogenic dosimetry allows for measurement of ionizing radiation by the observation of molecular fluorescence. Molecular absorption of visible and near-visible photons may result in excitation; fluorescence is the de-excitation through prompt emission of a lower energy photon.[19] Some energy is lost in the transfer, resulting in a wavelength shift referred to as the Stokes shift; this allows for discrimination between excitation and emission light.

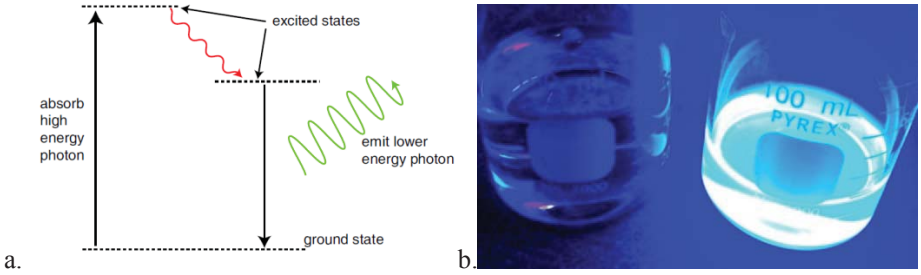

Figure 8. (a) Joblonski diagram showing absorbance resulting in a transition from ground to excited state with fluorescence occurring during the transition back to ground state.[51] (b) Image of a beaker of water next to a solution of coumarin-3-carboxylic acid illuminated by 365nm UV light, the solution of coumarin-3-carboxylic acid clearly demonstrates a visible cyan fluorescent emission.

Chemical dosimetry studies first reported on the quantification of phenolic products of irradiated aqueous benzene and benzoate as a measure of absorbed dose.[52] It was

subsequently shown that hydroxylation was due to the hydroxyl free radicals formed by water radiolysis.[53] Armstrong and Grant further explored the benzoate system with the application of fluorescence spectroscopy for determination of the salicylic acid product.[54]

Reacting by electrophilic substitution, aqueous solutions of aromatic compounds are hydroxylzed in response to irradiation. Personal communication revealed previous unpublished studies on an agar-based benzoic acid system.[55] With limited reports of hydrogel-based radio-fluorogenic detector systems, it was determined this avenue of investigation warranted further study.

The application of C3CA as a chemical dosimeter is an active area of research with several reports of use in aqueous solutions.[56-58] Collins et al. reported on aqueous C3CA as a chemical dosimeter for radiotherapy.[59] Positive characteristics were reported to include reproducibility, stability, and a linear dose range.

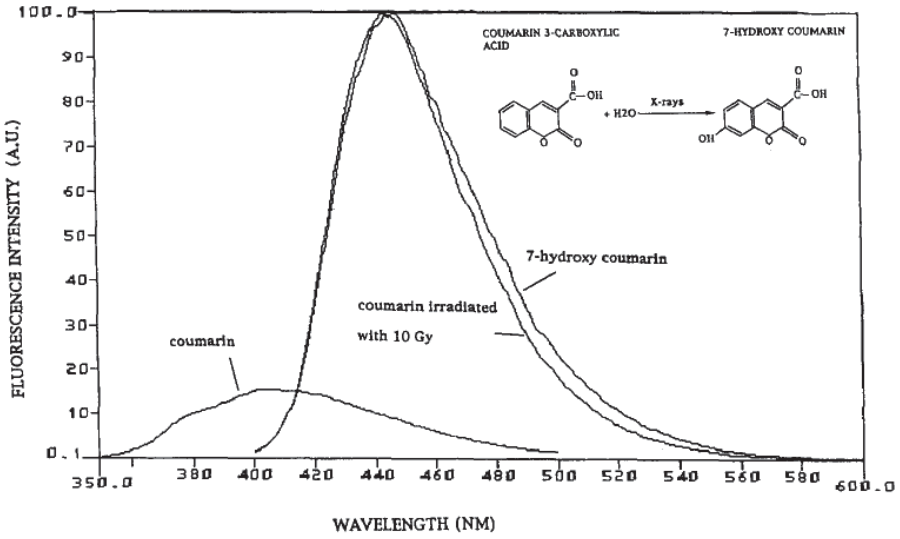

Figure 9. Illustrates the spectral fluorescent response of aqueous solutions of C3CA (labeled coumarin), C3CA irradiated with 10 Gy, and a stock solution of 7HC3CA (labeled 7-hydroxy coumarin). Inset is the basic reaction showing the subsequent product.[59]

First synthesized in 1886 from a mixture of salicylaldehyde, malonic acid, and undiluted acetic acid, C3CA is a stable compound that exhibits little decomposition upon boiling in water or melting.[60] Hydroxylation of C3CA yields 7-hydroxycoumarin-3-carboxylic acid (7HO-C3CA), a derivative of the known fluorescent probe umbelliferone. Umbelliferone is known to have a pH-dependent response.[61]

The current studies were undertaken to investigate characteristics of C3CA in gelatin for application as a water-equivalent radiation detector with respect to fluorescent yield, excitation, and emission spectra. The radiation response of the fluorescent gel dosimeter was explored and effects of gelatin and coumarin concentrations, as well as pH buffer and storage conditions, were studied. Multi-dimensional spatial distributions and methods of analysis were investigated experimentally and theoretically.

1.2 Objectives and Specific Aims

The promise of gel dosimetry is the achievement of a fully integrating three-dimensional dosimeter with tissue-like properties. The objective of this research was the development of a complete radio-fluorogenic gel dosimetry system for the determination of spatial distributions of absorbed dose.

Aim #1: Development of a gelatin-based radiation dosimeter exhibiting a functional dose-response relationship for practical application in radiotherapy. Hypothesis: A reliable radiation dosimeter can be produced by using radio-fluorogenic compounds in gelatin reacting in a predictable manner with hydroxyl free radicals formed by ionizing radiation.

Aim #2: Application of the fluorescent gel dosimeter for the determination a two-dimensional spatial pattern of energy deposition for beams of photons and electrons relevant to radiotherapy. Hypothesis: The spatial pattern of energy deposition in a gelatin dosimeter can be determined by analyzing the distribution of fluorescent intensity after irradiation.

Aim #3: Investigation of the theoretical principles of the dosimetric system with regard to three-dimensional dose distributions of fluorescent products. Hypothesis: Design a hypothetical reader to determine distributions of energy deposition in a volume of gel dosimeter.

References

1. A. Jemal, "Global cancer statistics," CA: A cancer journal for clinicians 61(2), 69 (2011).

2. P. Hoskin, *External Beam Therapy* (Oxford University Press, 2012).

3. M. Samiei, "Challenges of making radiotherapy accessible in developing countries," Cancer Control 85 (2013).

4. J. H Martin, E. A. Evans, et al., "Accuracy in Radiotherapy," Radiology 75(4), 552-558 (1960).

5. A. Brahme, "Dosimetric Precision Requirements in Radiation Therapy," Acta Oncologica 23(5), 379-391 (1984).

6. N. Agazaryan, T. D. Solberg, et al., Patient-specific quality assurance for the delivery of intensity modulated radiotherapy. Journal of Applied Clinical Medical Physics 4(1) 40-50 (2003).

7. B. D. Kavanagh and R. D. Timmerman, *Stereotactic body radiation therapy* (Lippincott Williams & Wilkins, 2005).

8. E. Schreibmann, A. Dhabaan, et al., "Patient-specific quality assurance method for VMAT treatment delivery," Medical physics 36(10), 4530-4535 (2009).

9. L. S. Chin and W. F. Regine, *Principles and practice of stereotactic radiosurgery* (Springer, 2008).

10. Z. Liepa, K. Auslands, et al., "Initial experience with using frameless image-guided radiosurgery for the treatment of brain metastases," Breast 8, 13 (2012).

11. S. J. Doran, "The history and principles of chemical dosimetry for 3-D radiation fields: Gels, polymers and plastics," Applied Radiation and Isotopes 67, (3), 393-398 (2009).

12. R. J. Senden et al., "Polymer gel dosimeters with reduced toxicity: a preliminary investigation of the NMR and optical dose–response using different monomers," Physics in Medicine and Biology 51(14), 3301 (2006).

13. M. Falk, P. M. Rosenschöld, et al., "Real-time dynamic MLC tracking for inversely optimized arc radiotherapy," Radiotherapy and Oncology 94(2), 218-223 (2010).

14. P. A. Jursinic, R. Sharma, et al., "MapCHECK used for rotational IMRT measurements: Step-and-shoot, Tomotherapy, RapidArc," Medical physics 37, 2837 (2010).

15. Y. DeDeene, "Fundamentals of MRI measurements for gel dosimetry," Journal of Physics: Conference Series, 87 (2004).

16. J. Adamovics, and M. J. Maryanski, "Characterisation of PRESAGE™: A new 3-D radiochromic solid polymer dosemeter for ionising radiation," Radiation Protection Dosimetry 120(1-4), 107-112 (2006).

17. S. Babic, J. Battista, et al., "Three-dimensional dose verification for intensity-modulated radiation therapy in the radiological physics centre head-and-neck phantom using optical computed tomography scans of ferrous xylenol–orange gel dosimeters," International Journal of Radiation Oncology* Biology* Physics 70(4), 1281-1291 (2008).

18. C. Baldock et al., "Polymer gel dosimetry," Physics in Medicine and Biology 55(5), R1 (2010).

19. J. R. Lakowicz, *Principles of fluorescence spectroscopy* (Springer, 2007).

20. D. A. Skoog, F. J. Holler, et al., *Principles of Instrumental Analysis* (Brooks Cole, 1997).

21. D. W. Anderson, *Absorption of ionizing radiation* (Baltimore, MD, University Park Press, 1984).

22. W. R. Hendee and E. R. Ritenour, *Medical imaging physics* (John Wiley & Sons, 2003).

23. J. J. Fitzgerald, G. L. Brownell, et al., *Mathematical Theory of Radiation Dosimetry* (New York, NY, Gordon and Breach Science Publishers, Inc.,1967).

24. R. Evans, *The Atomic Nucleus* (McGraw-Hill Book Company, New York, 1955).

25. G. F. Knoll, *Radiation Deteciton and Measurement* (Hoboken, NJ, John Wiley & Sons, 2005).

26. R. A. Serway and J. W. Jewett, *Physics for Scientists and Engineers with Modern Physics* (Cengage Learning, 2007).

27. Attix, *Introduction to Radiological Physics and Radiation Dosimetry* (Germany, John Wiley & Sons, 1986).

28. C. Jayachandran, "Calculated effective atomic number and kerma values for tissue-equivalent and dosimetry materials," Physics in Medicine and Biology 16(4), 617 (1971).

29. M. Taylor, R. Franich, et al. "The effective atomic number of dosimetric gels," Australasian Physics & Engineering Sciences in Medicine 31(2), 131-138 (2008).

28. P. R. Almond, P. J. Biggs, et al. "AAPM's TG-51 protocol for clinical reference dosimetry of high-energy photon and electron beams," Medical physics 26, 1847 (1999).

29. D. White, J. Booz, et al. "Tissue substitutes in radiation dosimetry and measurement," ICRU Report 44 (1989).

30. C. Washtell, *An Introduction to Radiation Counters & Detectors London* (George Newnes Limited, 1958).

31. J. Gore, Y. Kang, et al. "Measurement of radiation dose distributions by nuclear magnetic resonance (NMR) imaging," Physics in Medicine and Biology 29(10), 1189 (1984).

32. M. A. Bero, W. B. Gilboy, et al., "Tissue-equivalent gel for non-invasive spatial radiation dose measurements." Nuclear Instruments and Methods in Physics Research Section B: Beam Interactions with Materials and Atoms 166-167, 820-825 (2000).

33. M. and G. Stein, "Chemical effects of ionizing radiation in some gels," Journal name, issue number (1950).

34. B. Proctor and S. Goldblith, "Oxidation-reduction dyes as radiation indicators," Nucleonics 7(2), 83 (1950).

35. M. J. Day and G. Stein, "Chemical Dosimetry of Ionizing Radiations," Nucleonics 8(2), 34-45 (1951).

36. S. A. Goldblith, B. E. Proctor, et al., "Evaluation of food irradiation procedures. Quantitative chemical measurements utilizing high energy cathode rays," Industrial & Engineering Chemistry 44(2), 310-314 (1952).

37. H. L. Andrews, R. E. Murphy, et al., "Gel Dosimeter for Depth-Dose Measurements," Review of Scientific Instruments 28(5), 329-332 (1957).

38. L. Gevantman and J. Pestaner, *Depth-dosimetry for 250-kVp x rays by means of a gel-incorporated chemical system* (Naval Radiological Defense Lab., San Francisco, 1958).

39. J. Pestaner and L. Gevantman, *Depth-dosimetry by means of a gel-incorporated chemical system* (Naval Radiological Defense Lab., San Francisco, 1958).

40. L. Gevantman, "Radiation effects in gels," Radiation Research Supplement 2, 608-626 (1960).

41. H. Fricke and E. J. Hart, “The Oxidation of the Ferrocyanide, Arsenite and Selenite Ions by the Irradiation of Their Aqueous Solutions with X-Rays,” Journal of Chemical Physics, 3, 596 (1935).

42. G. Stein and M. Tomkiewicz, “Radiation Chemistry of Gelatin Gels Containing Ferricyanide,” Radiation research, 43(1), 25-33 (1970).

43. M. J. Maryanski et al., “Radiation therapy dosimetry using magnetic resonance imaging of polymer gels,” Medical physics, 23(5), 699-705 (1996).

44. L. J. Schreiner, “Review of Fricke gel dosimeters,” Journal of Physics: Conference Series 3(1), p. 9, (2004).

45. J. M. Warman, M. P. De Haas, and L. H. Luthjens, “High-energy radiation monitoring based on radio-fluorogenic co-polymerization. I: small volume in situ probe,” Physics in medicine and biology 54(10), 3185, (2009).

46. J. M. Warman, M. P. De Haas, and L. H. Luthjens, “High-energy radiation monitoring based on radio-fluorogenic co-polymerization II: fixed fluorescent images of collimated x-ray beams using an RFCP gel,” Physics in medicine and biology, 56(5), p. 1487 (2011).

47. J. M. Warman, M. P. de Haas, et al., "A Radio-Fluorogenic Organic Gel for Real-Time, 3D Radiation Dosimetry," Advanced Materials 23(42), 4953-4955 (2011).

48. J. M. Warman, M. P. De Haas, L. H. Luthjens, and M.L. Hom, “High-energy radiation monitoring based on radio-fluorogenic co-polymerization III: Fluorescent images of the cross-section and depth-dose profile of a 3MV electronbeam,” Radiation Physics and Chemistry, 84, 129-135, (2013).

49. K. McAuley, “The chemistry and physics of polyacrylamide gel dosimeters: why they do and don't work,” Journal of Physics: Conference Series (2004).

50. R. J. Senden, P. De Jean, K. B. McAuley, and L. J. Schreiner, “Polymer gel dosimeters with reduced toxicity: a preliminary investigation of the NMR and optical dose–response using different monomers,” Physics in medicine and biology, 51(14), 3301 (2006).

51. D. Semwogerere and E. R. Weeks, "Confocal microscopy," in *Encyclopedia of Biomaterials and Biomedical Engineering*, edited by G. Wnek, and G. Bowlin (Taylor and Francis, New York, 2005).

52. M. J. and G. Stein, "Chemical Measurement of Ionizing Radiations," Nature 164(1), p. 671-672 (1949).

53. G. Stein and J. Weiss, "Detection of Free Hydroxyl Radicals by Hydroxylation of Aromatic Compounds," Nature 166(4235), p. 1104-1105 (1950).

54. W. A. Armstrong and D. W. Grant, "A Highly Sensitive Chemical Dosimeter for Ionizing Radiation," Nature 182(4637), p. 747-747 (1958).

55. J. B. Sweet, *A tissue-equivalent chemical system for measuring two-dimensional radiation distributions.* Unpublished thesis (University of Cincinnati, 1996).

56. G. L. Newton and J. R. Milligan, "Fluorescence detection of hydroxyl radicals," Radiation Physics and Chemistry 75(4), 473-478, (2006).

57. M. Park, S. C. Moore, et al., "Performance of a coumarin-based liquid dosimeter for phantom evaluations of internal dosimetry," Nuclear Instruments and Methods in Physics Research Section A: Accelerators, Spectrometers, Detectors and Associated Equipment 569(2), 543-547 (2006).

58. T. Maeyama, S. Yamashita, et al., "Production of a fluorescence probe in ion-beam radiolysis of aqueous coumarin-3-carboxylic acid solution—1: Beam quality and concentration dependences," Radiation Physics and Chemistry 80(4), 535-539 (2011).

59. A. K. Collins, G. M. Makrigiorgos, et al., "Coumarin chemical dosimeter for radiation therapy," Medical Physics 21(11), 1741-1747 (1994).

60. C. M. Stuart, "XXXV—Action of cinnamic and salicylic aldehydes on malonic acid," Journal of the Chemical Society, Transactions 49, 365-367 (1986).

61. I. Johnson and M. Spence, Eds., *Molecular Probes Handbook, A Guide to Fluorescent Probes and Labeling Technologies*, 11th ed. (Eugene, OR, Molecular Probes, 2010).

Chapter 2

Water-Equivalent Radio-Fluorogenic Gel

2.1 Introduction

The complexities of modern radiotherapy treatments have encouraged the study of tissue-equivalent gel dosimeters capable of multi-dimensional spatial resolution. Investigation of detectors for application to gel dosimetry is ongoing and experiencing continuous development. Radio-fluorogenic detectors rely on the production of fluorescent products formed in response to ionizing radiation. Fluorescent detection techniques are promising due to their ability to form selective high-resolution images.

The indirect action of ionizing radiation produces reactive oxygen species (ROS). Hydroxyl radicals are the most potent ROS and are responsible for nearly two-thirds of the indirect effect of ionizing radiation, DNA damage, and subsequent biological effects.[1] Dosimetry techniques applied to the detection of hydroxyl radicals offer a possible method for measuring biological response and the biologically effective dose.

Aqueous solutions of aromatic compounds are known to react with hydroxyl radicals through electrophilic substitution to yield hydroxylzed derivatives. Several aromatic compounds are known to be radio-fluorogenic, producing fluorescent products in response to hydroxylation. Investigation of an aromatic radio-fluorogenic detector in tissue-equivalent media is the focus of this study.

2.1.1 Radio-Fluorogenic Detectors

Multiple radio-fluorogenic detectors reacting with hydroxyl radicals have been explored for the detection and measurement of absorbed dose by observation of fluorescence. Aqueous benzoic acid was the first system investigated with fluorescent techniques, demonstrating a reliable chemical dosimeter.[2-4] Benzoic acid reacts with hydroxyl radicals at multiple points, yielding three separate products, of which only salicylic acid is fluorescent. Figure 1 shows aromatic benzoic acid reacting with hydroxyl radicals to form salicylic acid by electrophilic addition at the ortho-postion.

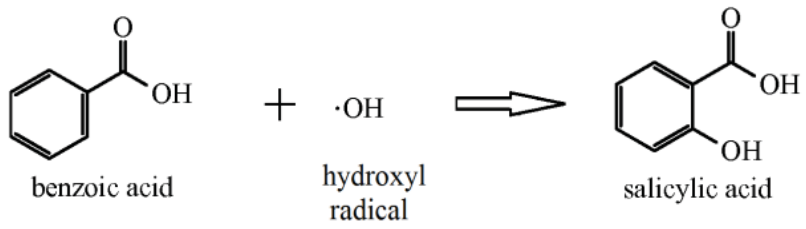

Figure 1. Illustration of benzoic acid reacting with hydroxyl radicals to form salicylic acid, a fluorescent product with maximum excitation near 295nm.

Other compounds include terephthalic, trimesic, and pyromellitic acid.[5-7] Each has increased the yield of fluorescent products by limiting substitution points. Figure 2 shows several compounds applied to radiation dosimetry. Unfortunately, the compounds below possess excitation wavelengths less than ideal for a tissue-equivalent substrate.

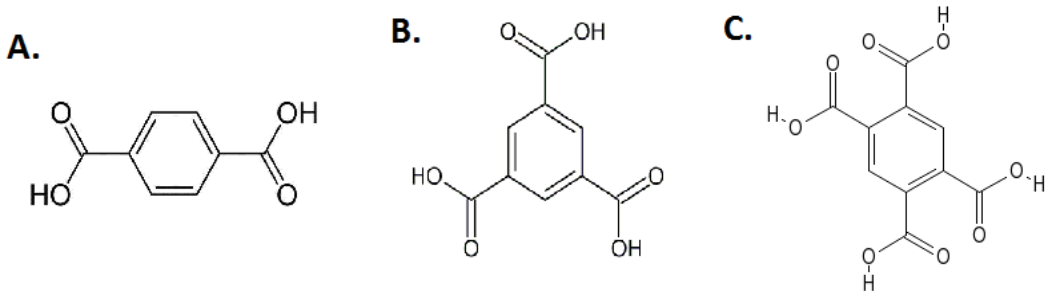

Figure 2. Illustrates the single ring aromatic compounds applied to radiation dosimetry. (a) Terephthalic acid yields a product with maximum excitation near 310nm. (b) Trimesic acid yields a product with maximum excitation near 350nm. (c) Pyromellitic acid yields a product with excitation near 330nm.

Rayleigh scatter is proportional to $1/\lambda^4$, resulting in rapid reduction of transmitted intensity for shorter wavelengths. All biological samples and organic gels are turbid due to the presence of macromolecules that interact with light. For turbid media such as tissue-equivalent gels, it is favorable to use longer wavelengths for excitation, which interact less and penetrate deeper.

When considering aromatic fluorescent compounds with conjugated alternating double-bonds, the overlapping pi orbitals allow for electrons to be delocalized throughout the system; this is known as the resonance effect. The larger the pi electron system, the lower the energy required to excite the compound to fluorescence.[8]

A multi-cyclic, radio-fluorogenic detector yielding a fluorescent product excitable with visible light would be closer to the ideal. A detector possessing this potential, coumarin-3-carboxylic acid (C3CA) has previously been explored in aqueous solution and offers the potential for high-resolution optical imaging when embedded in a tissue-equivalent gel.

2.1.2 Coumarin-3-Carboxylic Acid

Coumarin-3-carboxylic acid (C3CA) is a stable compound exhibiting little decomposition upon boiling in water or melting. As outlined in the previous chapter, in response to an absorbed dose of ionizing radiation, C3CA reacting with hydroxyl radicals forms a fluorescent sensor product, 7-hydroxycoumarin-3-carboxylic acid (7HO-C3CA). A derivative of umbelliferone, 7HO-C3CA is a well characterized fluorescent probe with excitation maximum reported in the 365-385nm range.

Use of C3CA within an aqueous solution as a chemical dosimeter is as an active area of research.[9-11] Aqueous C3CA has been reported as a chemical dosimeter for radiotherapy with favorable characteristics including reproducibility, stability, and linear dose response.[12] Other advantageous features of coumarin include high solubility in aqueous solutions, simple organic composition, and favorable excitation and emission spectra. Figure 3 shows the substitution reaction of C3CA with hydroxyl radicals producing the fluorescent umbelliferone derivative, 7-hydroxycoumarin-3-carboxylic acid (7HOC3CA).

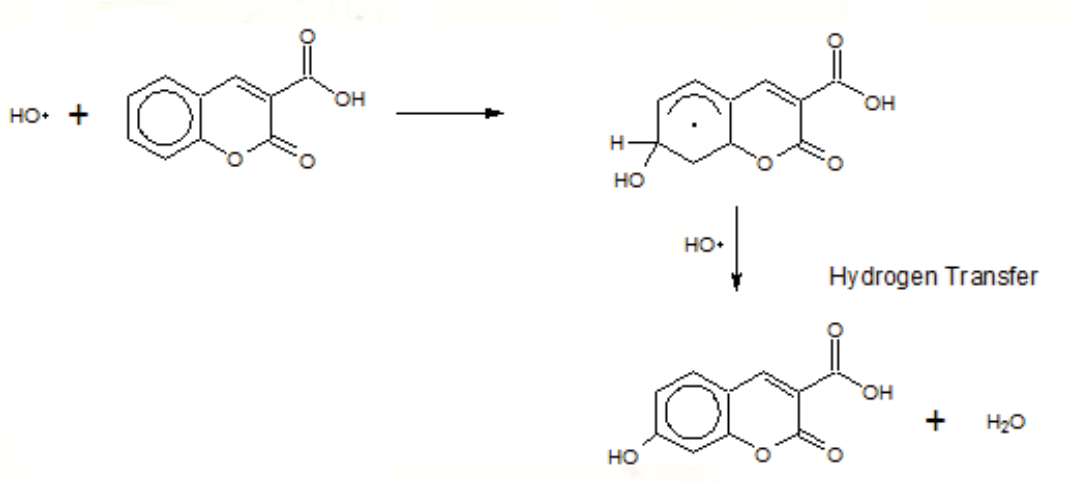

Figure 3. Illustration of coumarin-3-carboxylic acid undergoing hydrogen abstraction and substitution with hydroxyl radicals, yielding fluorescent product 7-hydroxycoumarin-3-carboxylic acid, reported maximum excitation in aqueous solution near 365nm.

Fluorescence is affected by the electronic configuration of orbital electrons within aromatic and heterocyclic rings. Hydrogenation has a direct effect on electronic structure and molecular fluorescence, resulting in decreased delocalization of electrons in the conjugated ring and subsequent reduction of fluorescent yield. Aqueous basic solutions of umbelliferone have been reported to significantly increase fluorescent yield. (Figure 4)

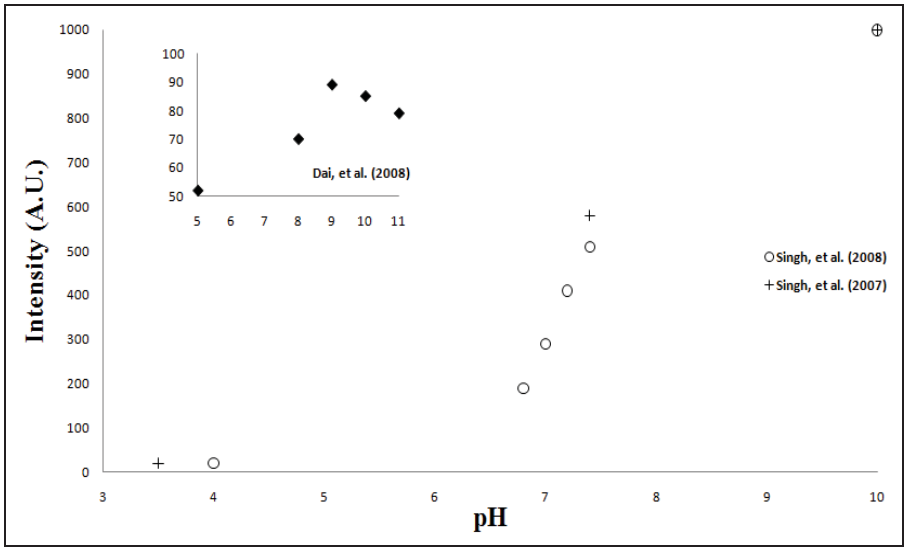

Figure 4. Reported pH dependencies, intensity versus pH, derived from maxima of spectroscopic peaks, both peaks at pH 10 were off scale.[4,13] Inset, plot of Φ versus pH.[14]

2.1.3 Gelatin

Gelatin was selected as being most similar to biological media. Collagen is the most abundant protein in the human body and the primary structural component and organic constituent of skin, bone, and connective tissues. Gelatin is comprised of tropocollagen rods in dimensions of approximately 300nm by 1.5nm diameter; commercial gelatin is derived from animal collagen.[15] Raw organic material is pretreated in either an acidic or basic solution; "Type A" is prepared with hydrogen chloride and "Type B" with sodium hydroxide. It has been shown that type-A, acid-precursor, gelatins are comprised of

multi-chain molecules which are significantly more compact than type-B, alkali-precursor gelatins of similar molecular weight.[15]

Gelatin consists of 18 amino acids in a pseudo-structured series of α-helices, with three major groups: alanine (type A) or glycine (type B) (33-50%), proline or hydroxyproline (25%) with almost a quarter of elements being ionic.[15] Gelatin clarity and transparency is dependent on preparation conditions and the purity and history of raw material. Type A is more compact than type B and possesses a larger intrinsic viscosity.[16] For the current study, Type-A was selected to yield a more rigid gel.

Formation of a rigid matrix occurs through gelation, a process of random interactions between intertwined elements of α-strand triple-helices, at concentrations upon which a critical number of molecular domains overlap (greater than 0.5%). Existing in solution as random coils, the primary structure of gelatin chain elements are characteristic collagen-folds—the result of intramolecular electrostatic interactions, hydrogen and hydrophilic bonding of α-strands in solution. The formation of molecular chain elements is followed by establishment of intermolecular junction points, the secondary structure, which provides an infinite three-dimensional matrix. The ordered nature of gelatin is exhibited by reduced scatter of light with increased concentration. Determined by rate of gelation, structure is a function of formation temperature. With high concentrations or quenching, rapid cooling, random contacts and entanglement occur, resulting in course disordered chain matrices.[17]

Slow gelation allows for a greater degree of chain element organization. Increased lateral bonding and better molecular orientation yield formation of fine well-ordered networks. It is possible to restructure a rapidly cooled gel by tempering, maintaining a temperature near its melting point for an extended period. Tempering allows for the slow transition to a fine well-ordered matrix with stronger cross-links, yielding rigid gels with greater resistance to thermal disruption. Gelation is not susceptible to ionic effects; high pH does not inhibit collagen-fold formation.[15] Figure 5 illustrates the organization of gelatin with the basic triple-helix of tropocollagen magnified; separate chain elements are color coded to allow discrimination.[17]

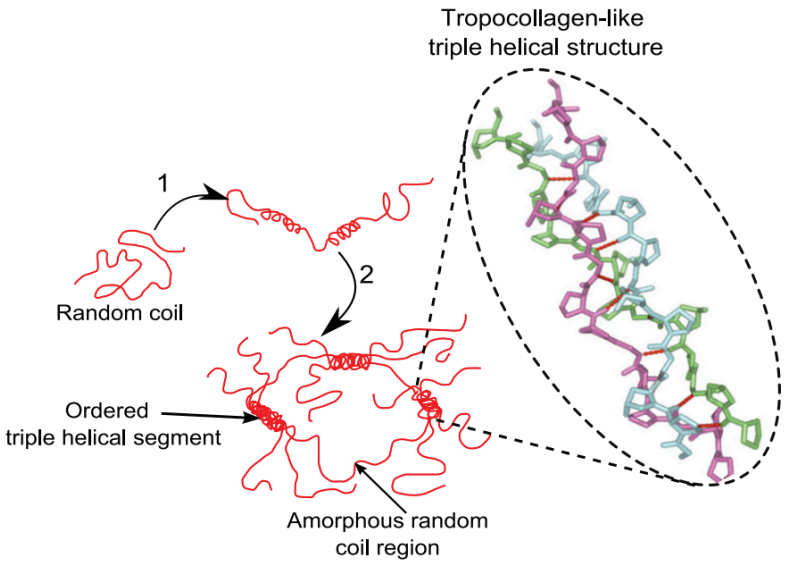

Figure 5. Illustration of gelatin organization with the basic triple-helix of tropocollagen magnified; separate chain elements are color coded to allow differentiation.[17]

2.1.4 System of Study

The current study investigated C3CA in gelatin as a tissue-equivalent radio-fluorogenic detector. With potential for both *in vitro* and *in vivo* measurement coupled with well understood mechanisms of interaction, the C3CA chemical detector offers an attractive avenue of investigation. The radio-product of C3CA, umbelliferone has a known pH-

dependent response. Incorporating an alkali solution in gelatin with radio-fluorogenic C3CA detector has not been investigated so far.

Concentration effects of gelatin and coumarin were explored and the impact of pH buffers in solution was investigated with respect to fluorescent yield and long-term stability. These investigations allowed for establishment of fabrication and storage protocols. Detector response to ionizing radiation was analyzed subject to modality, nominal dose, and dose rate for high energy electron and megavoltage photon energies.

2.2 Methods

All solutions were prepared with filtered and deionized water obtained from EASYpure water purification system (Barnstead International). All reagents were obtained from Fisher Scientific (Baltimore, MD): 98% coumarin-3-carboxylic acid, $C_{10}H_6O_4$ (Acros Organics, Baltimore, MD) and 99% 7-hydroxycoumarin-3-carboxylic acid, $C_{10}H_6O_5$, MW 206.16 (Infodine Chemical Company; Hillsborough, NJ). Phosphate Buffered Saline, sodium bicarbonate, and sodium hydroxide. Food grade, porcine type A gelatin bloom strength (~260), pH (~5), and viscosity (~40) was used.

Samples were fabricated, irradiated, and analyzed by the author. Samples were stored at low temperature (5°C) at all times except during irradiation. Post-irradiation stability was explored with regard to storage conditions and chemical composition. Procedures for fabrication and storage were developed along with protocols for irradiation and calibration.

2.2.1 Fabrication

The general procedure for gel preparation has been determined as follows: to permit effective dispersion, gelatin is allowed to 'wet,' during which the gelatin is placed in a beaker and soaked in with half the total volume of cold distilled water for 15-30 minutes. In a separate beaker, C3CA is brought into solution by bringing a fraction of the total volume to a boil. Following wetting of the gelatin, the radio-fluorogenic solution is added with the remaining fraction of water and the temperature of the gel solution is raised to approximately 35°C and no higher than 40°C since the gelatin may denature. The gel is maintained at approximately 35°C for approximately 90 minutes and is optically clear and free of visible colloidal structures. The solution is then removed from heat and pipetted into sample containers. Gels are left to cool overnight at ambient temperature.

2.2.2 Irradiation

Irradiations were conducted using medical linear accelerators, each providing two nominal megavoltage photon and five electron energies; 6 and 23 mega-volt (MV) and 9, 12, 15, and 20 MV electron energies. Medical linear accelerators possess ionization chamber dose monitors calibrated to the delivery of radiation at a specified depth, typically the depth of maximum energy deposition. For 6MV, this corresponds to a tissue depth of approximately 1.5cm. All machines were in clinical use, with photon and electron beam output routinely monitored and deviations greater than 2% adjusted.[18]

Irradiations were performed with cuvettes arranged as a stack or in bundles. The first arrangement involved placing three cuvettes under a slab of solid water. Electronic equilibrium was identified as a condition of significant concern. When three cuvettes were placed under a slab of bolus (tissue-substitute), the peripheral cuvettes show a marked difference of response than those in the center. The central cuvette exhibited a high signal while peripheral cuvettes under-responded due to a loss of lateral electronic equilibrium.

To minimize the beam time required for irradiations, a stacking method was applied to obtain dose response curves. Studies were initially performed with cuvettes placed between slabs of "plastic water," an acrylic doped with titanium oxide exhibiting an average atomic number similar to water.[19-20] A generalized voxel method was also utilized to obtain a depth dose curve from a free standing stack of 4 rows and 10 columns of cuvettes. Cuvettes were irradiated and the response of each cuvette analyzed by fluorescent spectroscopy, as detailed in the following section.

Further studies were performed using a polystyrene slab containing a void in which 4 cuvettes could be inserted for irradiation. This minimized air gaps and presented favorable geometry for the establishment of electronic equilibrium. A computed tomography (CT) scan was conducted on the acrylic phantom. DICOM format images were imported into Eclipse treatment planning system (Varian Medical Systems; Palo Alto, CA) for dose calculations. Plans were created with and without heterogeneity corrections and demonstrated that the difference in expected dose was <5%. The

computer generated dose distribution from an incident beam of 6MV photons is shown in Figure 6.

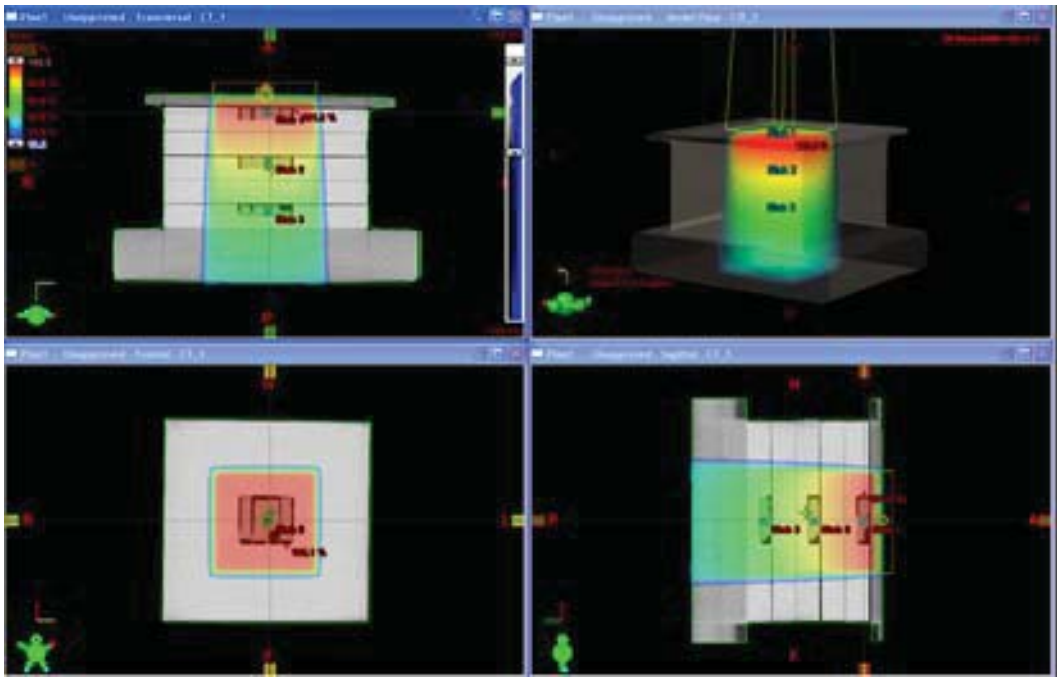

Figure 6. Illustration of the computer generated dose distribution from Eclipse Treatment Planning System, shown is 6MV 10x10cm field delivered 100cm source-to-surface distance to the phantom. Inset in the phantom are three cavities for four cuvettes. The coronal plane shows the surface of the top set of cuvettes.

2.2.3 Analysis

The study of fluorescent products is accomplished using fluorescence spectroscopy, an instrumental method with high sensitivity ($<10_E^{-12}$ mol) and specificity. Initial instrumental analysis was performed in the Connick Laboratory at the University of Cincinnati (Figure 7). Fluorescent analysis was performed with the SPEX Fluorolog-3 (Jobin Yovn – Spex Instruments S.A., Inc.; Edison, New Jersey). The Fluorolog-3 is equipped with a focused 450 W Xenon (Xe) arc lamp encased in housing providing collection and collimation optics for focusing the output. Slits select the bandgap while motorized grating monochromators allowed for selection of wavelength. Xe arc lamps

provide a continuum of light from the ionization and recombination of orbital electrons. Xe possesses a complex emission spectrum with multiple peaks observed near 450nm; correction factors are required for a normalized response. Prohibitively bright for direct observation, the intensity and UV emissions may respectively damage the retina and cornea.

Figure 7. Left. Spex Fluorolog-3 Spectrofluorometer, specifications include a single grating excitation spectrometer, double grating emission spectrometer, photodiode for excitation correction, and R928P photomultiplier tube detector. Front-face (20 degree) collection was used with this system in increments of 1 nm with an integration time of 1s, entrance and exit slits were both set to 5nm. Right, sample chamber with cut-off filter present.

Further instrumental analysis investigations were conducted in the Chemical Sensors and Biosensors Lab at the University of Cincinnati using a Cary Eclipse (Varian, Inc.; Pal Alto, California) fluorescence spectrophotometer equipped with a Xe flash-bulb and fixed right-angle collection. Xe flash lamps possess a more structured spectrum than the arc lamps with higher output in the UV region. Generating less heat and consuming less power, the pulsed nature of excitation results in reduced photobleaching of the samples.

Sensitivity and noise are parameters that must be balanced for any measurement system. Optimization of excitation and emission slit widths allow for manipulation of the signal-to-noise ratio of a flourimeter system. Increasing the excitation or emission slit width increases signal at the cost of spectral broadening, the result of increased noise. Consistent with previous studies in aqueous solution, excitation and emission slit widths were set to 5nm.

Methods of optical analysis are dependent upon sample scattering and absorption properties, which can be significantly affected by imperfections, foreign matter, and dirt on the surface of the cuvette. Investigated materials included quartz, poly-methyl-methacrylate (PMMA), and polystyrene (PS). PMMA and quartz demonstrated superior UV transmittance compared to PS. Quartz crytals were used initially, PS experimented with, and finally PMMA settled as optimal material based on cost and transmittance for near-UV spectral studies.

Data acquisition was optimized using both excititation and emission scans of samples. Scans allowed for determination of optimal wavelengths. Emission scans were conducted and peak emission values recorded and plotted. The dose response was obtained by plotting intensity of 445nm emission against nominal dose. Response was defined as the normalized fluorescent intensity at 445nm.

For the Xe arc lamp, system performance was checked by excitation scans of the xenon lamp showing broadband visible emission around 450nm with a peak at 467±0.5nm and

emission scans of deionized water showing the Raman spectrum with a peak at 397±0.5nm (See Figure 8). For the experiments using the Xe flash bulb, no standard was applied and only relative measurements were determined.

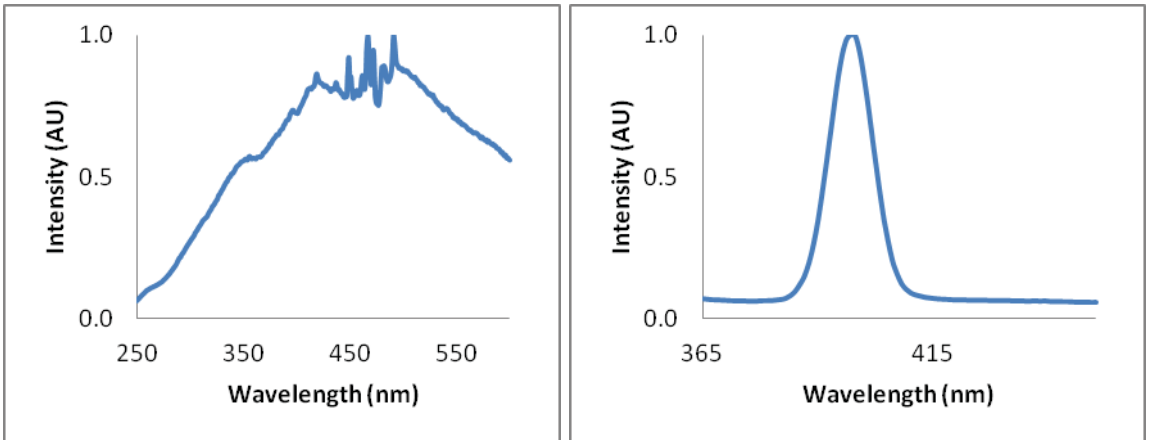

Figure 8. Left. Illustration of Xenon lamp spectral response by comparing intensity of measurements on lamp and detector functionality could be assessed. Right. Raman scatter peak of water, examination of peak location verified correct spectral response of the spectrofluorimeter.

2.3 Results & Discussion

Results of measurements with C3CA in gelatin as a radio-fluorogenic detector are reported with respect to fluorescent yield, excitation and emission spectra. Effects of pH buffer and gelatin concentration as well as storage conditions were explored. The radio-fluorogenic detector response with regard to coumarin concentration and ionizing radiation modality, energy, and rate of irradiation were studied.

2.3.1 Water-Equivalence

The atomic number Z is recognized as the principal characteristic for comparing photon interaction coefficients and subsequent absorption in various materials. This has led to

the development and widespread use of "effective Z" as a measure of a material's radiologic equivalency. Computed linearly by weighted addition, a material is termed "equivalent" if it possesses the same effective Z. Tables 1 and 2 list the elemental composition and chemical formulations, respectively, for the gels evaluated in this study.

Table 1. Elemental composition of the detector constituents and ICRU 44 soft tissue with chemical effective Z and with percent deviation from water and tissue.[21]

Element	Z	A	Water	Soft Tissue	Gelatin	C3CA	7HO-C3CA	NaOH	NaHCO3
Hydrogen	1	1	0.111	0.102	0.108	0.032	0.029	0.025	0.012
Carbon	6	12		0.143	0.020	0.632	0.583		0.143
Nitrogen	7	14		0.034	0.007				
Oxygen	8	16	0.889	0.708	0.858	0.336	0.388	0.400	0.571
Sodium	11	23		0.002	0.000*			0.575	0.274
Phosphorus	15	31		0.003					
Sulfur	16	32		0.003	0.008				
Chlorine	17	35		0.002	0.000*				
Potassium	19	39		0.003					
Iron	26	56			0.000*				
Effective Z			**7.22**	**7.07**	**7.27**	**6.52**	**6.63**	**9.55**	**8.45**
%dev. from water			0.00%	-2.15%	0.64%	-9.73%	-8.20%	32.22%	17.02%
%dev. from tissue			2.19%	0.00%	2.85%	-7.75%	-6.18%	35.12%	19.59%

*elemental constituents of gelatin, while present consist of less than 0.1%

Table 2. Chemical constituents and percent composition for gels studied. Buffered gel refers to sodium hydroxide/bicarbonate. Percent deviation from water and ICRU 44 soft tissue shown.[21]

Constituent	Aqueous Gel	Buffered Gel
Gelatin	7.00%	7.00%
C3CA	0.02%	0.02%
Water	92.98%	92.16%
NaHCO3		0.42%
NaOH		0.40%
Effective Z	**7.226**	**7.241**
%dev. from water	0.04%	0.24%
%dev. from tissue	2.24%	2.44%

The effective Z of the aqueous gel and buffered gel deviated 0.04% and 0.24% from water, respectively. This is less than the deviation from water to tissue. The gels deviated from tissue 2.24% and 2.44% for aqueous and buffered solutions, respectively. This is similar to the 2.19% deviation of water from ICRU 44 soft tissue.[21] These results support the water equivalence and suitability of the gel as a tissue substitute.

2.3.2 Photostability

With each molecular excitation, a fraction of fluorescent compounds are decomposed. This decomposition is commonly described as photo-bleaching and results in a decreased signal response following extended periods of excitation. Photo-bleaching was evaluated using repeated scans of a fluorescent sample. Response was normalized from the 445nm emission of 10 successive 1-min scans with Xenon arc lamp. Figure 9 shows minimal photodecomposition of the fluorescent product.

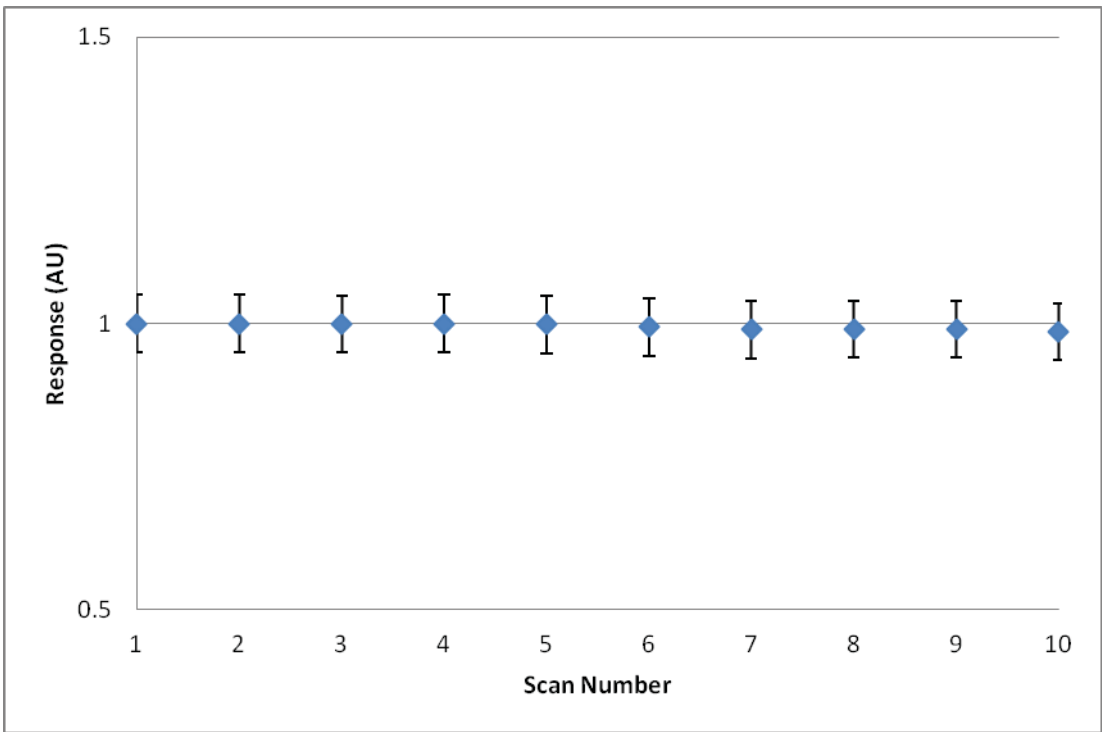

Figure 9. Plot showing the normalized response at 445nm, the result of multiple of continuous emission scans with a Xenon arc lamp. A pronounced lack of photobleaching is observed. Error bars represent a nominal 5% relative error.

These results are in agreement with previous reports of photostability. For aqueous solutions of 7HOC3CA, light dependencies have been demonstrated to be minimal under both diffused sunlight and fluorescent light with stable responses up to 35 and 40 days, respectively. However, solutions were unstable if exposed in direct sunlight for a prolonged period (3 hours).[22] Storage of gelatin-based samples under ambient conditions is prohibitive due to growth of microbes.

2.3.3 Gelatin Concentration

Initial concentration studies contained no coumarin to evaluate storage conditions. Solutions of gelatin in the concentration range of 4-7% gelatin by weight were prepared in deionized water and placed into cold storage (5°C) or left exposed to ambient

conditions (20°C). Ambient samples exhibited microbial growth with no apparent dependency on concentration. Samples stored at low temperature demonstrated no microbial growth; however, with gels of 4% and 5% concentration, freeze fracture crystallization and subsequent destruction of optical integrity was observed (Figure 10); 6% and 7% concentrations remained optically transparent.

Figure 10. Left, illustration of effects of low temperature (5°C) storage, 4% and 5% gelatin by weight exhibited freeze fracturing. Right, individual cuvettes illustrating freeze fractured and intact samples.

Further investigations were conducted with solutions of 0.9mM C3CA and 0.1mM umbelliferone with 7, 9, and 11% gelatin by weight. Solutions were prepared with umbelliferone to simulate irradiated solutions. Excitation and emission spectra were obtained from various concentrations of gelatin with fluor and 7% blank. Without the fluor, relatively no fluorescence occurs, eliminating concerns of intrinsic fluorescence from aromatic amino acids present in gelatin. Background signal can be attributed to C3CA. The excitation and emission spectra of C3CA/7HOC3CA gels is shown in Figure 11.

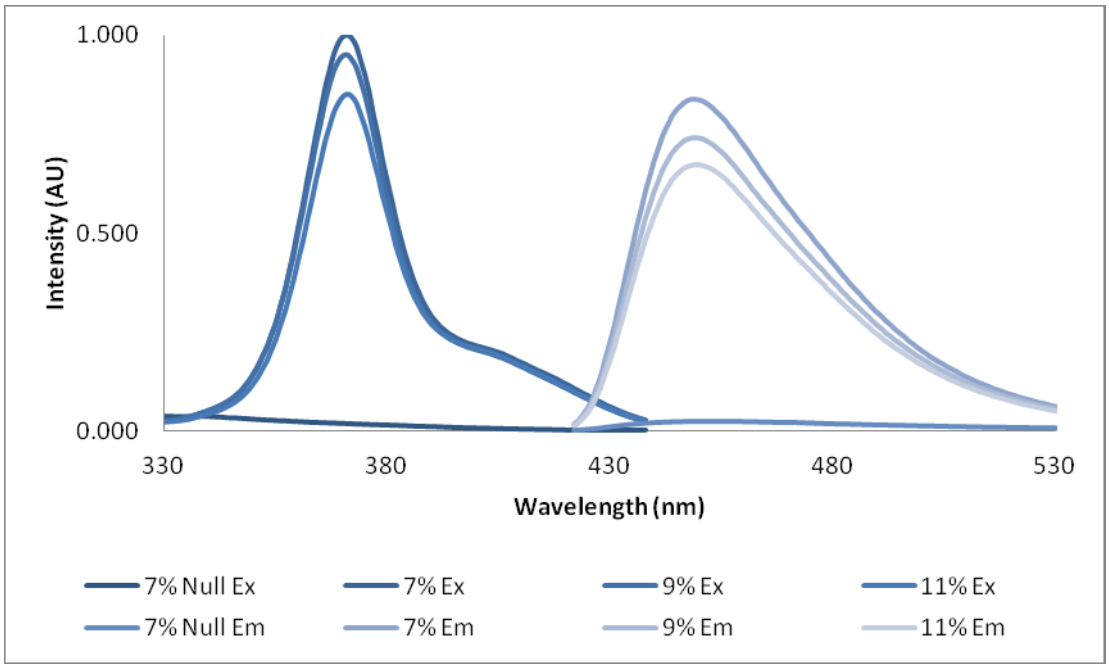

Figure 11. Illustration of excitation and emission spectral response with several concentrations of gelatin. Increased concentration resulted in decreased response. This can be predominately attributed to absorption, previously noted the ordered nature of gelatin results in decreased scattering with increasing concentration. Data included in appendix, Table A1.

Studies demonstrated that low concentrations of gelatin were unsuitable for low temperature storage due to freeze fracturing. High concentrations of gelatin resulted in development of a deep orange hue with increasing concentrations, yielding decreasing fluorescent intensity.

2.3.4 Photon Depth Dose

Dosimeter response was determined by applying published depth dose data for 6MV photon beam to a stacked arrangement of cuvettes. Net normalized results (Figure 10) demonstrate a linear response with a 1mM C3CA detector, 7% gelatin solution. All four cuvettes were used to derive average values with a 1.5% relative standard deviation between samples. An excellent linear fit is demonstrated for the dose range shown, see

Figure 12. Dose values and unit normalized intensity are shown in table 3. The detector response as a function of depth fit with a fourth order polynomial is shown in Figure 13.

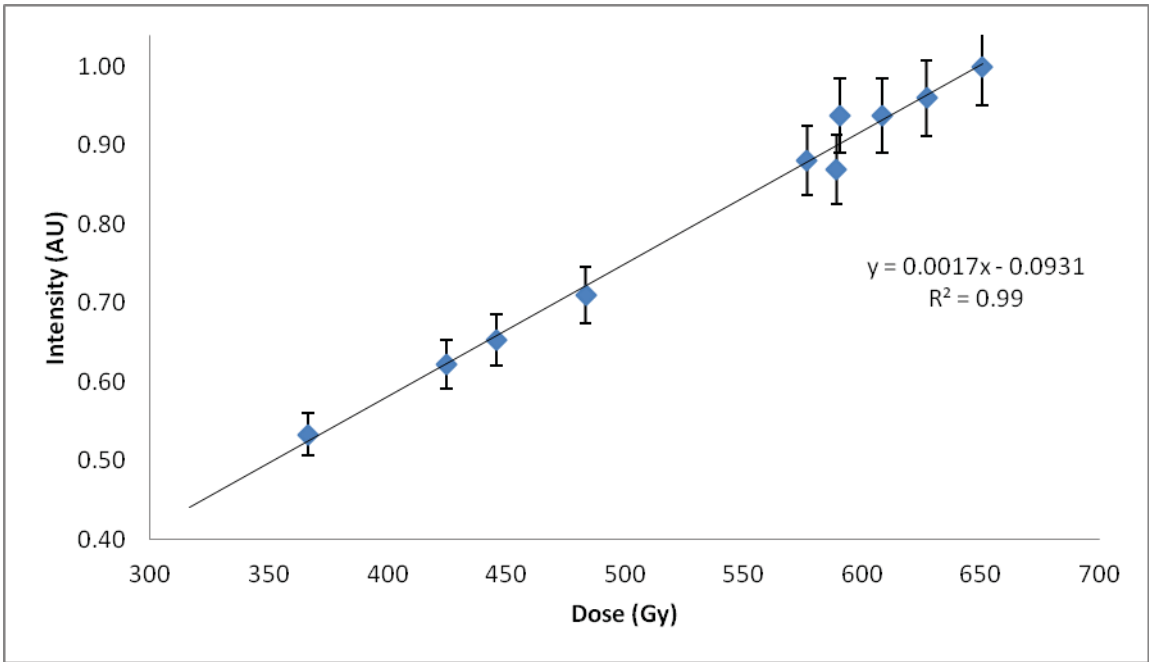

Figure 12. Nominal dose plotted versus normalized intensity. Samples at depth were averaged and background subtracted with nominal 5% relative error bars shown. All four cuvettes were used to derive average values with a 1.5% relative standard deviation between samples. A linear fit is demonstrated.

Table 3. Unit normalized intensity (AU) as a function of dose (Gy) for a stack of cuvettes irradiated with 6MV photons.

Dose (Gy)	Intensity (AU)
651	1.00
627	0.96
609	0.94
591	0.94
577	0.88
589	0.87
484	0.71
446	0.65
425	0.62
367	0.53

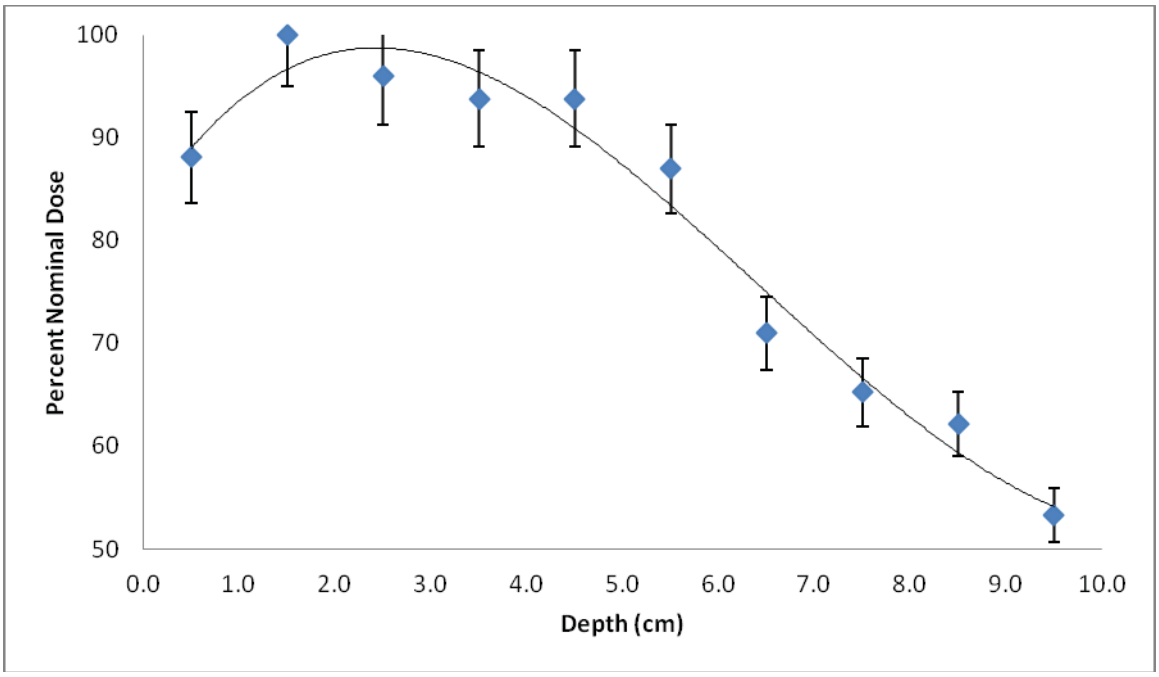

Figure 13. Illustration of detector response expressed as a percentage of nominal doses normalized to maximum value at 1.5cm plotted as a function of depth. Error bars represent a nominal 5% relative error. Curve fit with a fourth order polynomial.

Depth dose data has previously been shown to be an acceptable method for self-calibration and determination of dosimeter response. Relative dose calibrations were obtained with a priori knowledge of the absorbed dose deposited to the material to determine an absolute dose calibration based on the formation of molecular products. The fitting of depth dose curves with fourth-order polynomials is an accepted practice that has shown to provide a reliable fit to experimental and Monte Carlo calculated results.[23] In an attempt to validate the veracity of depth dose response, the data shown in Figure 13 was compared with accepted standard beam data shown in Figure 14.

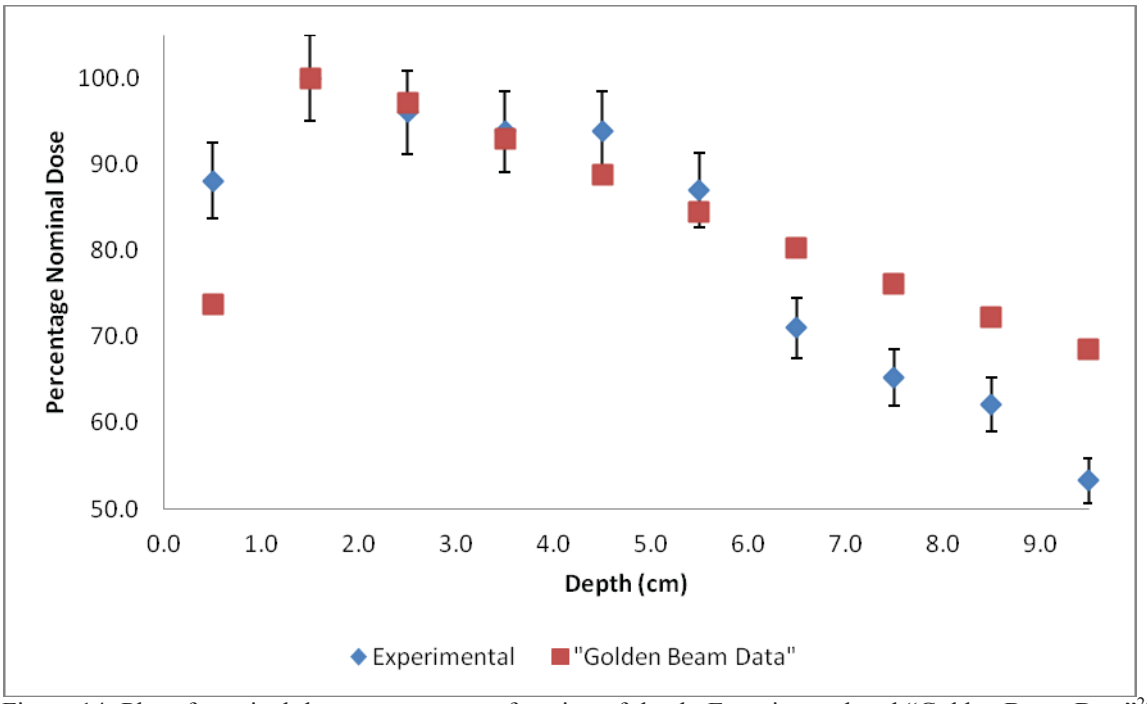

Figure 14. Plot of nominal dose response as a function of depth. Experimental and "Golden Beam Data"[24] error bars represent a nominal 5% relative error. Deviation between the two data sets is observed for depths beyond 5cm.

Table 4. Percent depth dose data derived from experimental measurements plotted alongside "Golden Beam Data."[24] Relatively good agreement (<5%) is found within 1.5-5.5cm with the exception of 4.5cm (5.62%). Larger deviations are observed within the buildup region (0.5cm) and at 6.5cm and beyond.

Depth	Experimental	"Golden Beam Data"	Percent Difference
0.5	88.1	73.8	19.36%
1.5	100.0	100.0	0.00%
2.5	96.0	97.1	-1.11%
3.5	93.8	93.0	0.86%
4.5	93.8	88.8	5.62%
5.5	87.0	84.5	2.92%
6.5	71.0	80.3	-11.58%
7.5	65.2	76.2	-14.38%
8.5	62.2	72.3	-14.01%
9.5	53.3	68.5	-22.22%

The experimental depth dose curve is consistent with beam models that do not account for build-up, the contribution of scatter. Varian "golden beam data" (GBD) is derived from The British Journal of Radiology supplement 25.[24] It must be noted that GBD has

been collected under conditions of full scatter. Caution is required when extrapolating experimental doses from the GBD. The experimental data obtained in this research was collected with cuvettes placed on the table top providing no backscatter. The under-response with depth is not unexpected. This brings the spectral effects of polyenergetic photon beams into the discussion and will be revisited when examining the dose response with depth.

2.3.5 Buffer Effects

Investigations were conducted to determine the effects on fluorescent response of pH buffers in gelatin. Solutions containing phosphate buffered saline (PBS) and sodium bicarbonate with sodium hydroxide were prepared. For studies on the effect of pH, solutions of 7% gelatin were prepared using commercially-available 7HOC3CA as a substitute for the radio-fluorogenic product. Solutions contained 0.9mM C3CA and 0.1mM 7HOC3CA. Figure 15 shows excitation and emission spectra of various buffered and “normal” deionized water solutions of C3CA in 7% gelatin.

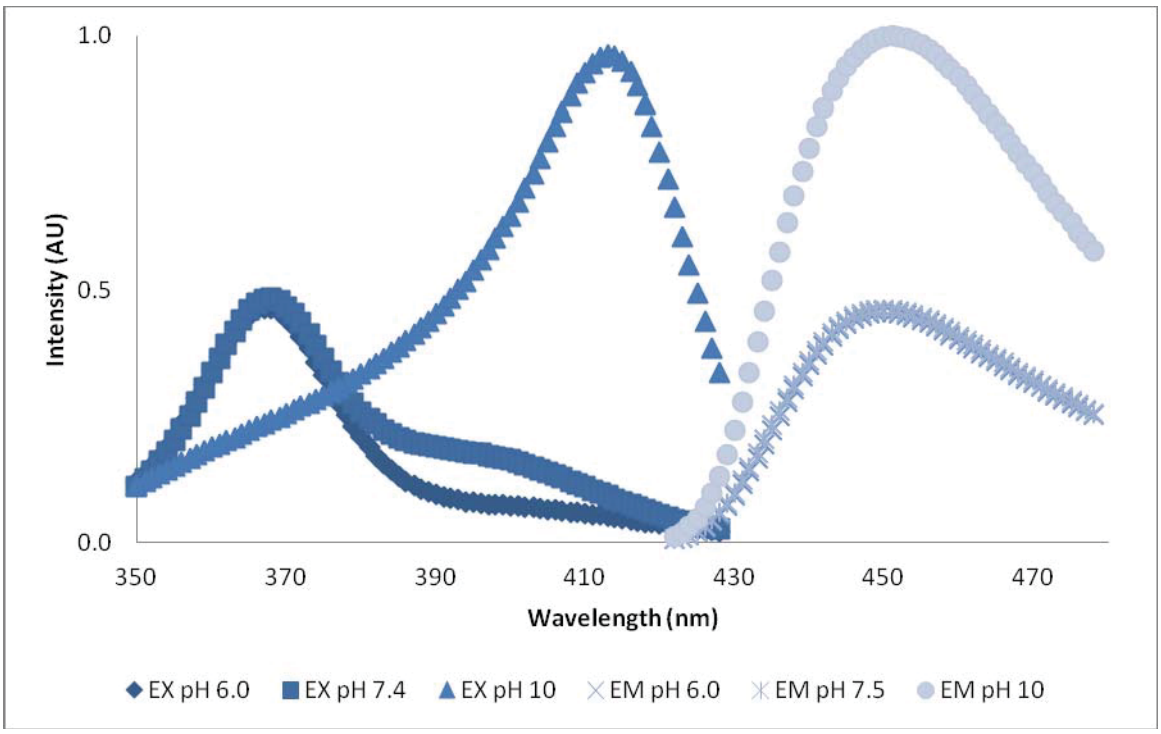

Figure 15. Excitation and emission spectra for three aqueous solutions of 0.9mM C3CA and 0.1mM 7HOC3CA in 7% gelatin. pH 6.0 represents a solution in deionized water, pH 7.4 represents a solution in phosphate buffered saline, and pH 10 represents a solution in sodium hydroxide and sodium bicarbonate A doubling of quantum efficiency is observed as well as a spectral shift of the peak excitation wavelength from 365nm to 405nm for the sodium hydroxide/bicarbonate solution. Spectral data given in appendix, table A2.

These results show that increasing the pH yields a higher effective quantum yield, allowing increased emission intensity with visible light. Studies also demonstrate a spectral shift of the excitation maxima, specifically the peak excitation wavelength shifted from 365nm in normal solutions (pH = 7) to 405nm in basic solutions (pH = 10). The longer wavelength yields increased transmission, which is excellent for application in a tissue-equivalent material.

Typically, only a small fraction of the excitation beam is absorbed by the fluorescent products. Quantum yield or efficiency of the emission process is usually small. The emission intensity is often three-orders of magnitude smaller than the excitation intensity.

In a perfect system, quantum yield approaches unity where all excited molecules fluoresce. Sensitive to changes in the excited state, quantum yield is influenced by the chemical environment, molecular structure, and energy gap. The energy gap, transition between ground and excited electronic states, is strongly influenced by the micro-environment (due to formation of complexes) and molecular motion, collision, rotational and translational diffusion. Large energy gaps typically result in smaller quantum yields due to the availability of other relaxation mechanisms.

The observed decrease in energy gap and subsequent increase in quantum yield are accordant with current theories. The decreased energy gap and resultant spectral shift is consistent with previous studies in aqueous solution, although the shift is larger than previously reported (405nm versus 385nm).[14] The increased spectral shift may be a result of intermolecular interactions between 7HOC3CA and gelatin. Further investigation would be necessary to elucidate these effects.

2.3.6 Concentration Dose Response

All solutions containing coumarin were prepared with 7% gelatin by weight. Solutions of 1mM, 5mM, 10mM, and 20mM C3CA were prepared in sodium bicarbonate/hydroxide buffer. Samples were irradiated in the acrylic phantom shown in Figure 7. Three separate irradiations were used to derive the dose range shown; 100Gy, 200Gy, and 300Gy. Significant increases in range of response were observed with concentrations 5mM and higher, Figure 16. Response, defined as fluorescent intensity divided by dose and normalized to the peak value, demonstrated significant saturation effects in the range

studied (Figure 17). A 10mM concentration of C3CA was selected to investigate the dynamic range of the gel.

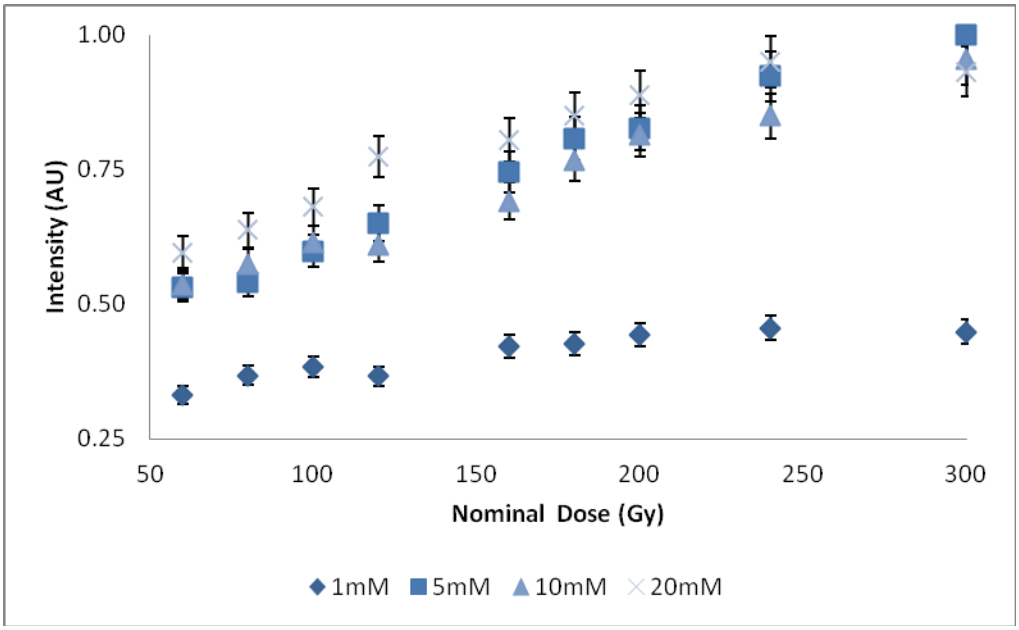

Figure 16. Nominal dose plotted versus normalized intensity for several concentrations of coumarin in 7% gelatin. A significant increase in observable range of response is exhibited for concentrations of 5mM and above. Error bars represent nominal 5% error, repeated measures produced similar uncertainties.

Table 5. Several fluorescent emission intensities normalized to max response for multiple concentrations of coumarin in 7% gelatin.

Dose (Gy)	1mM	5mM	10mM	20mM
60	0.33	0.53	0.54	0.60
80	0.37	0.54	0.57	0.64
100	0.38	0.60	0.61	0.68
120	0.37	0.65	0.61	0.77
160	0.42	0.75	0.69	0.81
180	0.43	0.81	0.77	0.85
200	0.44	0.83	0.82	0.89
240	0.46	0.92	0.85	0.95
300	0.45	1.00	0.96	0.93

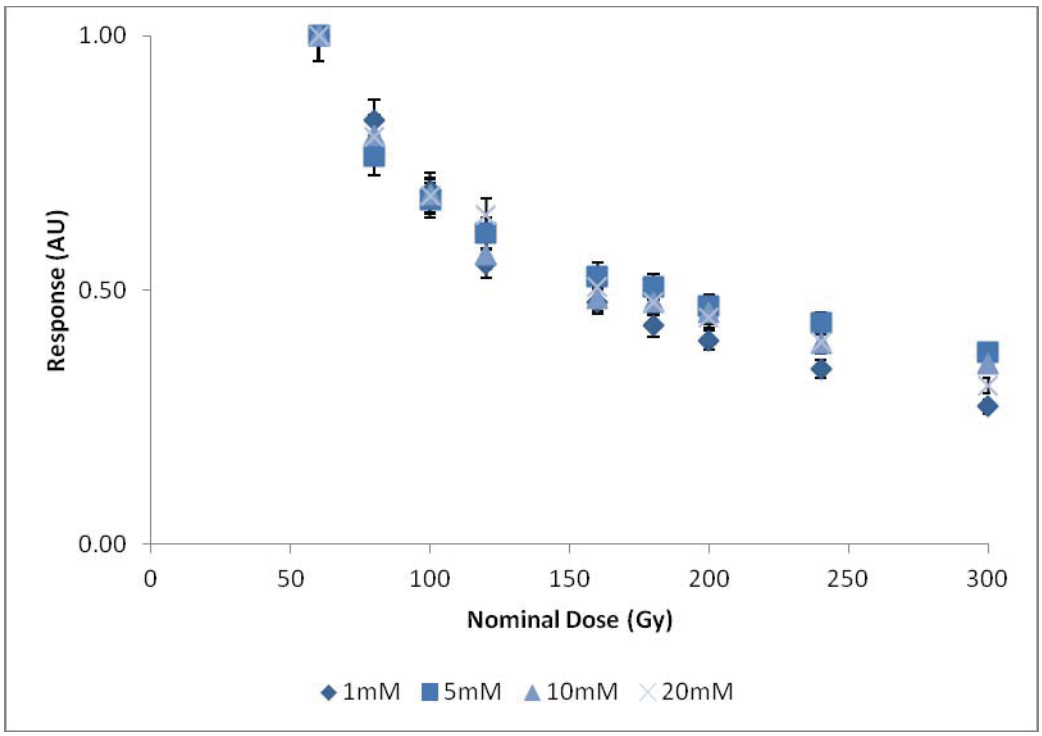

Figure 17. Nominal dose plotted versus normalized response. All concentrations demonstrated a decreasing exponential function indicating saturation effects, i.e. the decreased availability of radio-fluorogenic reactants.

A decreasing exponential curve is evidence of a diminishing population of radio-fluorogenic reactants. These results demonstrate a significant saturation effect within the dose range studied. Saturation effects are defined by the reduction of reactants with increasing intensity of incident radiation. It should be noted that the reduced population of reactants may be a function of the chemical transformation in response to ionizing radiation, or, more likely, the population of reactants available for fluorescence due to the diminishing intensity of incident excitation light with increased concentrations. Setting aside the possibility that the chemical reactants are being exhausted by the incident ionizing radiation, fluorescence inner filter effects will be discussed.

The apparent yield is often less than expected when determining quantum yield based on the intensity of incident light. This may be a result of inner-filter effects, which decrease excitation intensity at points within the volume and/or the resultant emission intensity reaching the detector. Respectively referred to as the primary and secondary inner-filter effects, absorption of the excitation and emission light must be accounted for determination of absolute measurements. The correction for this effect is:

$$F'_{corr} = F'_{obs}\ \text{antilog}\left(\frac{OD_{ex} + OD_{em}}{2}\right)$$

Where OD_{ex} and OD_{em} represent the respective optical density of the excitation and emission wavelengths.[25]

The optical density of a material is proportional to the concentration of the absorbing species. Molecular concentration does not produce a proportional fluorescent response over all ranges of optical densities. Biological samples and phantom materials, like the detector under study are significantly turbid; therefore, incident light of the excitation wavelength may be scattered or absorbed by the chemical constituents, interfering with accurate response. Further investigation of the fundamental processes and determination of extinction coefficients would be necessary for absolute dosimetry.

2.3.7 Dose Response Dependencies

Dose response was studied using samples irradiated with different modalities, energies, and dose rates. Samples were irradiated and the normalized response obtained from 445nm emissions and plotted as a function of nominal dose (see Figure 18). Error bars represent a nominal 5% uncertainty. Repeated measures of four samples for each data

point, all demonstrated less than relative error less than 1% (see Table 6). Dose response was relatively independent of modality (electron, photon) and energy (9 MeV, 6 MV, and 23MV).

Table 6. Data for dose response studies, photon and electron, 6 and 23MV and 9MeV respectively. Dose rates of 1, 3, and 6 (nominal) Gy/min. Irradiation geometry as shown in Figure 2.

Modality	Energy	Monitor Units	Dose Rate (mu/min)	Percent Depth Dose	Nominal Dose (Gy)	Avg Intensity (AU)	Standard Deviation	Relative Standard Deviation	Samples Used
Photon	6MV	5000	600	1.000	50.0	391	1.28	0.33%	1-4
Photon	6MV	5000	600	0.792	39.6	374	1.42	0.38%	5-8
Photon	6MV	5000	600	0.603	30.2	358	1.77	0.50%	9-12
Photon	6MV	5000	600	1.000	50.0	383	2.15	0.56%	13-16
Photon	6MV	5000	600	0.792	39.6	370	1.28	0.35%	17-20
Photon	6MV	5000	600	0.603	30.2	356	0.99	0.28%	21-24
Photon	6MV	5000	600	1.000	50.0	381	2.75	0.72%	49-52
Photon	6MV	5000	600	0.792	39.6	366	1.16	0.32%	53-56
Photon	6MV	5000	600	0.603	30.2	353	1.05	0.30%	57-60
Photon	6MV	5000	300	1.000	50.0	391	2.28	0.58%	25-28
Photon	6MV	5000	300	0.792	39.6	376	0.66	0.18%	29-32
Photon	6MV	5000	300	0.603	30.2	358	1.84	0.51%	33-36
Photon	6MV	5000	100	1.000	50.0	397	3.20	0.81%	37-40
Photon	6MV	5000	100	0.792	39.6	380	0.66	0.17%	41-44
Photon	6MV	5000	100	0.603	30.2	364	2.53	0.70%	45-48
Photon	23MV	5000	600	0.947	47.4	379	1.68	0.44%	61-64
Photon	23MV	5000	600	0.913	45.7	375	0.56	0.15%	65-68
Photon	23MV	5000	600	0.746	37.3	364	0.61	0.17%	69-72
Electron	9MeV	5000	600	0.957	47.9	379	1.32	0.35%	73-76
Electron	9MeV	4000	600	0.957	38.3	366	1.20	0.33%	77-80
Electron	9MeV	3000	600	0.957	28.7	350	1.41	0.40%	81-84
Electron	9MeV	5000	300	0.957	47.9	386	1.18	0.30%	85-88
Electron	9MeV	5000	100	0.957	47.9	394	0.84	0.21%	89-92
Control	N/A	0	0	1.000	0.0	306	0.70	0.23%	93-100

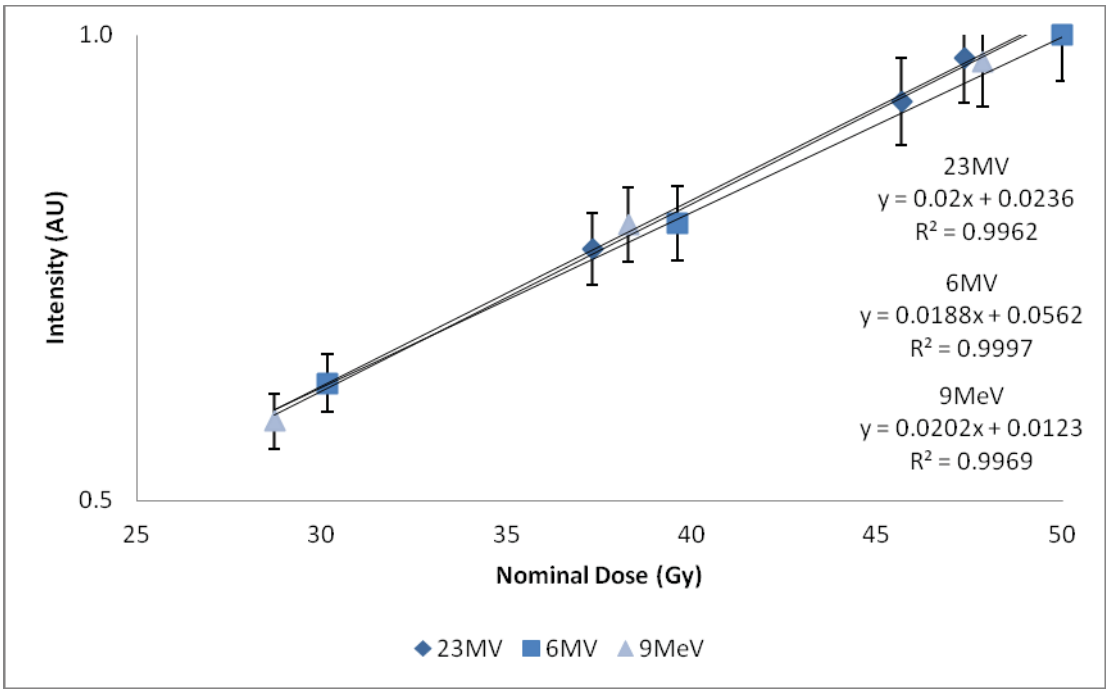

Figure 18. Nominal dose plotted against normalized intensity. All dose response curves show excellent linear fits (R>.99), indicating an energy independent response. Equations inlaid on graph. Error bars represent a nominal 5% uncertainty.

Dose response results were essentially linear for the range of energy and modalities investigated (R>.99). The modality independent response is expected, as photon dose deposition is predominately by delta rays, secondary electrons. Results of normalized energy dependence and modality independent response were in excellent agreement with the dose response curve (Figure 19).

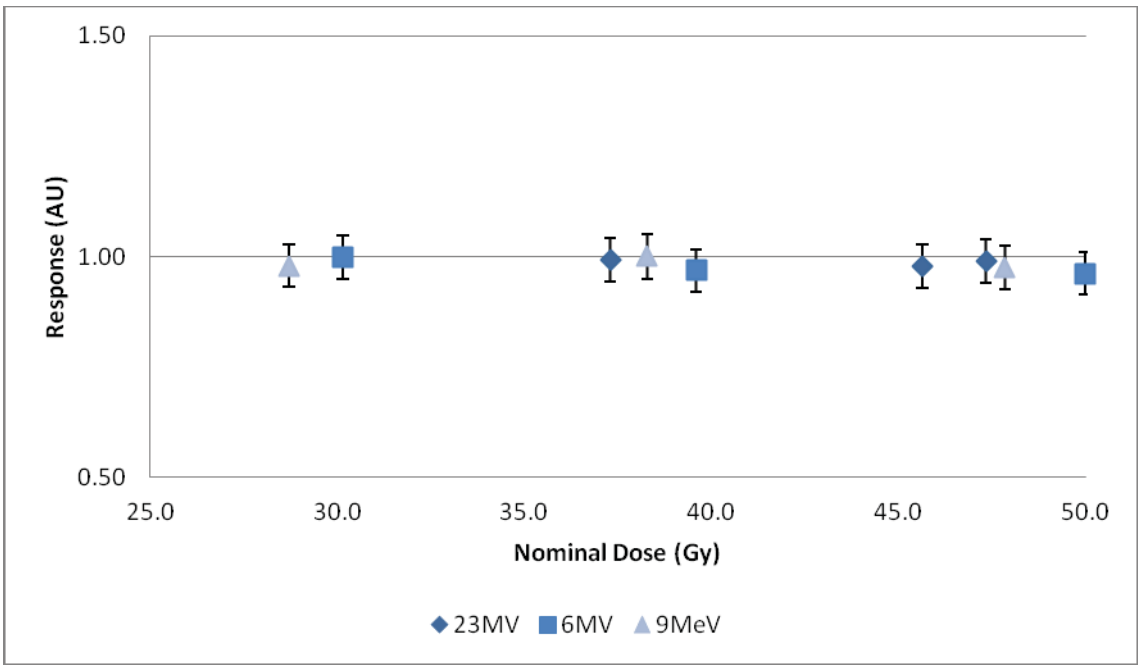

Figure 19. Plot of normalized response versus nominal dose for 23MV, 6MV, and 9MeV beams, error bars represent a nominal 5% relative error.

The results demonstrate a normalized linear response to dose, energy, and modality within 5% for the range studied. This suggests a reliable detector with favorable characteristics for additional study. The next attribute investigated was dose rate response dependencies, which appears to exist for the nominal rates studied (1, 3, and 6 Gy/min), (Figure 20).

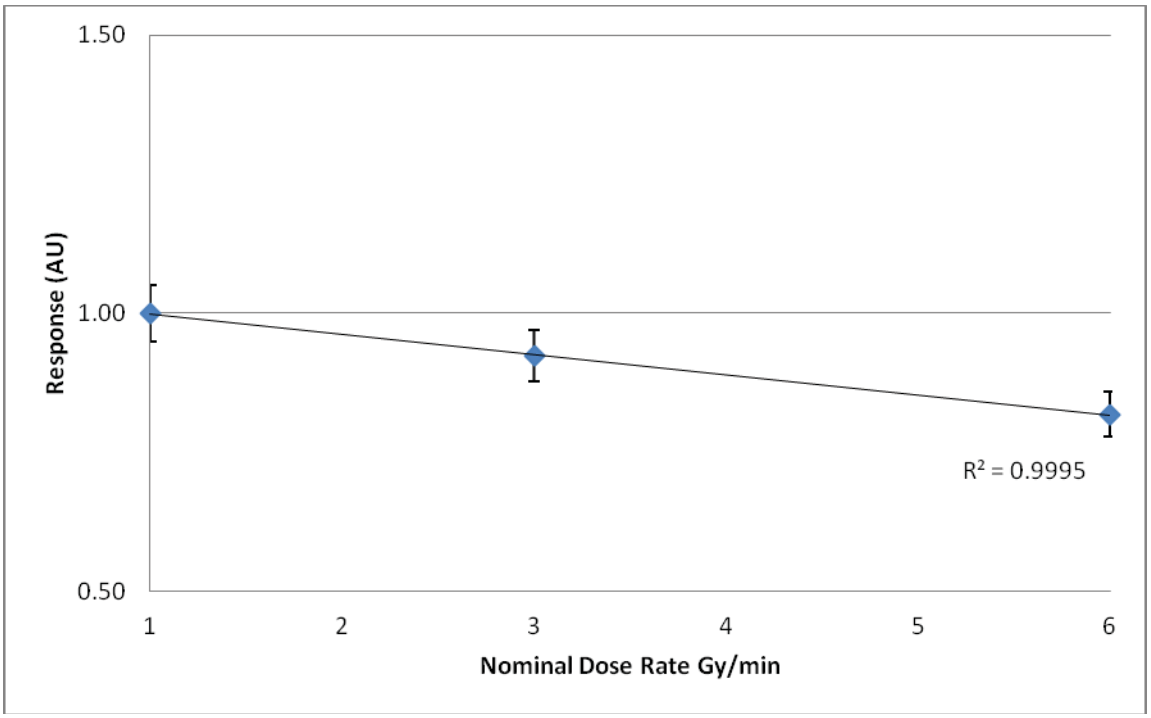

Figure 20. Normalized response plotted versus nominal dose rate show a response as a decreasing function of dose rate. This has been observed in other studies and has been hypothesized to be a result of metallic impurities within the C3CA.

The above results demonstrated a linear dose rate dependency with low dose rates increasing dose response, in agreement with previous studies.[12] The dependency is suggested to be the result of metallic impurities in C3CA and can be mitigated with successive distillations. Performance of distillations was deemed to be beyond the scope of the current study; however, future studies should investigate the feasibility of obtaining higher purity coumarin, either through distillations or purchase of high-grade C3CA. When plotting the normalized dose versus depth, an increasing response was observed, which may be a dose rate effect (Figure 21).

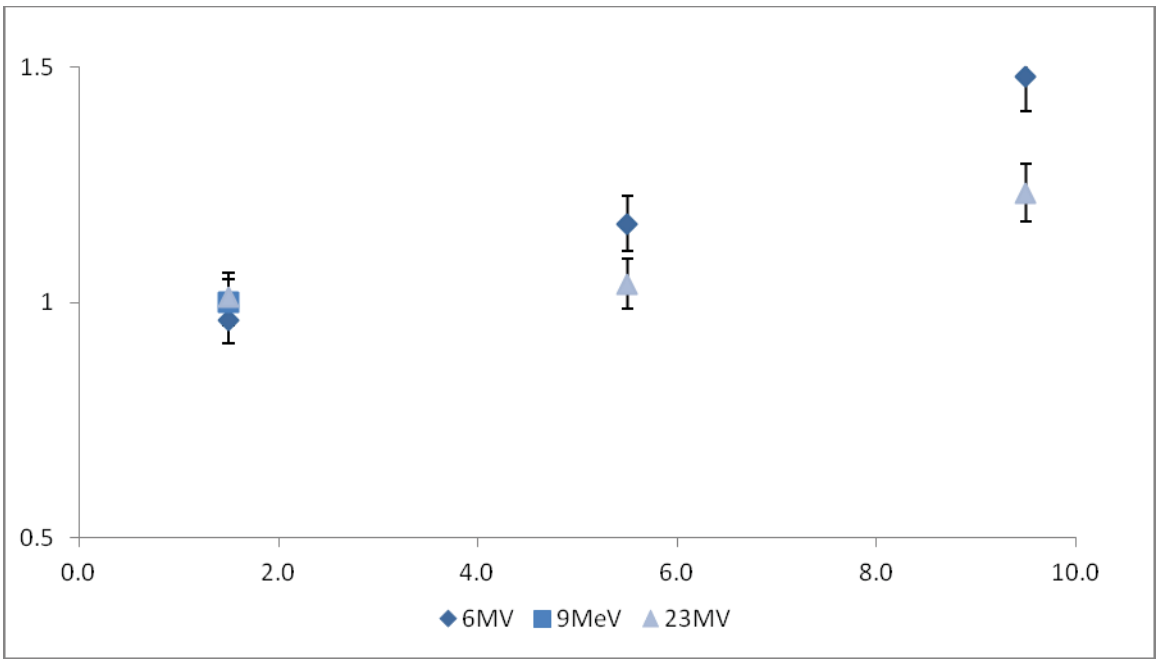

Figure 21. Nominal dose response normalized to 9 MeV and plotted as a function of depth; the photon beams show a slightly increasing response, dependent on energy, with depth.

The above results may demonstrate an energy fluence or total fluence dependent response. This would in effect be an energy-dependent response, which may be due to the presence of metallic impurities possessing a larger effective Z. The minimum detectable amount (MDA) of absorbed dose is assumed to be three times the standard deviation of the background, extrapolated from 9MeV electron data.[26] See Table 7 and Figure 22.

Table 7. Data used for extrapolation of MDA, experimental represents dose response from 9MeV electrons as shown in table 6. Extrapolated nominal dose of 1.5Gy for MDA represents the plotted fit to background response plus three standard deviations. See Figure 20.

Nominal Dose (Gy)	Experimental	Extrapolated
47.9	378.6	
38.3	365.5	
28.7	349.7	
1.5		308.1
0.0	305.5	

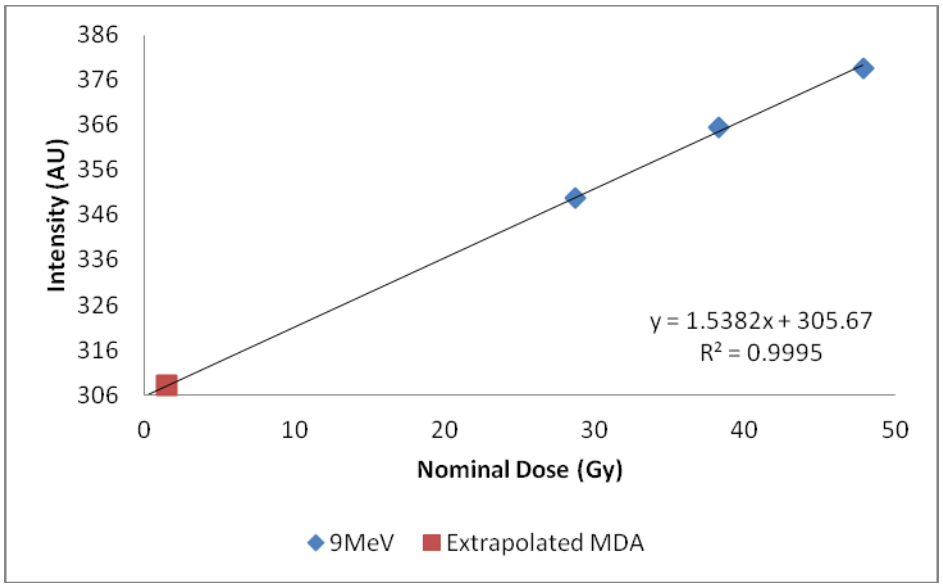

Figure 22. 9MeV dose response plotted with extrapolated MDA. MDA estimated to be 1.5Gy, extrapolated by the addition of three times the standard deviation of background.

As shown above, the estimated MDA is 1.5Gy. This is based on the use of repeated measures with a relative error less than 1%. The presented studies demonstrate the relative dose-response of the detector within a limited range of doses in stacked geometries. Future work could expand the dose range and aim towards determination of absolute efficiencies for dose response.

2.3.8 Stability

The stability of high pH buffered solutions of C3CA was studied. Samples were irradiated with 30Gy and kept in storage. Significant degradation of signal was observed with passage of time, nearly 40% per month in storage (Figure 20).

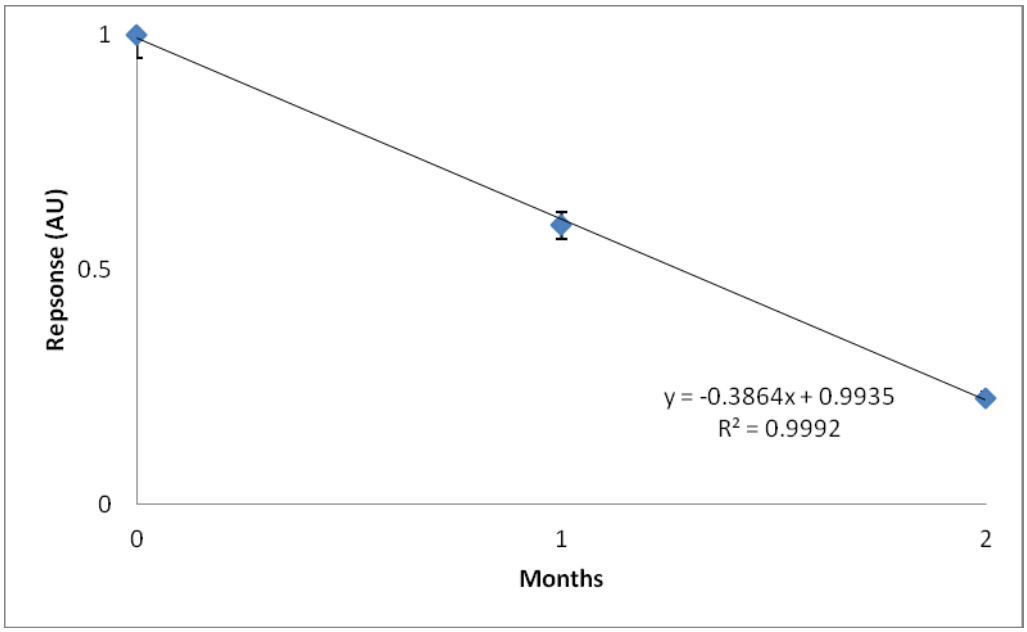

Figure 23. Stability of response plotted as a function of time. Irradiated 30Gy, a linear decrease in signal is observed. Nearly 40% signal loss is observed over the course of one month. This is hypothesized to be a result of decomposition of radio-fluorogenic products in basic solution.

The above results for buffered solutions are in contrast with previous results for aqueous solutions. Manevich et al. reported the stable use of aqueous solutions kept under refrigeration for up to 3 months.[27] The lack of stability of buffered solutions is believed to be the result of decomposition of aromatic molecules within the solution. Further investigation may clarify these effects, although it is believed that a solution of pH 10 is inherently unstable. Future studies should focus on non-buffered solutions which may provide sufficient quantum yield when coupled with intense light sources such as lasers.

2.4 Conclusions

The preceding data and analysis demonstrate the feasibility of a gelatin-based C3CA radio-fluorogenic detector exhibiting a measurable dose-response relationship, supporting the working hypothesis originally proposed. A functional, tissue-equivalent fluorogenic gel dosimeter has been produced by use of C3CA dissolved in gelatin, reacting with hydroxyl free radicals formed by exposure to ionizing radiation. The response of a gelatin-based detector was observed and studied with respect to concentration of chemical constituents, presence of pH buffers, energy deposition, exposure rate, and type of ionizing radiation (photons and electrons).

Within a basic solution, peak excitation wavelength was observed to shift from 365nm to 405nm; the further shift into the visible spectrum provides increased transmission, favorable for application in phantoms. Observation of the wavelength shift suggested applicability of 405nm violet diode lasers for excitation. Due to large-scale manufacturing, inexpensive 405nm violet diode laser sources are readily available.[28] Their application to the detector will be discussed in the following chapter.

References

1. E. J. Hall, *Radiobiology for the Radiologist* (New York, Lippincott Williams & Wilkins, 2000).

2. W. A. Armstrong and D. W. Grant, "A Highly Sensitive Chemical Dosimeter for Ionizing Radiation," Nature 182(4637), p. 747-747 (1958).

3. K. McAuley, "The chemistry and physics of polyacrylamide gel dosimeters: Why they do and don't work," Journal of Physics: Conference Series, IOP Publishing (2004).

4. A. K. Singh, Chen, et al., "Synthesis of Coumarin-Polyamine-Based Molecular Probe for the Detection of Hydroxyl Radicals Generated by Gamma Radiation," Radiation Research 168(2), p. 233-242 (2007).

5. J. C. Barreto, G. S. Smith, et al., "Terephthalic acid: A dosimeter for the detection of hydroxyl radicals in vitro," Life Sciences 56(4), PL89-PL96 (1994).

6. R. W. Matthews, "Aqueous chemical dosimetry," The International Journal of Applied Radiation and Isotopes 33(11), 1159-1170 (1982).

7. R. Nadrowitz, A. Coray, et al., "A liquid fluorescence dosimeter for proton dosimetry," Physics in Medicine and Biology 57(5), p. 1325 (2012).

8. B. Valuer and M. N. Berberan-Santos, *Molecular Fluorescence: Principles and Applications* (Weinheim, Germany, Wiley-VCH, 2012).

9. S. Yamashita, G. Baldacchino, et al., "Mechanism of radiation-induced reactions in aqueous solution of coumarin-3-carboxylic acid: Effects of concentration, gas and additive on fluorescent product yield," Free radical research 46(7), 861-871, (2012).

10. C. C. Perry, V. J. Tang, et al., "Use of a Coumarin-Labeled Hexa-Arginine Peptide as a Fluorescent Hydroxyl Radical Probe in a Nanoparticulate Plasmid DNA Condensate," The Journal of Physical Chemistry B 115(32), 9889-9897 (2011).

11. F. Kroll, J. Pawelke, et al., "Preliminary investigations on the determination of three-dimensional dose distributions using scintillator blocks and optical tomography," Medical physics 40(8), 082104-082104 (2013).

12. A. K. Collins, G. M. Makrigiorgos, et al., "Coumarin chemical dosimeter for radiation therapy," Medical Physics 21(11), 1741-1747 (1994).

13. A. Singh, Y. Yang, et al., "Synthesis and application of molecular probe for detection of hydroxyl radicals produced by Na125I and gamma-rays in aqueous solution," International Journal of Radiation Biology 84(12), p. 1001-1010 (2008).

14. X. Dai, E. Rollin, et al., "Wavelength shifters for water Cherenkov detectors," Nuclear Instruments and Methods in Physics Research Section A: Accelerators, Spectrometers, Detectors and Associated Equipment 589(2), p. 290-295 (2008).

15. A. Veis, *The Macromolecular Chemistry of Gelatin* (New York, NY, Academic Press, 1964).

16. K. B. Djagny, Z. Wang, and S. Xu, "Gelatin: a valuable protein for food and pharmaceutical industries: Review," Critical reviews in food science and nutrition, 41(6), p. 481-492 (2001).

17. M. Roussenova, J. Enrione, et al., "A nanostructural investigation of glassy gelatin oligomers: molecular organization and interactions with low molecular weight diluents," New Journal of Physics 14(3), 035016, (2012).

18. E. E. Klein, J. Hanley, et al., Task Group 142 report: Quality assurance of medical acceleratorsa, Medical physics, 36(9), p. 4197-4212 (2009).

19 V. Tello, R. Tailor, et al., "How water equivalent are water-equivalent solid materials for output calibration of photon and electron beams?" Medical physics 22, p. 1177 (1995).

20. R. F. Hill, S. Brown, and C. Baldock, "Evaluation of the water equivalence of solid phantoms using gamma ray transmission measurements," Radiation Measurements, 43(7), p. 1258-1264, (2008).

21. D. R. White, J. Booz, et al., Tissue substitutes in radiation dosimetry and measurement. ICRU Report, 44, pp. ## (1989).

22. H. Khan, M. Anwar, et al., "Effect of temperature and light on the response of an aqueous coumarin dosimeter," Journal of Radioanalytical and Nuclear Chemistry 200(6), p. 521-527 (1995).

23. T. F. Lisanti, "Calculating electron range values mathematically," Radiation Physics and Chemistry 71(1), p. 581-584 (2004).

24. T. Jordan, "Megavoltage X-ray beams: 2-50 MV," BJR supplement/BIR 25, p. 62 (1996).

25. J. R. Lakowicz, *Principles of fluorescence spectroscopy* (Springer, 2007).

26. P. E. Metcalfe, T. Kron, et al., "The physics of radiotherapy x-rays and electrons," Journal name, Vol(iss), p. ## (2007).

27. Y. Manevich, K. D. Held, and J. E. Biaglow, “Coumarin-3-carboxylic acid as a detector for hydroxyl radicals generated chemically and by gamma radiation,” Radiation research, 148(6), p. 580-591 (1997).

28. A. A. Bergh, "Blue laser diode (LD) and light emitting diode (LED) applications," Physica status solidi (a) 201(12), p. 2740-2754 (2004).

Appendix

Table A1. Fluorescent excitation (Ex) and emission (Em) spectra of multiple concentrations of gelatin.

Wavelenth (nm)	7% Null Ex	7% Ex	9% Ex	11% Ex	7% Null Em	7% Em	9% Em	11% Em
322	0.032	0.017	0.018	0.015				
323	0.033	0.018	0.019	0.016				
324	0.033	0.019	0.020	0.016				
325	0.034	0.020	0.021	0.017				
326	0.035	0.020	0.022	0.018				
327	0.036	0.022	0.023	0.020				
328	0.037	0.023	0.025	0.021				
329	0.038	0.024	0.026	0.022				
330	0.038	0.026	0.027	0.023				
331	0.038	0.027	0.028	0.024				
332	0.038	0.028	0.029	0.025				
333	0.037	0.029	0.031	0.026				
334	0.037	0.031	0.033	0.027				
335	0.037	0.034	0.035	0.029				
336	0.038	0.036	0.038	0.032				
337	0.038	0.040	0.041	0.035				
338	0.038	0.043	0.045	0.038				
339	0.038	0.047	0.049	0.041				
340	0.038	0.050	0.053	0.044				
341	0.037	0.055	0.058	0.048				
342	0.036	0.060	0.063	0.052				
343	0.036	0.065	0.068	0.056				
344	0.035	0.071	0.074	0.061				
345	0.034	0.079	0.082	0.068				
346	0.034	0.088	0.091	0.075				
347	0.033	0.098	0.101	0.084				
348	0.032	0.112	0.114	0.094				
349	0.032	0.127	0.130	0.107				
350	0.031	0.144	0.146	0.121				
351	0.030	0.164	0.167	0.138				
352	0.029	0.187	0.189	0.157				
353	0.029	0.212	0.215	0.179				
354	0.028	0.242	0.244	0.205				
355	0.028	0.275	0.277	0.234				
356	0.027	0.314	0.314	0.267				
357	0.027	0.356	0.355	0.303				
358	0.026	0.403	0.401	0.342				
359	0.025	0.458	0.450	0.386				
360	0.025	0.514	0.503	0.433				
361	0.024	0.570	0.557	0.480				
362	0.024	0.631	0.613	0.531				
363	0.023	0.691	0.669	0.584				

364	0.023	0.749	0.726	0.634				
365	0.022	0.808	0.780	0.684				
366	0.022	0.864	0.830	0.730				
367	0.021	0.912	0.876	0.772				
368	0.021	0.952	0.910	0.806				
369	0.021	0.981	0.935	0.831				
370	0.020	0.996	0.949	0.846				
371	0.020	1.000	0.951	0.852				
372	0.019	0.993	0.940	0.848				
373	0.019	0.973	0.920	0.831				
374	0.019	0.940	0.889	0.804				
375	0.018	0.899	0.849	0.769				
376	0.018	0.850	0.800	0.729				
377	0.017	0.795	0.749	0.686				
378	0.017	0.740	0.698	0.641				
379	0.016	0.684	0.644	0.595				
380	0.016	0.632	0.593	0.552				
381	0.016	0.580	0.545	0.509				
382	0.015	0.531	0.497	0.466				
383	0.015	0.485	0.453	0.429				
384	0.015	0.447	0.417	0.397				
385	0.014	0.409	0.383	0.366				
386	0.014	0.378	0.354	0.341				
387	0.013	0.350	0.329	0.319				
388	0.013	0.326	0.308	0.299				
389	0.013	0.305	0.289	0.283				
390	0.012	0.288	0.273	0.269				
391	0.012	0.274	0.260	0.258				
392	0.012	0.262	0.250	0.249				
393	0.011	0.252	0.241	0.241				
394	0.011	0.244	0.234	0.234				
395	0.010	0.237	0.227	0.228				
396	0.010	0.231	0.222	0.223				
397	0.010	0.226	0.217	0.218				
398	0.009	0.222	0.212	0.215				
399	0.009	0.218	0.209	0.212				
400	0.009	0.215	0.206	0.209				
401	0.008	0.211	0.203	0.206				
402	0.008	0.208	0.199	0.202				
403	0.008	0.205	0.196	0.199				
404	0.008	0.202	0.192	0.195				
405	0.007	0.198	0.188	0.191				
406	0.007	0.194	0.184	0.186				
407	0.007	0.189	0.180	0.182				
408	0.007	0.184	0.174	0.176				
409	0.007	0.178	0.169	0.171				
410	0.006	0.173	0.164	0.166				
411	0.006	0.167	0.158	0.161				

412	0.006	0.162	0.153	0.155				
413	0.005	0.156	0.147	0.150				
414	0.005	0.151	0.142	0.145				
415	0.005	0.146	0.136	0.139				
416	0.005	0.141	0.131	0.134				
417	0.005	0.136	0.126	0.128				
418	0.004	0.131	0.120	0.122				
419	0.004	0.125	0.115	0.116				
420	0.004	0.118	0.109	0.111				
421	0.004	0.113	0.103	0.105				
422	0.004	0.107	0.097	0.099	0.001	0.019	0.017	0.015
423	0.003	0.100	0.092	0.094	0.002	0.028	0.025	0.023
424	0.003	0.095	0.087	0.088	0.003	0.041	0.037	0.033
425	0.003	0.089	0.081	0.083	0.004	0.059	0.052	0.047
426	0.003	0.083	0.075	0.077	0.005	0.081	0.073	0.065
427	0.003	0.077	0.070	0.072	0.006	0.108	0.097	0.087
428	0.003	0.071	0.065	0.066	0.007	0.141	0.126	0.113
429	0.003	0.066	0.060	0.061	0.009	0.180	0.160	0.144
430	0.003	0.060	0.055	0.056	0.010	0.222	0.198	0.177
431	0.003	0.055	0.050	0.051	0.011	0.268	0.239	0.214
432	0.003	0.050	0.046	0.047	0.013	0.317	0.282	0.253
433	0.003	0.045	0.041	0.043	0.014	0.367	0.326	0.292
434	0.003	0.041	0.037	0.039	0.015	0.416	0.370	0.332
435	0.003	0.037	0.034	0.035	0.016	0.467	0.415	0.372
436	0.003	0.033	0.030	0.032	0.017	0.515	0.457	0.410
437	0.004	0.030	0.027	0.029	0.018	0.562	0.499	0.448
438	0.004	0.027	0.025	0.026	0.019	0.606	0.538	0.483
439					0.020	0.648	0.574	0.515
440					0.020	0.685	0.607	0.545
441					0.021	0.720	0.637	0.572
442					0.021	0.750	0.663	0.596
443					0.022	0.775	0.685	0.616
444					0.022	0.796	0.702	0.633
445					0.022	0.813	0.717	0.647
446					0.023	0.824	0.728	0.657
447					0.023	0.833	0.736	0.665
448					0.023	0.839	0.740	0.670
449					0.023	0.840	0.742	0.671
450					0.023	0.838	0.741	0.672
451					0.023	0.834	0.738	0.669
452					0.023	0.828	0.732	0.666
453					0.023	0.818	0.725	0.660
454					0.023	0.808	0.717	0.654
455					0.023	0.797	0.707	0.645
456					0.023	0.784	0.696	0.635
457					0.023	0.769	0.683	0.625
458					0.023	0.756	0.670	0.613
459					0.023	0.740	0.657	0.600

460					0.023	0.725	0.642	0.588
461					0.023	0.709	0.627	0.576
462					0.022	0.693	0.613	0.562
463					0.022	0.676	0.599	0.549
464					0.022	0.660	0.585	0.537
465					0.022	0.643	0.571	0.524
466					0.021	0.628	0.558	0.511
467					0.021	0.612	0.545	0.499
468					0.021	0.597	0.532	0.486
469					0.021	0.582	0.519	0.474
470					0.021	0.567	0.505	0.462
471					0.021	0.553	0.492	0.450
472					0.020	0.538	0.478	0.438
473					0.020	0.524	0.465	0.427
474					0.020	0.510	0.452	0.416
475					0.019	0.496	0.440	0.404
476					0.019	0.482	0.428	0.393
477					0.019	0.468	0.416	0.382
478					0.018	0.455	0.404	0.370
479					0.018	0.441	0.392	0.359
480					0.017	0.427	0.380	0.347
481					0.017	0.413	0.368	0.336
482					0.017	0.400	0.355	0.326
483					0.017	0.386	0.344	0.315
484					0.016	0.373	0.333	0.305
485					0.016	0.361	0.321	0.295
486					0.016	0.348	0.310	0.285
487					0.016	0.336	0.300	0.274
488					0.015	0.324	0.289	0.265
489					0.015	0.312	0.279	0.255
490					0.015	0.301	0.268	0.246
491					0.014	0.290	0.258	0.237
492					0.014	0.280	0.248	0.228
493					0.014	0.270	0.239	0.220
494					0.014	0.259	0.231	0.212
495					0.013	0.250	0.222	0.204
496					0.013	0.240	0.214	0.197
497					0.013	0.230	0.206	0.190
498					0.013	0.221	0.198	0.182
499					0.013	0.213	0.191	0.176
500					0.012	0.205	0.184	0.169
501					0.012	0.197	0.177	0.162
502					0.012	0.189	0.170	0.156
503					0.012	0.182	0.163	0.150
504					0.011	0.175	0.157	0.144
505					0.011	0.169	0.151	0.139
506					0.011	0.162	0.145	0.133
507					0.011	0.156	0.139	0.128

508					0.010	0.150	0.134	0.123
509					0.010	0.144	0.129	0.119
510					0.010	0.138	0.124	0.114
511					0.010	0.133	0.119	0.110
512					0.010	0.128	0.114	0.106
513					0.010	0.123	0.110	0.101
514					0.009	0.118	0.106	0.098
515					0.009	0.114	0.102	0.094
516					0.009	0.109	0.098	0.091
517					0.009	0.105	0.094	0.087
518					0.009	0.101	0.091	0.084
519					0.009	0.097	0.087	0.081
520					0.008	0.094	0.084	0.078
521					0.008	0.090	0.081	0.075
522					0.008	0.087	0.077	0.072
523					0.008	0.083	0.075	0.069
524					0.008	0.080	0.072	0.066
525					0.008	0.077	0.069	0.064
526					0.007	0.074	0.066	0.062
527					0.007	0.072	0.064	0.059
528					0.007	0.069	0.061	0.057
529					0.007	0.066	0.059	0.055
530					0.007	0.063	0.057	0.053
531					0.007	0.061	0.054	0.051
532					0.007	0.058	0.052	0.049
533					0.006	0.056	0.050	0.047
534					0.006	0.054	0.048	0.045
535					0.006	0.052	0.046	0.043
536					0.006	0.050	0.044	0.041
537					0.006	0.047	0.043	0.040
538					0.006	0.046	0.041	0.038
539					0.006	0.044	0.039	0.036
540					0.005	0.042	0.038	0.035
541					0.005	0.041	0.036	0.034
542					0.005	0.039	0.035	0.032
543					0.005	0.037	0.033	0.031
544					0.005	0.036	0.032	0.030
545					0.005	0.034	0.031	0.028
546					0.005	0.033	0.029	0.027
547					0.005	0.032	0.028	0.026
548					0.005	0.031	0.027	0.025
549					0.005	0.029	0.026	0.025
550					0.004	0.028	0.025	0.024
551					0.004	0.027	0.024	0.023
552					0.004	0.026	0.023	0.022
553					0.004	0.025	0.022	0.021
554					0.004	0.024	0.022	0.020
555					0.004	0.023	0.021	0.019

556					0.004	0.022	0.020	0.019
557					0.004	0.022	0.019	0.018
558					0.004	0.021	0.018	0.017
559					0.004	0.020	0.018	0.016
560					0.003	0.019	0.017	0.015
561					0.003	0.018	0.016	0.014
562					0.003	0.017	0.016	0.014
563					0.003	0.017	0.015	0.013
564					0.003	0.016	0.015	0.012
565					0.003	0.016	0.014	0.012
566					0.003	0.015	0.014	0.011
567					0.003	0.014	0.013	0.011
568					0.003	0.014	0.013	0.011
569					0.003	0.013	0.012	0.010
570					0.003	0.013	0.012	0.010
571					0.003	0.012	0.011	0.009
572					0.003	0.012	0.011	0.009
573					0.003	0.011	0.010	0.009
574					0.002	0.011	0.010	0.008
575					0.002	0.011	0.010	0.008
576					0.002	0.010	0.009	0.008
577					0.002	0.010	0.009	0.007
578					0.002	0.010	0.008	0.007

Table A2. Fluorescent excitation (Ex) and emission (Em) spectra three aqueous solutions of 0.9mM C3CA and 0.1mM 7HOC3CA in 7% gelatin. pH 6.0 represents a solution in deionized water, pH 7.4 represents a solution in phosphate buffered saline, and pH 10 represents a solution in sodium hydroxide and sodium bicarbonate.

Wavelength (nm)	**pH 6.0 Ex**	**pH 7.4 Ex**	**pH 10 Ex**	**pH 6.0 Em**	**pH 7.5 Em**	**pH 10 Em**
322	0.014	0.013	0.009			
323	0.015	0.013	0.010			
324	0.015	0.013	0.010			
325	0.016	0.014	0.011			
326	0.017	0.014	0.012			
327	0.018	0.015	0.014			
328	0.019	0.016	0.015			
329	0.020	0.017	0.017			
330	0.021	0.018	0.018			
331	0.023	0.019	0.020			
332	0.024	0.021	0.023			
333	0.026	0.022	0.025			
334	0.027	0.024	0.028			
335	0.030	0.025	0.031			
336	0.032	0.028	0.034			
337	0.035	0.030	0.038			
338	0.038	0.033	0.042			
339	0.041	0.036	0.046			
340	0.045	0.039	0.051			

341	0.049	0.043	0.056			
342	0.054	0.047	0.061			
343	0.060	0.052	0.067			
344	0.066	0.057	0.073			
345	0.073	0.064	0.079			
346	0.080	0.070	0.086			
347	0.088	0.079	0.092			
348	0.098	0.088	0.099			
349	0.109	0.099	0.107			
350	0.122	0.112	0.114			
351	0.137	0.126	0.122			
352	0.152	0.142	0.129			
353	0.170	0.160	0.136			
354	0.189	0.179	0.144			
355	0.210	0.201	0.152			
356	0.234	0.225	0.159			
357	0.260	0.251	0.166			
358	0.286	0.278	0.174			
359	0.313	0.307	0.181			
360	0.341	0.336	0.188			
361	0.367	0.364	0.194			
362	0.392	0.393	0.201			
363	0.415	0.419	0.208			
364	0.434	0.441	0.215			
365	0.449	0.460	0.222			
366	0.459	0.474	0.229			
367	0.464	0.480	0.235			
368	0.462	0.483	0.242			
369	0.455	0.477	0.248			
370	0.443	0.467	0.255			
371	0.427	0.452	0.262			
372	0.407	0.435	0.270			
373	0.383	0.412	0.276			
374	0.357	0.389	0.283			
375	0.330	0.364	0.290			
376	0.303	0.340	0.299			
377	0.276	0.315	0.306			
378	0.252	0.294	0.315			
379	0.229	0.275	0.325			
380	0.208	0.259	0.335			
381	0.190	0.245	0.345			
382	0.172	0.234	0.355			
383	0.156	0.223	0.365			
384	0.143	0.215	0.376			
385	0.131	0.208	0.388			
386	0.121	0.203	0.399			
387	0.113	0.197	0.412			
388	0.106	0.194	0.425			

389	0.100	0.191	0.439			
390	0.095	0.189	0.453			
391	0.090	0.186	0.467			
392	0.087	0.184	0.484			
393	0.084	0.183	0.500			
394	0.081	0.180	0.517			
395	0.080	0.178	0.538			
396	0.078	0.176	0.558			
397	0.076	0.173	0.579			
398	0.075	0.170	0.602			
399	0.074	0.166	0.625			
400	0.073	0.163	0.647			
401	0.072	0.159	0.673			
402	0.070	0.155	0.702			
403	0.069	0.150	0.730			
404	0.068	0.145	0.760			
405	0.066	0.139	0.792			
406	0.065	0.133	0.822			
407	0.063	0.127	0.852			
408	0.061	0.121	0.880			
409	0.059	0.116	0.907			
410	0.058	0.110	0.927			
411	0.056	0.104	0.946			
412	0.054	0.098	0.958			
413	0.052	0.092	0.962			
414	0.050	0.086	0.959			
415	0.048	0.081	0.950			
416	0.045	0.075	0.930			
417	0.043	0.070	0.901			
418	0.041	0.064	0.866			
419	0.039	0.059	0.822			
420	0.037	0.055	0.772			
421	0.035	0.050	0.719			
422	0.033	0.046	0.664	0.006	0.007	0.013
423	0.031	0.042	0.606	0.009	0.010	0.020
424	0.029	0.039	0.549	0.014	0.015	0.031
425	0.027	0.036	0.493	0.021	0.022	0.047
426	0.025	0.032	0.437	0.030	0.032	0.070
427	0.023	0.029	0.385	0.041	0.044	0.097
428	0.022	0.027	0.337	0.056	0.059	0.132
429				0.073	0.078	0.175
430				0.094	0.099	0.223
431				0.116	0.123	0.278
432				0.141	0.149	0.336
433				0.168	0.176	0.397
434				0.194	0.203	0.457
435				0.223	0.232	0.518
436				0.250	0.259	0.576

437				0.277	0.287	0.633
438				0.304	0.312	0.685
439				0.329	0.336	0.735
440				0.351	0.359	0.780
441				0.372	0.379	0.822
442				0.391	0.397	0.858
443				0.407	0.414	0.890
444				0.421	0.427	0.917
445				0.433	0.438	0.940
446				0.442	0.447	0.958
447				0.449	0.453	0.974
448				0.454	0.458	0.985
449				0.456	0.460	0.993
450				0.457	0.461	0.998
451				0.456	0.461	1.000
452				0.454	0.458	0.999
453				0.450	0.456	0.995
454				0.446	0.451	0.990
455				0.441	0.446	0.982
456				0.434	0.440	0.972
457				0.427	0.433	0.961
458				0.419	0.425	0.948
459				0.411	0.417	0.934
460				0.402	0.408	0.919
461				0.393	0.399	0.902
462				0.384	0.391	0.884
463				0.376	0.382	0.866
464				0.367	0.373	0.847
465				0.358	0.364	0.828
466				0.349	0.355	0.809
467				0.340	0.346	0.789
468				0.332	0.338	0.770
469				0.324	0.329	0.750
470				0.316	0.320	0.731
471				0.307	0.312	0.711
472				0.299	0.304	0.692
473				0.291	0.296	0.672
474				0.283	0.288	0.653
475				0.275	0.280	0.633
476				0.268	0.272	0.613
477				0.260	0.264	0.595
478				0.253	0.256	0.576

Chapter 3

Violet Diode Laser-Induced Fluorescence

3.1 Introduction

Complexities of modern radiotherapy treatment delivery have advanced to a level of sophistication requiring patient specific quality assurance. The need for inexpensive and practical three-dimensional dosimetry systems is apparent; gel dosimetry has repeatedly been championed as a potential solution.[1] Gel dosimeters possess the potential to provide fully integrated three-dimensional dose distributions.

The most reactive known oxidizers, hydroxyl radicals, are produced by water radiolysis due to interactions with ionizing radiation. When aqueous-based solutions of coumarin-3-carboxylic acid (C3CA) are exposed to ionizing radiation, hydroxyl free radicals readily induce hydrogen abstraction and hydroxylation of the aromatic ring producing 7-hydroxy-coumarin-3-carboxylic acid (7HO-C3CA), a derivative of the well-characterized fluorescent sensor umbelliferone.[2]

Activation of C3CA may be an analogue for biological damage because interactions with hydroxyl free radicals produce the same reactants responsible for the majority of DNA double-strand breaks and injury. Hydroxyl free radicals induce hydrogen abstraction and hydroxylation of the aromatic ring of coumarin-3-carboxylic acid to form 7-hydroxycoumarin-3-carboxylic acid, a known fluorescent probe.[3] Figure 1 illustrates the

production and subsequent excitation of 7-hydroxycoumarin-3-carboxylic acid under ultra-violet (365nm) to violet (405nm) light with a visible cyan (455nm) emission.

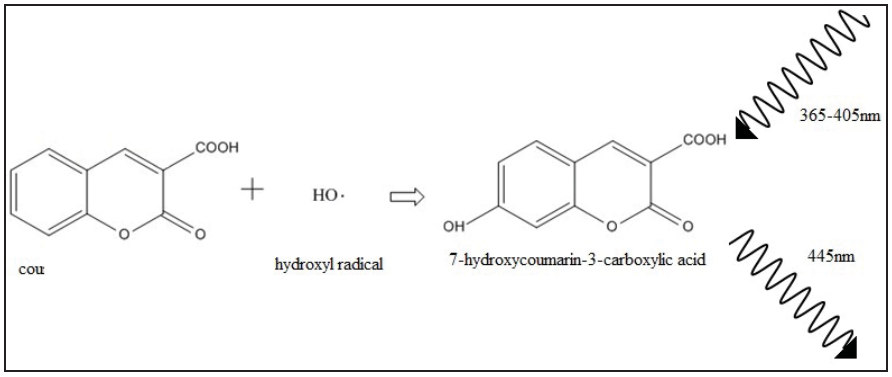

Figure 1. Coumarin-3-carboxylic acid hydroxylzed in the presence of ionizing radiation due to hydroxyl free radicals, producing 7-hydroxycoumarin-3-carboxylic acid, a fluorescent molecule exciting in the range of 365-405nm and emitting a 445nm.

The formation of fluorescent products in response to ionizing radiation and measurement of absorbed dose by quantification of fluorescent emission intensity is referred to as radio-fluorogenic dosimetry (RFD). This study describes investigations of violet diode laser-induced fluorescence (LIF) with C3CA embedded in gelatin as a RFD detector with potential for multi-dimensional spatial resolution. Possessing favorable characteristics, such as high sensitivity and selectivity, laser-induced fluorescence (LIF) is recognized as a powerful analytic tool.[4]

RFD gels were irradiated with a sealed source of Ir-192. LIF was performed using a divergent beam violet diode laser that creates an excitation plane to image spatial dose distributions. The two-dimensional pattern of fluorescent emission yields images of the integrated absorbed dose distribution. The relative radial dose of the Ir-192 HDR source was compared to published results. Feasibility of using violet diode LIF for

characterizing spatial distributions of fluorescent products within an RFD detector is demonstrated.

3.2 Methods

3.2.1 Fabrication

Food grade, type A gelatin* (Fisher Scientific, Baltimore, MD) was soaked in cold, deionized water for 15-30 minutes before dissolving. A volume of coumarin-3-carboxlyic acid was prepared and added to gelatin to achieve a detector consisting of 10mM coumarin in 7% gelatin. The temperature of the gel solution was raised to no higher than 35°C on a hotplate and maintained for approximately 90 minutes. Degradation of the gel detector will occur above 40°C. When the gel becomes clear, a pipet is used to fill sample containers. The samples are cooled overnight before irradiation.

3.2.2 Irradiation

An aperture is provided in the lid of the sample container to accommodate the source catheter (2mm radius). Prior to irradiation, samples were imaged using a commercial computed tomography scanner (Brilliance; Phillips Healthcare, Amsterdam, Netherlands) with catheters in place. DICOM format images were transferred to a commercial treatment planning system (Brachyvision; Varian Medical Systems, Palo Alto, CA) for comparison calculations of dose distributions. The x and y axis of each sample container was marked to ensure proper alignment for comparison of dose distributions.

Guide-tubes were connected to catheters inserted in the detectors and samples irradiated for 90 minutes with a 7 Ci Ir-192 source from a high dose rate (HDR) remote after-loader (GammaMed iX-plus; Varian Medical Systems, Palo Alto, CA). Figure 2 shows the irradiation arrangement for cylindrical vials. Cuvettes were irradiated in a similar fashion; however, the source catheter radius was 1mm.

a.  b. 

Figure 2. (a) Photograph of sample container with catheter inserted, (b) Photograph of catheter connected to Ir-192 remote afterloader.

3.2.3 Analysis

Samples were analyzed by violet diode LIF immediately following irradiation. A 5mW circular laser beam coupled to a cylinder lens was used to create an excitation plane. The planar excitation path yields an axial view of the dose distribution, with a slice thickness the width of the original circular beam, i.e., 2mm. Digital images were collected using an 8MP camera equipped with a complementary metal-oxide-semiconductor (CMOS) detector. Figure 3 shows the arrangement used to obtain dosimetric images with gelatin

solutions. Image pixel intensity was analyzed to determine the relative radial dose distribution of the Ir-192 source.

(a) 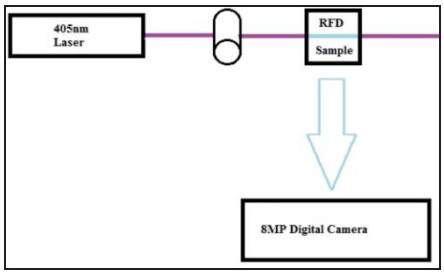

(b) 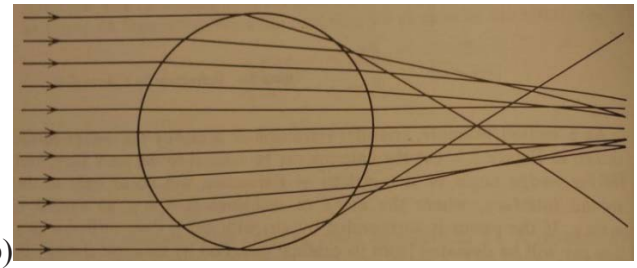

Figure 3. Setup used for LIF of gel detectors. (a) Right angle collection with 8MP CMOS digital camera. (b) Illustration of cylinder lens as used to create a planar excitation beam with a width equal to the diameter of the initial circular beam. In the present experiment a 2mm diamter beam was coupled to a 12mm diameter cylinder. Shown is a small cylinder relative to the incident beam.[5]

Planar images normal to the excitation path were collected and analyzed to determine radio-fluorogenic response. Absorbed dose is represented by intensity of the 445nm, cyan fluorescent emission. Images were analyzed in ImageJ, where color channel separation, grayscale, and smoothing was applied.[6] Blue image channel was saturated in unfiltered images, thus the green channel was selected for analysis. (Figure 4)

a.  b.  c. 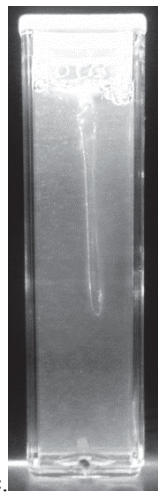 d. 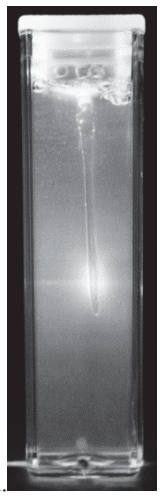 e. 

Figure 4. Unfiltered cuvette images (a) original color image, (b) grayscale, (c) red channel, (d) green channel, (e) blue channel. Blue channel shows significant saturation effects with the green channel exhibiting the most contrast. No smoothing was applied to the above images.

Gelatin and coumarin exhibit a yellow/orange hue at higher concentrations, as discussed in the previous chapter. The yellow color from the sample overlapping with the cyan emission yields a measurable response in the green channel. Dependent on the cyan emission, the green response is believed to respond linearly with fluorescent intensity. Saturation effects were less evident with images collected at an extended distance (see Figure 5).

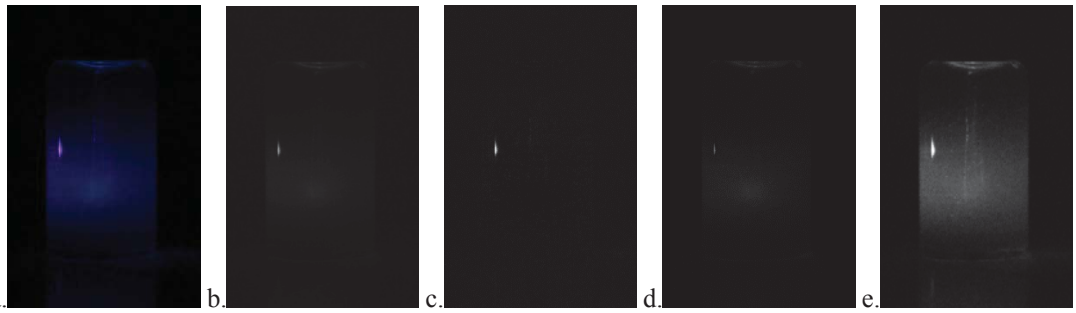

Figure 5. Images collected from an extended distance. a. original color image, b. grayscale, c. red channel, d. green channel, e. blue channel. Blue and green channel exhibiting measurable response. No smoothing was applied to the above images.

3.3 Results/Discussion

Results from images of the radio-fluorogenic detector, C3CA in gelatin, applied to the determination of two-dimensional spatial patterns of energy deposition from an Ir-192 source are reported. Analysis of images of gel detectors in both cuvette and cylindrical containers are shown. Qualitative comparisons of doses are shown for calculated distributions from commercial planning software. The relative radial dose is plotted with published values, showing subjectively good agreement.

3.3.1 Qualitative Dose Distributions

The visible cyan emission is evident in images of detector samples, see Figures 4 and 5. Grayscale images were used to obtain relative iso-line intensity distributions. Distributions of fluorescent intensity, corresponding to energy deposition in the radio-fluorogenic samples, were shown with window and leveling of images. Further smoothing yielded fairly symmetric distributions, qualitatively comparative to calculated isodose values (see Figure 6).

a. b. c.

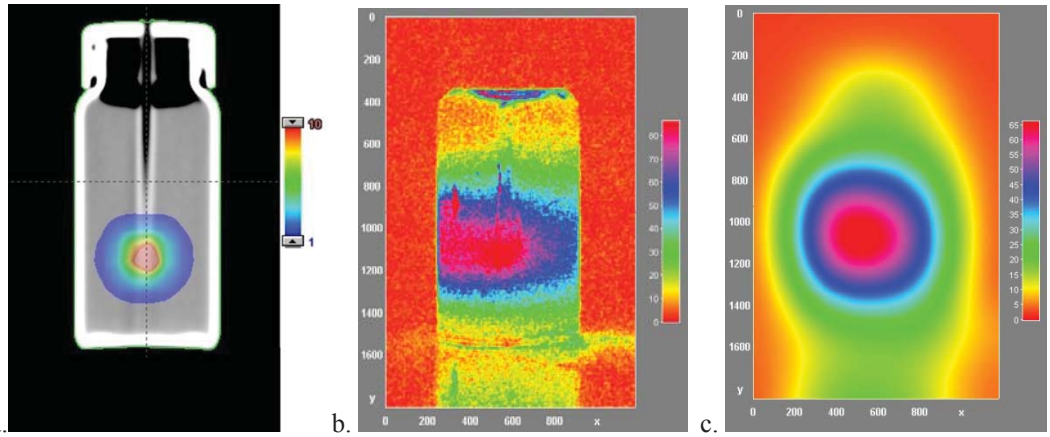

Figure 6. Calculated dose distribution for qualitative comparison to processed image from Figure 5. (a) Dose distribution as calculated by commercial treatment planning software (Brachyvision; Varian Medical Systems, Palo Alto, CA). (b) Window and leveled detector image shown with a thermal color palate, demonstrating a dose distribution qualitatively similar to distribution shown in (a). (c) Smoothed detector image from (a), significant improvements in symmetry are seen by the application of averaging.

The above results demonstrate a spatial pattern of fluorescent emission visually correlating to a known distribution of dose deposition. Several artifacts are observed that impact the accuracy of the resultant image. Lens flaring, produced by reflection at the sample container interface, is the most apparent. This is evident by the increased response on the left. In Figure 5, the flare is evident as the white object on the upper left of the sample container. The differential excitation with depth is also apparent. This is due to

the inner filter effect as described in the previous chapter whereby the excitation light intensity is absorbed by the sample proportional to path length. This can be mitigated in future work by the determination and application of correction factors, to be discussed in the following chapter.

A second image was used to obtain a point spread function. Smoothing, window and leveling was applied to obtain intensity isolines. Converted to grayscale, a line profile cutting through the axis of the most intense point was used to generate a point spread function demonstrating an equivalent point source. (Figure 7)

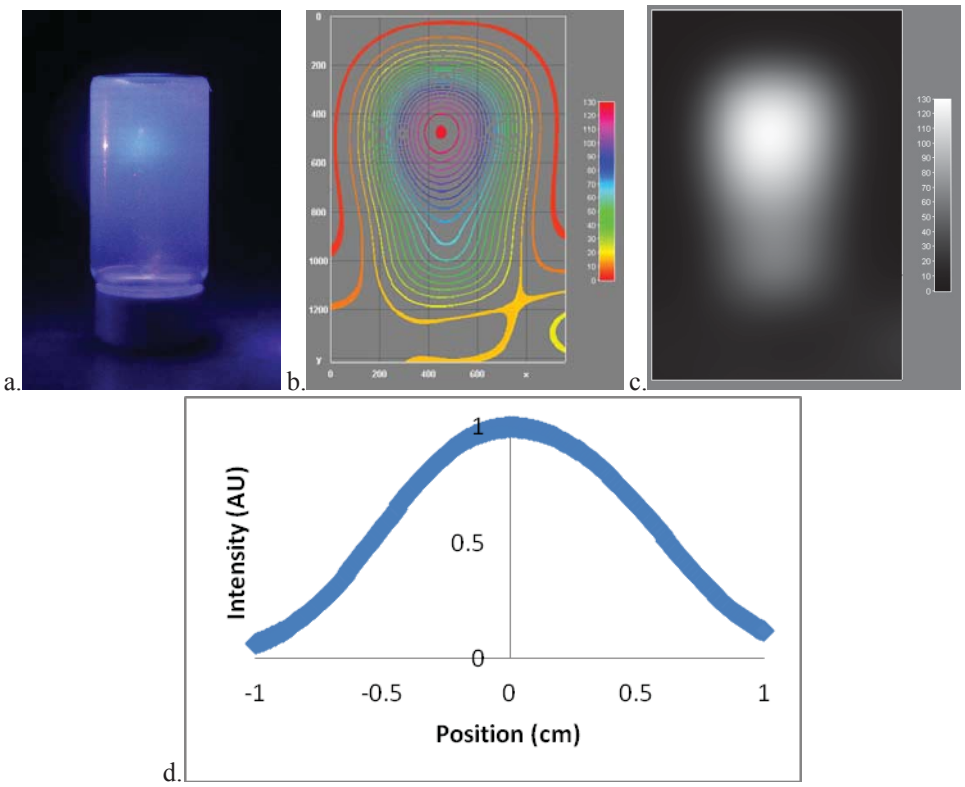

Figure 7. Image of fluorescent emission from radio-fluorogenic gel detector temporarily embedded with an Ir-192 source. (a) Unprocessed image, void from insertion and removal of source catheter is visible through the y-axis of the sample container. (b) Processed image, smoothed and shown as intensity isolines. (c) Processed image, smoothed and grayscale. (d) Pixel line profile of smoothed grayscale image, a broad point spread function is shown, qualitative demonstration of an equivalent point source.

A line profile bisecting the y-axis of the dose distribution should be approximately symmetric. The model of an equivalent point source is commonly applied to brachytherapy in calculating a point of interest where the source distribution is symmetric relative to the detection volume.[7-8] The above results are qualitative analyses of spatial distributions of fluorescent intensity, the dosimeter response function, as a metric for absorbed dose. These results demonstrate the feasibility of imaging spatial dose distributions with radio-fluorogenic imaging. Many refinements can and should be applied to future collection and analyses; these will be discussed at length in the following chapter.

3.1.2 Relative Radial Dose Distribution

Images of LIF in the investigated radio-fluorogenic detector were analyzed to obtain the relative radial dose distribution for comparison to published reports; see Figure 4 for the original image. A line profile bisecting the source was obtained and a plot of intensity versus position was determined. Inner-filter effect was minimized with the assumption of radial symmetry with left and right pixel intensity values averaged. This profile was contrasted with other authors' data, collected by MRI imaging of polymer gels and Monte Carlo calculations.[9-10]

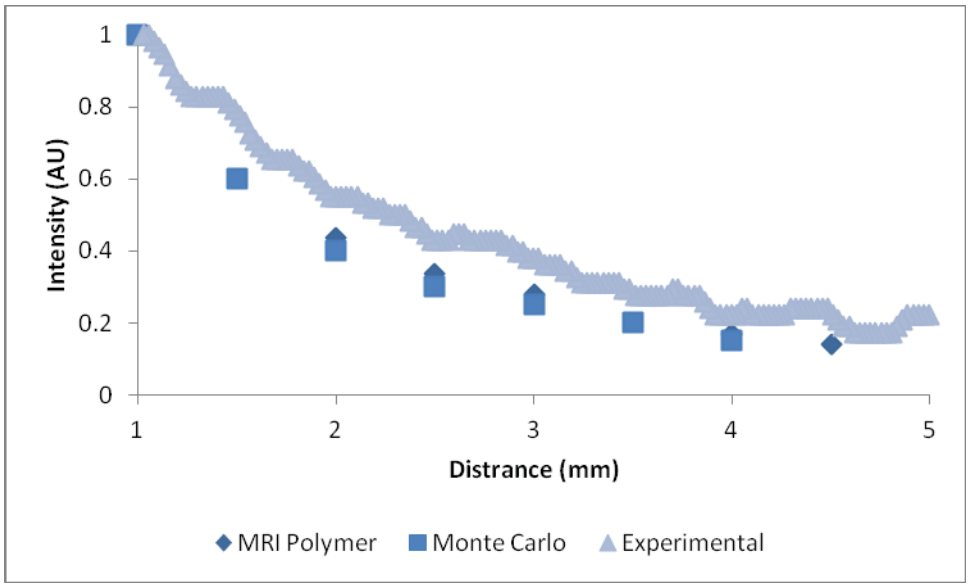

Figure 8. Relative radial dose compared with other reports. Triangle, experimental results of violet diode LIF; line profile of gray scale image, left and right pixel intensities averaged. Diamond, VIPAR polymer gel values from magnetic resonance imaging of 3.0mm slices.[7] Square, Monte Carlo generated values from MCNP.[8] Data for plot in appendix, tables A1 and A2.

The above results show a fair correlation of published results with collected images demonstrating agreement within 20%. This deviation is much larger than hoped; however, such results are promising for initial studies. The combination of inner-filter effects and non-optimized excitation and emission collection optics clearly has a significant impact on the quality of results. The complex spectral nature of the Ir-192 source may also play a role. While improvements can be made in the collection of images, to be discussed in the following chapter, these results are unambiguous evidence of the ability to obtain spatial patterns of absorbed dose by radio-fluorogenic gel detectors.

3.4 Conclusion

The preceding data and analysis demonstrate the feasibility of obtaining spatial dose distributions from radio-fluorogenic detectors, C3CA in gelatin, with violet diode LIF. These results support the working hypotheses originally proposed. The fluorescent intensity produced by LIF following irradiation can be analyzed to determine the spatial pattern of energy deposition.

The compound has now been successfully applied with a gel substrate for the determination of a two-dimensional spatial pattern of energy distribution by analyzing the distribution of fluorescent intensity produced after irradiating the dosimeter. Collection of planar images is the first step in the determination of three-dimensional dose distributions. Optical focusing with cylinder lenses to create divergent beams for imaging planar distributions presents as a potential approach for three-dimensional imaging. Coupling the divergent LIF with a rotational stage to obtain a series of axial projections could provide the data for three-dimensional image reconstruction. Such a method will be discussed in the following chapter regarding the design of a three-dimensional reader.

References

1. C. Baldock et al. "Polymer gel dosimetry," Physics in Medicine and Biology 55(5), p. R1 (2010).

2. I. Johnson, and M. Spence, Eds., *Molecular probes handbook: A guide to fluorescent probes and labeling technologies*, 11th Edition (Eugene, OR, Molecular Probes, 2010).

3. A. K. Collins, G. M. Makrigiorgos, et al., "Coumarin chemical dosimeter for radiation therapy," Medical Physics 21(11), p. 1741-1747 (1994).

4. G. R. Van Hecke and K. K. Karukstis, *A guide to lasers in chemistry* (Boston, Jones and Bartlett, 1998).

5. C. M. Vest, *Holographic interferometry* (New York, John Wiley and Sons, Inc., 1979).

6. W. S. Rasband, *ImageJ* (Bethesda, US National Institutes of Health, 1997).

7. R. Nath, L. L. Anderson, et al., "Dosimetry of interstitial brachytherapy sources: Recommendations of the AAPM Radiation Therapy Committee Task Group No. 43," Medical Physics 22, p. 209-234 (1995).

8. M. J. Rivard, B. M. Coursey, et al., "Update of AAPM Task Group No. 43 Report: A revised AAPM protocol for brachytherapy dose calculations," Medical Physics 31(3), p. 633-674 (2004).

9. P. Papagiannis, E. Pappas, et al., "Dosimetry close to an Ir HDR source using N-vinylpyrrolidone based polymer gels and magnetic resonance imaging," Medical physics 28, p. 1416 (2001).

10. N. Kolbun, P. Levêque, et al., "Experimental determination of the radial dose distribution in high gradient regions from a low dose rate iridium-192 wire sources using EPR imaging," World Congress on Medical Physics and Biomedical Engineering (Munich, Germany, Springer, September 7-12, 2009).

Appendix

Table A1. Published data used for comparison to experimental results. “MRI Polymer,” represents a VIPAR gel imaged with 3.0mm slices with magnetic resonance imaging (Kolbun, Levêque et al. 2009). “Monte Carlo” represents values generated with MCNP (Papagiannis, Pappas et al. 2001).

mm	MRI Polymer	mm	Monte Carlo
2.000	0.438	4.000	0.150
2.500	0.337	3.500	0.200
3.000	0.281	3.000	0.250
4.000	0.169	2.500	0.300
4.500	0.140	2.000	0.400
		1.500	0.600
		1.000	1.000

Table A2. Experimental results violet diode LIF; line profile of gray scale image of Ir-192 source, left and right pixel intensities averaged.

mm	Intensity (AU)	mm	Intensity (AU)	mm	Intensity (AU)	mm	Intensity (AU)
6.400	0.086	5.050	0.207	3.700	0.293	2.350	0.500
6.373	0.086	5.023	0.224	3.673	0.276	2.323	0.500
6.346	0.086	4.996	0.224	3.646	0.276	2.296	0.500
6.319	0.103	4.969	0.224	3.619	0.276	2.269	0.500
6.292	0.103	4.942	0.224	3.592	0.276	2.242	0.517
6.265	0.103	4.915	0.224	3.565	0.276	2.215	0.517
6.238	0.103	4.888	0.224	3.538	0.276	2.188	0.517
6.211	0.103	4.861	0.207	3.511	0.276	2.161	0.534
6.184	0.103	4.834	0.190	3.484	0.293	2.134	0.534
6.157	0.103	4.807	0.172	3.457	0.293	2.107	0.552
6.130	0.103	4.780	0.172	3.430	0.310	2.080	0.552
6.103	0.103	4.753	0.172	3.403	0.310	2.053	0.552
6.076	0.103	4.726	0.172	3.376	0.310	2.026	0.552
6.049	0.121	4.699	0.172	3.349	0.310	1.999	0.552
6.022	0.138	4.672	0.172	3.322	0.310	1.972	0.552
5.995	0.155	4.645	0.172	3.295	0.310	1.945	0.569
5.968	0.172	4.618	0.172	3.268	0.310	1.918	0.586
5.941	0.172	4.591	0.190	3.241	0.310	1.891	0.603
5.914	0.172	4.564	0.190	3.214	0.328	1.864	0.621
5.887	0.172	4.537	0.207	3.187	0.345	1.837	0.621
5.860	0.172	4.510	0.224	3.160	0.345	1.810	0.638
5.833	0.172	4.483	0.241	3.133	0.362	1.783	0.655
5.806	0.172	4.456	0.241	3.106	0.362	1.756	0.655

5.779	0.172	4.429	0.241	3.079	0.362	1.729	0.655
5.752	0.172	4.402	0.241	3.052	0.362	1.702	0.655
5.725	0.172	4.375	0.241	3.025	0.379	1.675	0.655
5.698	0.155	4.348	0.241	2.998	0.379	1.648	0.672
5.671	0.155	4.321	0.241	2.971	0.379	1.621	0.690
5.644	0.155	4.294	0.241	2.944	0.397	1.594	0.707
5.617	0.155	4.267	0.224	2.917	0.397	1.567	0.724
5.590	0.172	4.240	0.224	2.890	0.414	1.540	0.759
5.563	0.190	4.213	0.224	2.863	0.414	1.513	0.776
5.536	0.224	4.186	0.224	2.836	0.431	1.486	0.793
5.509	0.241	4.159	0.224	2.809	0.431	1.459	0.810
5.482	0.259	4.132	0.224	2.782	0.431	1.432	0.828
5.455	0.276	4.105	0.224	2.755	0.431	1.405	0.828
5.428	0.276	4.078	0.241	2.728	0.431	1.378	0.828
5.401	0.276	4.051	0.241	2.701	0.431	1.351	0.828
5.374	0.276	4.024	0.224	2.674	0.431	1.324	0.828
5.347	0.276	3.997	0.224	2.647	0.448	1.297	0.828
5.320	0.276	3.970	0.224	2.620	0.448	1.270	0.828
5.293	0.276	3.943	0.224	2.593	0.448	1.243	0.845
5.266	0.259	3.916	0.224	2.566	0.431	1.216	0.862
5.239	0.259	3.889	0.241	2.539	0.431	1.189	0.879
5.212	0.241	3.862	0.259	2.512	0.431	1.162	0.914
5.185	0.224	3.835	0.276	2.485	0.431	1.135	0.948
5.158	0.224	3.808	0.276	2.458	0.448	1.108	0.966
5.131	0.207	3.781	0.276	2.431	0.466	1.081	0.983
5.104	0.207	3.754	0.276	2.404	0.466	1.054	1.000

Chapter 4

Spatial Dosimetry

4.1 Introduction

Radio-fluorogenic coumarin-3-carboxylic acid (C3CA) reacts with hydroxyl radicals to form a fluorescent product in response to ionizing radiation. Sensors such as radio-fluorogenic detectors must often be coupled to transducer circuits or reader systems for analysis. A significant impediment to implementation of radio-fluorogenic dosimeters is the availability of a dedicated reader for quantitative measurements.

Gel dosimeters, first with Fricke (ferrocyanide in gelatin) and later polymer solutions, were initially imaged with magnetic resonance imaging (MRI). The use of computed tomography (CT) has also been explored. However, development of stand-alone optical reader systems was initiated as an alternative to the use of clinical devices. Optical-Computed-Tomography (OCT) systems are now commonly used for the determination of 3D dose distributions with gel dosimeters.

OCT systems commonly employ transmission techniques, where the transmitted intensity of light is measured and attenuation due to scattering or absorption within the gel detector determined as a function of absorbed dose. The application of apparatus to the emission-computed tomography of fluorescent distributions is a relatively new

development. Typical arrangement of transmission OCT and an existing system for Optical-ECT is shown using parallel opposed high-pressure mercury lamps (Figure 1).[1]

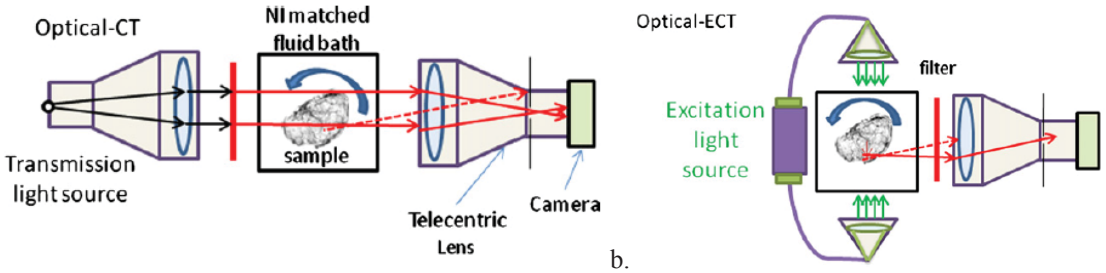

a. b.

Figure 1. Illustrations of existing systems used for transmission and emission computer tomography, from reference.[1] Telecentric lenses are used to reduce collection of scattered photons. Dashed lines represent rejected light. (a) Transmission apparatus, single light source coupled to a single detector. (b) Emission apparatus, two parallel-opposed light sources coupled to a single detector normal to the excitation path.

For a fluorescent reader, the system can be examined as consisting of three components: excitation source, sample chamber, and emission detector. Lenses are inherent, since light sources and detectors both require focusing and collimation for optimal observations. With C3CA in gelatin, the spatial pattern of fluorescent emission by violet diode laser-induced fluorescence (LIF) has been shown to yield two-dimensional images of integrated dose distributions.

Determination of three-dimensional dose distributions is the ultimate application of a gel dosimetry system. Design of a system capable of three-dimensional imaging was explored. A basic optical reader system was fabricated and violet diode laser excitation source coupled with a CMOS detector, embedded in a conventional digital camera, was explored for the measurement of dose response with aqueous solutions of C3CA. A new method of three-dimensional analysis is proposed for imaging radio-fluorogenic detectors.

4.2 Methods

4.2.1 Fabrication

Aqueous solutions were prepared with filtered and deionized water obtained from a water purification system (EASYpure; Barnstead International, *Dubuque, IA*). C3CA was brought into solution by bringing the substance and a small volume of water to a boil. Additional water was added to the volume of C3CA to obtain 1mM concentration. The solution was allowed to cool and then placed into high-density polyethylene (HDPE) containers for irradiation.

4.2.2 Irradiation

RFD irradiations were conducted with a medical linear accelerator (Varian Trilogy; Varian Medical Systems, Palo Alto, CA). Using a 10x10cm applicator and gantry angle of 90 degrees, such that the entire volume was in-field, samples in cylindrical HDPE containers were placed on a marked styrofoam block on the central axis of the beam with surface set to 100SSD. Samples were irradiated with 20 MeV electrons delivered at a nominal dose rate of 5 Gy/min. Individual samples were irradiated with 0.1, 0.5, 1, 5, 10, 5, 10, 15, 20, 25, and 50 Gy.

4.2.3 Analysis

Violet diode lasers were used for the sample excitation and digital cameras embedded with CMOS detectors were used for collection of images. Aliquots of irradiated aqueous

solutions were placed in polystyrene cuvettes and exposed to 30mW circular 405nm violet diode laser beam. The LIF emission was imaged for each aliquot with an 8MP digital camera coupled to a 10nm band-pass filter with peak transmission at 450nm. (Figure 2)

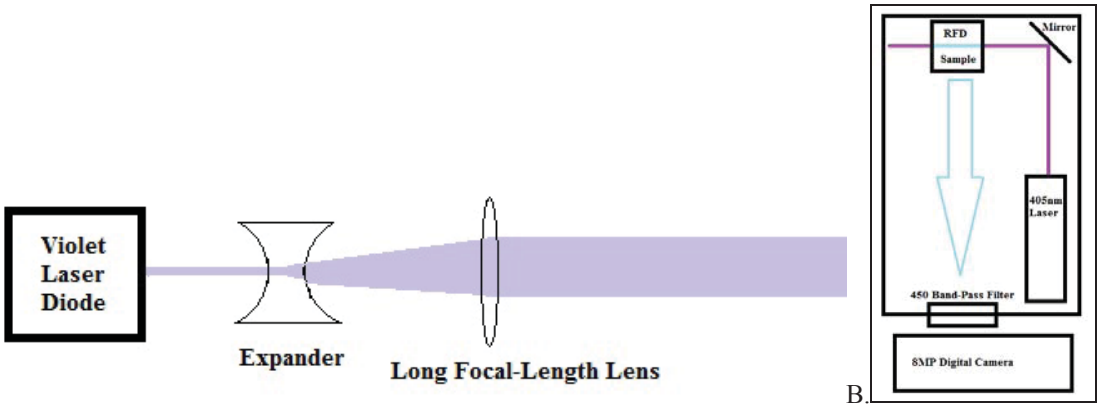

A. B.

Figure 2. Schematic of LIF setup for collection of RFD aqeuous images. (a) Illustration of internal focusing optics of circular 30mW 405nm violet diode laser. (b) Reader system showing right-angle image collection with an 8MP CMOS detector and band-pass filter (450nm, 10nm).

The radio-fluorogenic dose-response curve was determined by measuring the intensity of 445nm emissions from irradiated aqueous solutions. Images normal to the excitation path were analyzed to determine response. Color images were split into RGB channels; with filtered images, the blue channel was selected for analysis of aqueous solutions. A line profile of pixel intensity was determined from images collected at a right angle from the laser excitation path.

4.3 Results/Discussion

Results from a basic dedicated reader for C3CA radio-fluorogenic response are reported. Analysis of the dose response for an aqueous solution of C3CA is shown. Output from a script for the determination of an automated dose curve with MatLab is shown. Further

analysis of the normalized dose response calculated by analysis with ImageJ is compared to results obtained with a conventional fluorescent spectrometer equipped with a Xenon arc lamp. Proposed design of a full three-dimensional imaging system and a method of analysis; attenuation corrections for excitation and emission, is submitted and discussed.

4.3.1 Basic Design and Dose Response

Irradiated aqueous solutions were examined with a basic dedicated violet diode LIF reader system to obtain a dose response curve. A Gaussian profile is typical of circular laser beams. The excitation path of a circular beam demonstrates the greatest intensity along its central axis. This characteristic was exploited to obtain the response function. Collected images were analyzed with Image J and excitation profiles from violet diode LIF were plotted (see Figure 3).

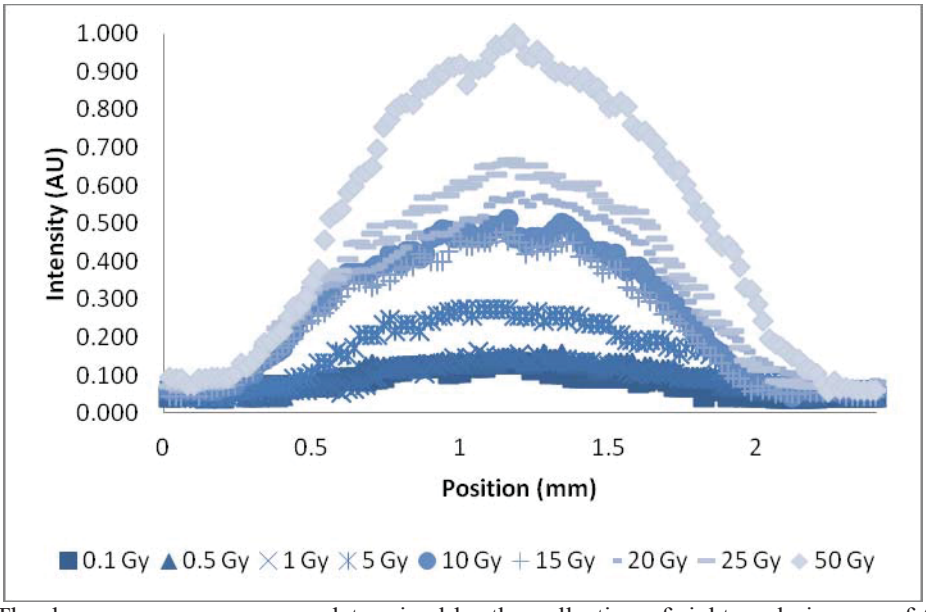

Figure 3. The dose response curve was determined by the collection of right-angle images of the 445nm blue fluorescent emission produced by LIF excitation. Plot of the blue channel line profile, intensity of emission represented by increasing pixel value. Values below 5 Gy are irresolvable (within 20%) from background.

The basic system demonstrated a quantifiable radio-fluorogenic response function for doses 5 Gy and above. Maximum values were normalized to unity. Profiles demonstrate a noisy Gaussian distribution. Plotting peak intensity values versus dose, aqueous samples demonstrated a measurable response within the observed range of 0.1-50 Gy (Figure 4).

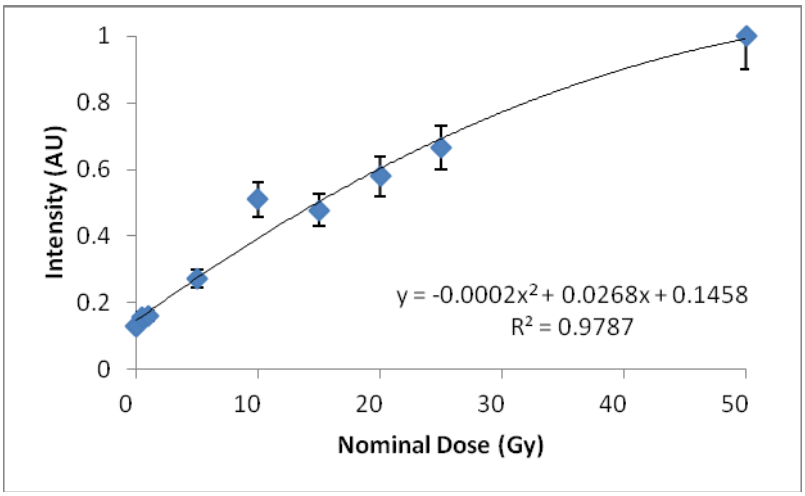

Figure 4. Maximum pixel intensity values of emission line profile normalized to unity and plotted against nominal dose to obtain a response curve. Results show sublinear dose response in the range of 0.1-50 Gy; error bars represent an arbitrary relative 5% error. Curve fit with a first-order polynomial, the results show $R^2 = 0.9787$.

Results show a concave downward, supra-linear, dose response in the range of 0.1-50 Gy ($y = -0.0002x^2 + 0.0268x + 0.1458$). Responses below 5 Gy are irresolvable from background. Doses 5 Gy and above were compared to values collected with a dedicated Xenon arc lamp spectrofluorimeter, see Figure 5.

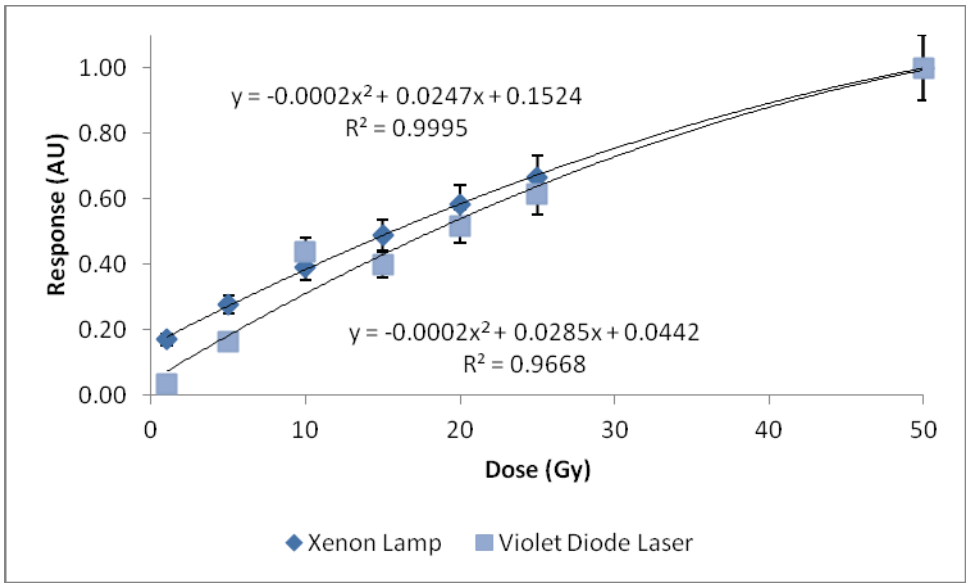

Figure 5. Comparison of response from (diamond) Xenon Lamp and (square) violet diode laser. Relatively good agreement is shown with a the Xenon lamp demonstrating a lower threshold of response,

Table 1. Tabulated data of normalized dose response for aqueous solutions of 1mM C3CA irradiated with 20MeV electrons. Percent difference shown with larger discrepancies at lower doses.

Dose (Gy)	Xenon Lamp	Violet Diode Laser	Percent Difference
1	0.17	0.03	65.76%
5	0.28	0.16	25.88%
10	0.39	0.44	5.30%
15	0.49	0.40	10.12%
20	0.58	0.52	6.22%
25	0.67	0.61	4.01%
50	1.00	1.00	0.00%

Shown above, a basic dedicated reader demonstrated a measureable dose response comparable to a Xenon lamp spectrofluorimeter. Tabulated results shown in Table 1.A MatLab script, provided in the appendix, was written to obtain the line profile of the excitation path from a series of images. The full-width half-maximum (FWHM) of the excitation profile was plotted as a function of dose demonstrating a dose response curve (see Figure 6).

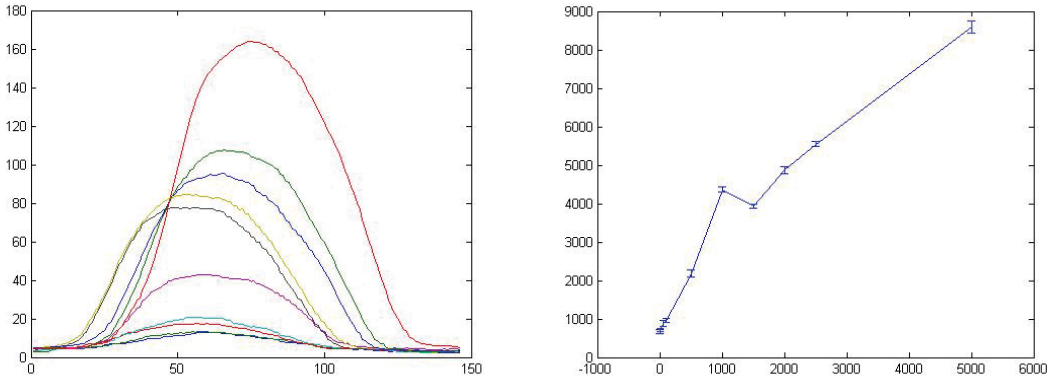

Figure 6. Initial dose response; Left, line profiles of emission (y-axis, intensity in aribitrary units; x-axis, pixel number); Right, dose response curve (y-axis, intensity in aribitrary units; x-axis, dose in cGy)

The above method could be applied for the determination of a calibration curve with a detecticated reader system. These results demonstrate the feasibility of violet diode LIF coupled with CMOS detectors for the quantification of fluorescent response of a radio-fluorogenic detectors.

4.3.2 Three-Dimensional Reader

Development and design of a dedicated multi-dimensional reader system for radio-fluorogenic dosimetry has been explored. Three-dimensional imaging can be accomplished using rotational and/or translational manipulation of the object. Multiple projections from a number of angles and application of a mathematical algorithm can be used to reconstruct a three-dimensional image.

In diagnostic radiology with computed tomography (CT) and nuclear medicine with positron emission tomography (PET), the Radon transformation has been coupled with transmission and emission projections (CT and PET respectively) to obtain 3D images. The principal method has been with back-projection, where a series of images is collected

to form a sinogram and processed by dividing the intensities from multiple projections evenly between the pixels within the projection path. These same methods may be applied to fluorescent imaging.

A proposed system utilizes both transmission and emission techniques to obtain attenuation correction factors and a resultant three-dimensional image. The basic premise of the approach uses a planar excitation source. For light incident a cylinder, the angle of divergence is proportional to distance from the paraxial ray. The mathematical description is as follows:

$$\theta_1 = \tan^{-1}\left[\frac{y}{(R^2 - y^2)^{1/2}}\right] = \sin^{-1}\left(\frac{y}{R}\right)$$

Where θ represented the angle of divergence, y is the distance from the cylinder bisection (location of paraxial ray) and R is the cylinder radius; results are plotted in Figure 7. In the plotted results, a cylinder with radius = 6mm is shown.

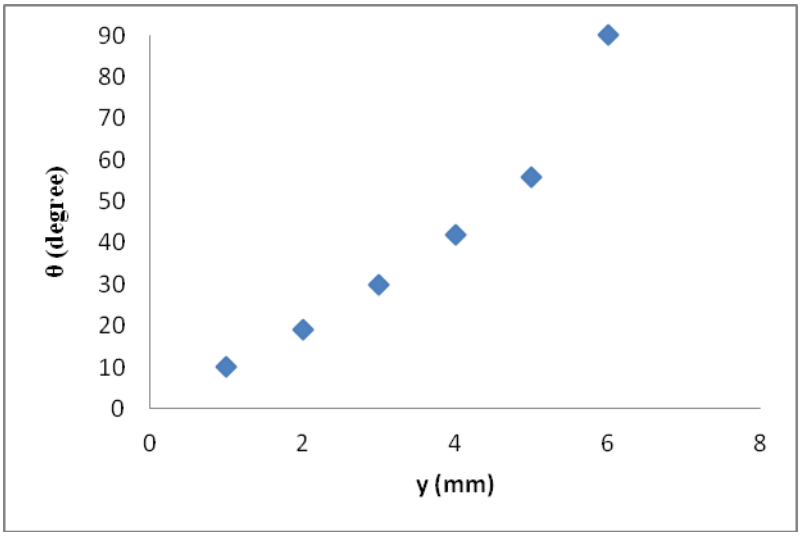

Figure 7. Plot of refraction by a 6mm radius homogeneous cylinder as a function of distance from bisection. Optimization of incident beam radius with respect to cylinder lens is a requirement for accurate geometric design.

Cylinder lenses are used to provide a line focus instead of a point focus. In the previous chapter, a cylindrical lens was used to create a divergent beam creating multiple rays to illuminate a plane of the object. Planar imaging of projections from multiple angles of a sample, mounted on a rotational stage would provide data for three-dimensional reconstruction.

As stated in the introduction, fluorescent analysis requires an excitation source, sample chamber and emission detector. The basic proposed 3D reader system—not including focusing optics understood to consist of lenses previously discussed and data processing hardware—consists of five elements. For accurate, attenuation-corrected measurements, an emission transmission source, excitation transmission detector, emission detector, and a rotational stage should be assembled (see Figure 8).

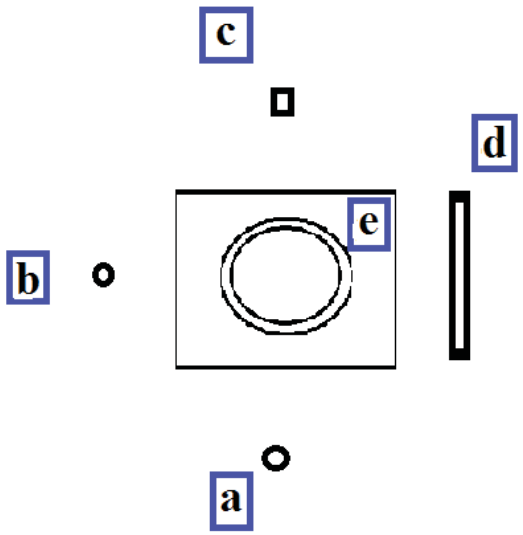

Figure 8. Elements of a proposed LIF-ECT system. Lenses for focusing of detected excitation and emission photons are not illustrated. (a) 405nm diode laser coupled to a cylinder lens for creation of planar excitation beam (b) 445nm LED for emission attenuation correction source. (c) Planar CMOS photodiode array for excitation attenuation correction. (d) Flat panel CMOS array for emission detection. (e) Rotational stage for sample.

The apparatus outlined above would require a four-step process for the collection of quantitative 3D dose distributions from radio-fluorogenic detectors. The first two steps could be performed on a periodic basis to ensure proper function of sources and detectors. Calibration processes would test for source and detector constancy and uniformity (see Figure 9).

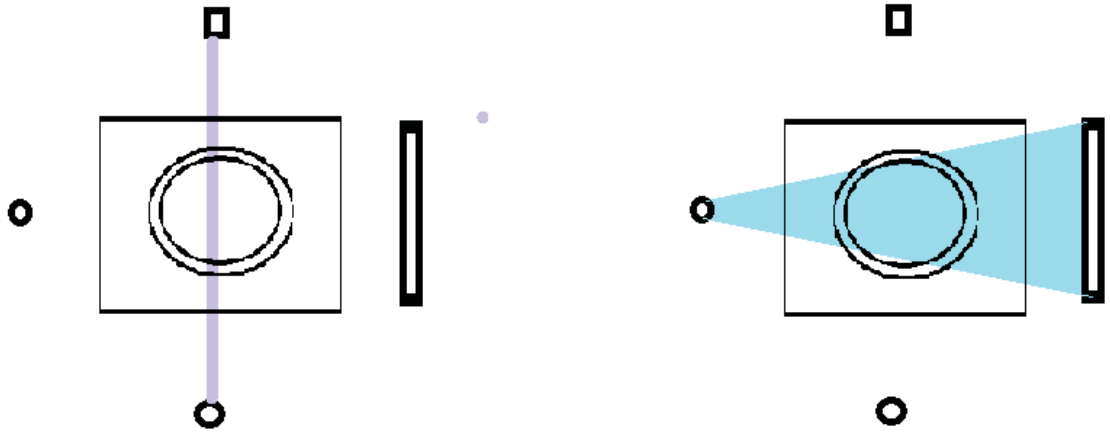

Figure 9. Illustration of two-step source and detector calibration process. (left) 405nm excitation source incident planar array for attenuation correction of excitation light. (Right) Transmission source for attenuation correction of emission light. Collection would occur without sample present to determine source and detector constancy and uniformity, respectively.

Figure 9 illustrates a method for calibration of components of the proposed reader system. Sample read-out would also necessitate a two-step process for determination of accurate attenuation correction factors (Figure 10).

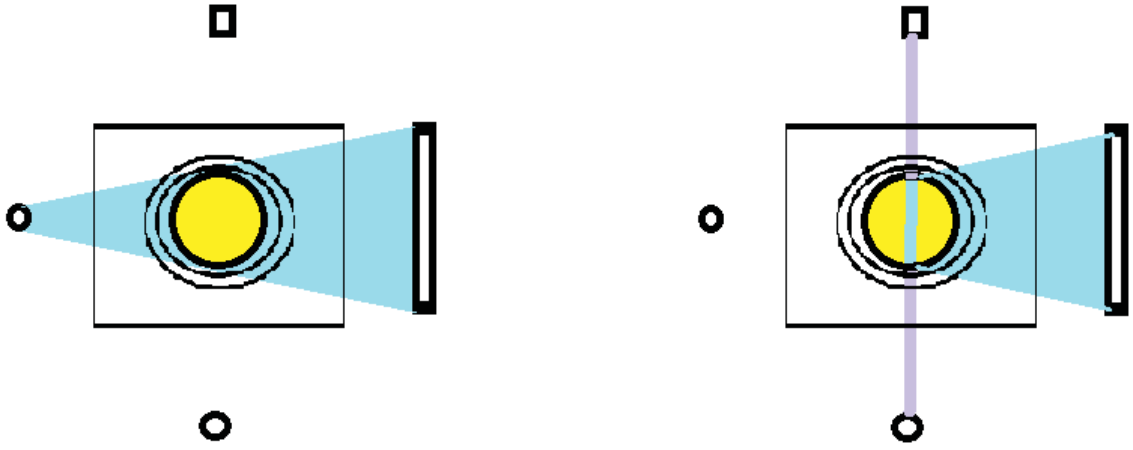

Figure 10. Illustration of two-step reading process. (Left) LED emission source incident sample for determination of emission attenuation correction factors. (Right) Diode laser excitation source incident sample illustrating collection of in-line transmission and normal planar emission projection.

Accurate quantitative measurements of emission-computed tomography necessitate the determination of attenuation correction factors for both excitation and emission light. The proposed system uses an LED of the emission wavelength as a point source for the collection of cone-beam images for determination of transmission correction factors. A detector in-line with the excitation source would be used for the determination of excitation correction factors. An illustration of the collection process is shown below (Figure 11).

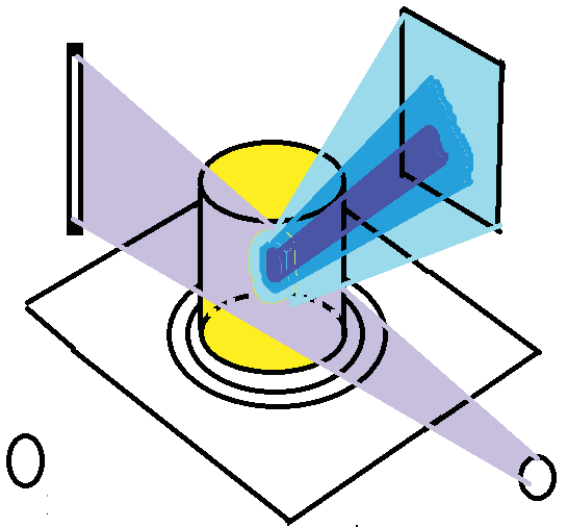

Figure 11. Illustration of LIF-ECT with RFD detector. Rotational stage allows for collection of multiple projections, resultant sinogram permits reconstruction to a 3-D distribution of energy deposition within the detector.

Figure 11 shows a proposed system design for the determination of 3D dose distributions with a radio-fluorogenic detector. A second analytical approach may employ the iterative methods of reconstruction by solving a modified linear Boltzmann equation or coupled excitation and emission radiative transfer equations. The presented results, coupled with

the previous chapters, illustrate a proposed method for three-dimensional radio-fluorogenic dosimetry.

4.4 Conclusion

A hypothetical reader has been designed to determine distributions of energy deposition in volumes of a radio-fluorogenic gel detector. Cylindrical samples provide favorable geometry for rotational image analysis. By rotating the sample through a 360-degree arc, multiple right-angle images could be collected and analyzed to reconstruct a three-dimensional image by use of filtered back-projection. The processing of such three-dimensional images is beyond the scope of the present research and remains an enticing subject for further study.

References

1. A. Thomas, J. Bowsher, et al., "A comprehensive method for optical-emission computed tomography," Physics in medicine and biology 55(14), p. 3947 (2010).

2. S. R. Cherry, J. A. Sorenson, et al., *Physics in Nuclear Medicine* (Philadelphia, Saunders, 2003).

3. C. M. Vest, *Holographic interferometry* (New York, John Wiley and Sons, Inc., 1979).

Appendix

MatLab code for processing of images; results shown in Figure 3:

```
clear all;
imname=dir('*.jpg');          %image selection
d=size(imname,1);             %number of images
dose=[0, 10, 50, 100, 500, 1000, 1500, 2000, 2500, 5000]; % dose vector
for calibration

xline = [2305,2450];          %start and end point for line profile
yline = [1350,1350];          %y pixel coordinate

for k= 1:d;                   %for number of images

RGB = imread(imname(k).name); %load image, RGB = color image
B = RGB(:,:,3);               %filter just blue, B = blue layer
c=1;
for n = -30:1:30;
    ylinen=yline+n;
        parp(:,c)=improfile(B, xline, ylinen);    %line profile of
images
        b=parp(:,c);                               %iteration
        y=max(b)/2<= b;                         %FWHM, values greater
than
        areavar(c) = trapz(b(y));
        c=c+1;

end

p(:,k)= mean(parp,2);    % average line profile of images
avar(k)=std(areavar);

a=p(:,k);                              %iteration
y=max(a)/2<= a;                        %FWHM, values greater than
area(k) = trapz(a(y));                 %area of curve greater than FWHM
                          %restart
%assignin('base', ['profile', num2str(k)], p(:,k))

end
figure(1);plot(p); legend
figure(2);
errorbar(dose,area,avar);
%plot(dose,area,dose,area-avar,'-',dose,area+avar,'-');grid on;
```

Chapter 5

Conclusions

5.1 Research Accomplishments

A water-equivalent radio-fluorogenic detector was produced by the use of C3CA in gelatin, reacting in a predictable manner with hydroxyl free radicals formed by exposure to ionizing radiation. Undertaken to explore development of a non-toxic water-equivalent radiation dosimeter with capacity for spatial resolution, the present work yielded spatial images of dose distributions with a radio-fluorogenic gel dosimeter excited by violet diode LIF.

The ultimate application of the investigated chemical dosimeter is the determination of spatial dose distributions. The described work demonstrated such systems could be applied to the determination of complex dose distributions. A limiting factor has been a specialized method for reading the resultant fluorescent patterns. The design of a reader system has been outlined presenting an avenue for future work.

5.2 Future Work

Radio-fluorogenic polymers excited by mercury-arc lamps are a recent development in the search for active agents for gel dosimetry.[1-4] LIF with optical-emission computed tomography coupled with a method for excitation and emission correction, as proposed in

the preceding chapter, may be an interesting method for providing high-resolution three-dimensional images.

The application of LIF to assay radio-fluorogenic products in phantom material has been demonstrated by the present work. Other investigators have studied *in vitro* measurements; this suggests *in vivo* studies may be possible.[5-6] Molecular biological imaging is an active area of investigation with multiple methods based on labeling biomarkers with fluorescent probes; coumarin has been identified as a potential probe.[7] Reported studies indicate labeling coumarin compounds to peptide ligands, designed for DNA binding, hold potential as sensitive sensors of biological response.[8-9] Extended dose ranges should be explored further; pulsed LIF may provide high flux excitation for studies of low dose response.

References

1. J. M. Warman, M. P. De Haas, and L. H. Luthjens, “High-energy radiation monitoring based on radio-fluorogenic co-polymerization. I: small volume in situ probe,” Physics in medicine and biology 54(10), p. 3185 (2009).

2. J. M. Warman, M. P. De Haas, and L. H. Luthjens, “High-energy radiation monitoring based on radio-fluorogenic co-polymerization II: fixed fluorescent images of collimated x-ray beams using an RFCP gel,” Physics in medicine and biology 56(5), p. 1487 (2011).

3. J. M. Warman, M. P. de Haas, et al. "A Radio-Fluorogenic Organic Gel for Real-Time, 3D Radiation Dosimetry," Advanced Materials 23(42), p. 4953-4955 (2011).

4. J. M. Warman, M. P. de Haas, et al., “High-energy radiation monitoring based on radio-fluorogenic co-polymerization III: Fluorescent images of the cross-section and depth-dose profile of a 3MV electronbeam,” Radiation Physics and Chemistry 84, p. 129-135 (2013).

5. M. Park, S. C. Moore, et al., "Performance of a coumarin-based liquid dosimeter for phantom evaluations of internal dosimetry," Nuclear Instruments and Methods in Physics Research Section A: Accelerators, Spectrometers, Detectors and Associated Equipment 569(2), p. 543-547 (2006).

6. M. J. Kim, S. Pal, et al., "Determination of the dose–depth distribution of proton beam using resazurin assay< i> in vitro</i> and diode laser-induced fluorescence detection," Analytica chimica acta 593(2), p. 214-223 (2007).

7. B. Jakob and M. Durante, "Radiation Dose Detection by Imaging Response in Biological Targets," Radiation Research 177(4), p. 524-532 (2012).

8. C. C. Perry, V. J. Tang, et al., "Use of a Coumarin-Labeled Hexa-Arginine Peptide as a Fluorescent Hydroxyl Radical Probe in a Nanoparticulate Plasmid DNA Condensate," The Journal of Physical Chemistry B 115(32), p. 9889-9897 (2011).

9. V. J. Tang, K. M. Konigsfeld, et al., "DNA binding hydroxyl radical probes," Radiation Physics and Chemistry 81(1), p. 46-51 (2012).